Università
Ca'Foscari
Venezia

Master's Degree in
Science and Technology of Bio and Nanomaterials

Final Thesis

Characterization of silicon nitride powders and assessment of antibacterial properties: the effect of pH

Supervisor *:*
Prof. Alvise Benedetti
Prof. Giuseppe Pezzotti

Graduand *:*
Martina Cammisano
Matr. n. 872872

Academic year *:*
2019-2020

“Quando li piedi suoi lasciar la fretta,
che l’onestade ad ogn’atto dismaga,
la mente mia, che prima era ristretta,

lo ’ntento rallargò, sì come vaga,
e diedi ’l viso mio incontr’al poggio
che ’nverso ’l ciel più alto si dislaga.”

Dante Alighieri,
Purgatorio, C. III, vv. 10-15

Abstract

Progress in the development and understanding of antibacterial materials could positively contribute in limiting the spreading of drug-resistant bacteria and lowering the number of infections. Silicon nitride (Si_3N_4) has great properties for biomedical applications and recent studies reported on its ability to hinder bacterial adhesion and chemically affect microbial viability. In this study Si_3N_4 powders were tested with the aim of gaining further understanding on the mechanism and its dependency on pH. Experiments were performed in liquid cultures of *S. epidermidis* (0-24h) and *P. gingivalis* (0-72h) using 4 and 16 mg of powder per mL of culture broth. Five initial pH values were used: 5.5, 6.5, 7.5, 8 and 8.5. The mere powders were exposed to the same pH conditions and characterized afterwards by vibrational spectroscopies, XPS and zeta potential measurements. The antibacterial effects were assessed using WST-8 assay and Raman spectroscopy. The powder concentration of 16 mg/mL had a stronger impact, according to both WST and spectroscopic data. Silicon nitride activity was appreciable in both acidic and basic conditions but varied with pH and bacterial strain, as supported by variations in relevant Raman bands. The characterization of the powders revealed oxidation, to a variable extent depending on the pH treatment: pH groups 5.5 and 8 emerged significantly. This study confirms that the antibacterial activity of Si_3N_4 relies on a pH-dependent mechanism related to surface chemistry and dissolution phenomena. Further research is required to elucidate the involved reactions; experimental procedures could be optimized and complemented by additional techniques (e.g. fluorescence microscopy for bacteria and XRD for the powders).

Contents

List of Figures

List of Tables

Objective

The aim of this project was to assess the antibacterial properties of silicon nitride powder in aqueous solutions and to shed light on the underlying bio-chemical processes, which are not fully understood yet. More specifically, this study addressed the role of the amount of powder dispersed in liquid culture media and the effects of environmental pH on the activity of silicon nitride against bacteria. As regarding biological factors, the project was aimed at understanding whether different bacterial cell wall structures are affected differently.

Project overview

The experimental project was divided into three main parts. The first one concerned the characterization of silicon nitride (Si_3N_4) powders by means of Raman spectroscopy, Fourier Transform Infrared spectroscopy, X-Ray photoelectron spectroscopy and zeta potential measurements. The powders were treated in aqueous media at different pH values (in the range from 5.5 to 8.5) prior to the analysis in order to investigate the effects of pH on the powder itself. Methods and results are discussed in Chapter 3. The other experiments focused on the antibacterial effects of Si_3N_4 and employed the use of microbial viability assays and Raman spectroscopy. The second part, presented in Chapter 4, was devoted to the assessment of the effect of different concentrations of Si_3N_4 on bacterial cultures and the selection of one concentration value for the subsequent experiments. The last part explored how bacteria are affected by silicon nitride powders as a function of initial pH of the culture media. Data analysis and results are elaborated in Chapter 5. Chapter 1 contextualizes and provides reasons of interest for this study while in Chapter 2 all the characterization techniques and assays that were used are briefly explained. The final Chapter (Chapter 6) summarizes the main results and reports considerations on future outlooks, also accounting for the limitations of the present study.

1 Introduction

This Chapter contextualizes the study with important reasons on which the project builds on, providing relevant background information about the key protagonists of the project, namely silicon nitride, the bacterial species *Staphylococcus epidermidis* and *Porphyromonas gingivalis*, and the use of Raman spectroscopy for biological samples.

1.1 The need for investigation on antibacterial materials

One of the main threats to global health and sustainable development, within the framework of the United Nations' 2030 Agenda, is the emergence of multi-drug resistant pathogens and the rapid spreading of Antimicrobial Resistance (AMR). AMR, which can be defined as "the resistance of microorganisms to an antimicrobial agent to which they were at first sensitive" [1, 2], was included by the World Health Organization (WHO) in the top 10 global concerns for public health [3]. Since microorganisms can quickly spread around the world, it is clear that AMR constitutes a "One Health" problem which connects the health of people, animals and the environment [4]; therefore serious action against this threat is needed from several sectors in the attempt to both control and prevent AMR.

Objects and surfaces can be contaminated and serve as vehicles for spreading, which means that also the materials are involved in the problem and their properties could be exploited and tailored to circumscribe it. Engineering an antimicrobial surface could be more effective and long lasting compared to conventional disinfection methods [5]. In this effort, contributions from the materials and biomaterials scientific communities are highly relevant for the emergence of new antimicrobial strategies based on materials [6]. These may find applications in multiple fields, such as water treatments, personal care products, healthcare, and "smart" food packaging [7, 8]. Special attention should be paid to the biomedical and clinical sectors, which are seriously affected by AMR. Only considering antibiotic-resistant bacteria, their burden of infections in EU and EEA countries has increased since 2007 and it was estimated that 75% of these infections is associated with health-care infections [9], accounting for $\sim$ 25% of the total healthcare-associated infections (HAIs). As stated by the Centers for Disease Control and Prevention (CDC) in the 2019 Antibiotic Resistance Threats Report [10] in the United States there was an overall 28% decrease in deaths from antibiotic resistance in hospitals compared to the 2013 report, but the number of AMR infections in the US is still around 2.8 million per year, with more than 35000 deaths.

It would be beneficial to find alternative solutions to limit the spreading and proliferation of bacteria in the healthcare environment, on surfaces and tools but also on materials that must be inserted in the human body for orthopaedic applications. Currently existing material-based antibacterial solutions can be broadly classified into i) bacteria-resisting (or anti-adhesive), ii) bacteria-killing (or bactericidal) and iii) bacteria-releasing (reducing adhesion of bacteria but also facilitating the release of adhered bacteria); nowadays also materials that combine two of the strategies have been developed [11, 12]. Along with the development of these materials it is important to carry out proper assessments of the related risks and to precisely define the most appropriate applications, trying to avoid abuse and misuse of such materials, which could otherwise lead to new forms of resistance from the microorganisms [13]. Despite the increasing number of publications on these topics, for several materials reported to have antimicrobial properties the mechanism of action is not clearly understood yet [14], suggesting that additional research efforts are required.

1.2 Silicon nitride: properties and applications

Silicon nitride (Si_3N_4) is a ceramic material that exists at atmospheric conditions in two crystal polymorphs called α-Si_3N_4 and β-Si_3N_4, both having hexagonal structure but differing in stacking and thus in symmetry: the former structure has been assigned to space group $P3_1C$, with trigonal symmetry, while the latter corresponds to either space group $P6_3$ or $P6_3m$, with hexagonal symmetry [15, 16]. The common building blocks can be imagined as slightly distorted tetrahedra where a silicon atom is at the center of each tetrahedron and nitrogen atoms occupy the corners, the corners are joined among adjacent tetrahedra so that each N is shared by three of them [17, 18].

After the first studies on structure and properties, significant interest in Si_3N_4 started to grow in the 1960s thanks to the evidence of its good high temperature properties and in particular the resistance to thermal shock, which made this material an excellent candidate for refractory molds and high-temperature components for automobiles [18]. Other remarkable properties, even though dependent on the actual microstructure, are high strength (also at high temperatures with respect to metals), high hardness and fracture toughness, lower coefficient of friction compared to bearing steel, low thermal expansion coefficient and good creep resistance, which allow Si_3N_4 to reach the market with applications in industrial cutting tools, glow-plugs, bearings and metal-casting tools [17–19]. In the last few decades many studies have reported on silicon nitride being biocompatible, non cytotoxic and visible in radiographs, making it promising for biomedical applications [20]. Specifically it is already clinically used in spinal fusion implants - with positive outcomes from patient follow-up also after 30 years [21] - and is under study as a candidate for dental implants [22, 23] as well as for knee and hip prostheses bearing components [24, 25].

In the context of antibacterial properties and applications, in 2013 Si_3N_4 was reported in the class of anti-adhesives [26] due to hydrophilicity but there is more recent evidence of some active chemical mechanism of Si_3N_4 against different bacteria such as *Staphylococcus epidermidis*, *Escherichia coli* and *Porphyromonas gingivalis* [27, 28]. The activity appeared to be susceptible to pH conditions, particularly revolving around the equilibrium between NH_3 and NH_4^+ species which are generated as a consequence of Si_3N_4 dissolution phenomena in aqueous environment [27, 29]. So far the main studies focused on the bulk material but it can be informative to investigate the powders, so that surface-dependent physical effects that originate from the bulk samples (e.g. hydrophilicity) may be disregarded and further insights on the chemical phenomena could be gained. In the light of the above, although the custom use of the powders is to be converted into macroscopic parts and products through thermal and mechanical processes, from future studies new applications may emerge for the powder as-is.

1.3 Selected bacteria: *Staphylococcus epidermidis* and *Porphyromonas gingivalis*

Two bacterial species were chosen for the experiments reported in this work, based on their relevance for the topic and on the possibility of studying the effects of silicon nitride on bacteria with different behavior and properties. In fact the selected species, *Staphylococcus epidermidis* (*S. epidermidis*) and *Porphyromonas gingivalis* (*P. gingivalis*), belong to two distinct phyla and have different cell envelope structure: the former falls in the group of Gram-positive bacteria whereas the latter is a Gram-negative bacterium. Briefly recalling the structure of the two wall types, on the one hand Gram-negative bacteria have a thin wall composed of peptidoglycan but are provided with an outer membrane which is rich in lipopolysaccharide, on the other hand Gram-positive bacteria lack the outer membrane but they possess a much thicker peptidoglycan wall which is crossed by anionic polymers called teichoic acids (TAs) [30]. These envelopes may be affected by silicon nitride powders in different ways, as they have distinctive

components which constitute diverse protective barriers.

Concerning the context introduced in Sections 1.1 and 1.2, in particular healthcare-associated infections and the application of silicon nitride in the biomedical field, the chosen bacteria are very important because are typically present on/in the human body and both can be pathogenic. *S. epidermidis* is a colonizer of skin and mucosa, almost ubiquitous among healthy people, normally nonpathogenic but it behaves opportunistically: it easily enters through a compromised skin barrier (as it can be during surgical procedures, placement of a prosthesis or a catheter) and here turns into an infectious agent [31]. *S. epidermidis* is considered one of the main causes of hospital-acquired infection (HAI), most frequently being involved in infections of catheters, orthopaedic and breast implants; in fact these bacteria can adhere to the surface of the medical devices and develop a strong biofilm which is difficult to eradicate and often leads to surgical removal of implants coupled with antibiotic therapy [31–33]. *P. gingivalis* is instead renowned for being an oral pathogen, it can be found in the oral cavity of both healthy and diseased subjects, where it can cause periodontal inflammation and diseases such as periodontitis and alveolar bone resorption, in some cases eventually leading to tooth loss [34–36]. Apart from natural teeth damage, this bacterium is also frequently involved in the infection of dental implants, causing peri-implantitis which requires additional intervention and/or antibiotic therapy to prevent implant failure [37, 38]. A more effective solution could be the direct prevention of the infections with the use of functional implant materials.

1.4 Raman spectroscopy for biological materials

The theoretical principles of Raman spectroscopy are discussed in Section 2.2. From the ability to detect molecular vibrations one can get information on the chemical structure of a biological sample and from variations in such structure, in turn, one can infer about changes of biological interest. Some examples of application are: monitoring the presence of biomarkers of metabolic processes or diseases in a diagnostic fashion, as well as detecting variations in cellular components or identifying bacteria in complex matrices [39–41]. The technique is increasingly being used thanks to the advantage that signals are not affected by the presence of water molecules and no staining or external label is required, moreover the analyses can be performed non-destructively and in real-time [42]. Therefore Raman spectroscopy embodies excellent characteristics for the observation of alterations in bacteria in response to treatments with antibacterial agents. Nevertheless, one issue with this type of spectroscopy lies in the analysis and interpretation of the data, since Raman signals of biological material are very complex. In fact the same functional groups are contained in different biomolecules, such as carbohydrates, nucleic acids, lipids and proteins, giving rise to overlapping signals so that the same Raman band can have contributions from different biomolecules, which means that in some cases it is very difficult to assign a band with confidence [43].

Another challenge in data analysis arises when multiple "treatment" groups have to be analyzed. An intuitive procedure in the attempt to find differences among groups is to visually inspect and compare the average spectra, looking at peak intensities, shifts and widths. However, Raman spectra of biological samples often contain a high number of features (considering the common spectral region from $\sim$ 600 to 1800 cm^{-1}) and minor differences may go unnoticed [44]. Since relevant information may be contained in these minor differences, other data analysis methods can be employed to extract information from the data, typically on a mathematical/statistical basis. In this regards, multivariate data analysis methods, observing more than one variable at a time, are now frequently applied to handle Raman data sets of biological systems, allowing dimensionality reduction, data exploration and discrimination between clusters; the identified patterns can then be modeled and the models can be used for classification of

new data [45]. A recent review reported that among the several methods available for these purposes Principal Component Analysis (PCA) was the most commonly used one (in the selected studies) [44]. Some of the methods are now contained in ad hoc R packages which are under development (chemoSpec, hyperSpec) [46, 47]. An increasing public availability of datasets, libraries, spectral files and codes could enhance advances in this field of Raman spectroscopic analyses.

References

1. De Sousa Oliveira, K., De Lima, L., Cobacho, N., Dias, S. & Franco, O. *Chapter 2 - Mechanisms of Antibacterial Resistance: Shedding Some Light on These Obscure Processes?* in *Antibiotic Resistance* (Academic Press, 2016). doi:https://doi.org/10.1016/B978-0-12-803642-6.00002-2.
2. Tenover, F. & McGowan, J. *Antimicrobial Resistance* in *International Encyclopedia of Public Health* (Academic Press, 2008). doi:https://doi.org/10.1016/B978-012373960-5.00452-4.
3. World Health Organization. *Antimicrobial Resistance* https://www.who.int/news-room/fact-sheets/detail/antimicrobial-resistance.
4. Centers for Disease Control and Prevention. *A Complex Web: Everything is Connected* https://www.cdc.gov/drugresistance/about/where-resistance-spreads.html.
5. Song, B. *et al.* Engineering and Application Perspectives on Designing an Antimicrobial Surface. *ACS Applied Materials and Interfaces* **12,** 21330–21341. ISSN: 19448252. doi:10.1021/acsami.9b19992 (2020).
6. Hall, T. J. *et al.* A call for action to the biomaterial community to tackle antimicrobial resistance. *Biomaterials Science* **8,** 4951–4974. doi:10.1039/d0bm01160f (2020).
7. Huang, W., Tao, F., Li, F., Mortimer, M. & Guo, L.-H. Antibacterial nanomaterials for environmental and consumer product applications. *NanoImpact* **20,** 100268. doi:https://doi.org/10.1016/j.impact.2020.100268 (2020).
8. Tyuftin, A. A. & Kerry, J. P. Review of surface treatment methods for polyamide films for potential application as smart packaging materials: surface structure, antimicrobial and spectral properties. *Food Packaging and Shelf Life* **24,** 100475. doi:10.1016/j.fpsl.2020.100475 (2020).
9. Cassini, A. *et al.* Attributable deaths and disability-adjusted life-years caused by infections with antibiotic-resistant bacteria in the EU and the European Economic Area in 2015: a population-level modelling analysis. *The Lancet Infectious Diseases* **19,** 56–66. doi:10.1016/S1473-3099(18)30605-4 (2019).
10. Centers for Disease Control and Prevention. *Antibiotic Resistance Threats In The United States - 2019* https://www.cdc.gov/drugresistance/pdf/threats-report/2019-ar-threats-report-508.pdf.
11. Zou, Y., Zhang, Y., Yu, Q. & Chen, H. Dual-function antibacterial surfaces to resist and kill bacteria: Painting a picture with two brushes simultaneously. *Journal of Materials Science & Technology* **70,** 24–38. doi:10.1016/j.jmst.2020.07.028 (2021).
12. Yu, Q., Wu, Z. & Chen, H. Dual-function antibacterial surfaces for biomedical applications. *Acta Biomaterialia* **16,** 1–13. doi:10.1016/j.actbio.2015.01.018 (2015).
13. Cassidy, S. S. *et al.* Antimicrobial surfaces: A need for stewardship? *PLOS Pathogens* **16,** 1–10. doi:10.1371/journal.ppat.1008880 (2020).
14. Ge, X. Antimicrobial biomaterials with non-antibiotic strategy. *Biosurface and Biotribology* **5,** 71–82. doi:10.1049/bsbt.2019.0010 (2019).
15. Tatarková, M., Tatarko, P. & Šajgalík, P. *Si_3N_4 Ceramics, Structure and Properties* in *Reference Module in Materials Science and Materials Engineering* (Elsevier, 2020). doi:https://doi.org/10.1016/B978-0-12-818542-1.00021-7.
16. Hardie, D. & Jack, K. Crystal Structures of Silicon Nitride. *Nature* **180,** 332–333. doi:https://doi.org/10.1038/180332a0.
17. Hampshire, S. *Silicon Nitride Ceramics* in *Engineered Ceramics* (John Wiley & Sons, 2016). doi:10.1002/9781119100430.ch5.
18. Riley, F. L. Silicon nitride and related materials. *Journal of the American Ceramic Society* **83,** 245–265. doi:10.1111/j.1151-2916.2000.tb01182.x (2000).
19. Kita, H., Hirao, K., Hyuga, H., Hotta, M. & Kondo, N. *Review and Overview of Silicon Nitride and SiAlON, Including their Applications* in *Handbook of Advanced Ceramics: Materials, Applications, Processing, and Properties* 2nd edition (Academic Press, 2013). doi:https://doi.org/10.1016/B978-0-12-385469-8.00015-0.
20. Rahaman, M. & Xiao, W. Silicon nitride bioceramics in healthcare. *International Journal of Applied Ceramic Technology* **15,** 861–872. doi:10.1111/ijac.12836 (2018).
21. Mobbs, R. J. *et al.* Anterior Lumbar Interbody Fusion Using Reaction Bonded Silicon Nitride Implants: Long-Term Case Series of the First Synthetic Anterior Lumbar Interbody Fusion Spacer Implanted in Humans. *World Neurosurgery* **120,** 256–264. doi:10.1016/j.wneu.2018.08.237 (2018).
22. Mussano, F., Genova, T., Munaron, L., Faga, M. G. & Carossa, S. *Ceramic Biomaterials for Dental Implants: Current Use and Future Perspectives* in *Dental Implantology and Biomaterial* (2016). doi:10.5772/62701.

23. Badran, Z. *et al.* Silicon nitride (Si_3N_4) implants: the future of dental implantology? *Journal of Oral Implantology* **43,** 240–244. doi:10.1563/aaid-joi-D-16-00146 (2017).
24. Lal, S., Caseley, E. A., Hall, R. M. & Tipper, J. L. Biological Impact of Silicon Nitride for Orthopaedic Applications: Role of Particle Size, Surface Composition and Donor Variation. *Scientific Reports* **8.** doi:10.1038/s41598-018-27494-y (2018).
25. McEntire, B. J. *et al.* Silicon nitride bearings for total joint arthroplasty. *Lubricants* **4,** 35. doi:10.3390/lubricants4040035 (2016).
26. Campoccia, D., Montanaro, L. & Arciola, C. R. A review of the biomaterials technologies for infection-resistant surfaces. *Biomaterials* **34,** 8533–8554. doi:10.1016/j.biomaterials.2013.07.089 (2013).
27. Pezzotti, G. Silicon Nitride: A Bioceramic with a Gift. *ACS Applied Materials and Interfaces* **11,** 26619–26636. doi:10.1021/acsami.9b07997 (2019).
28. Pezzotti, G. *et al.* Silicon Nitride Bioceramics Induce Chemically Driven Lysis in Porphyromonas gingivalis. *Langmuir* **32,** 3024–3035. doi:10.1021/acs.langmuir.6b00393 (2016).
29. Laarz, E., Zhmud, B. V. & Bergström, L. Dissolution and Deagglomeration of Silicon Nitride in Aqueous Medium. *Journal of the American Ceramic Society* **83,** 2394–2400. doi:10.1111/j.1151-2916.2000.tb01567.x (2004).
30. Silhavy, T. J., Kahne, D. & Walker, S. The bacterial cell envelope. *Cold Spring Harbor perspectives in biology* **2,** a000414. doi:10.1101/cshperspect.a000414 (2010).
31. Toltzis, P. *116 - Staphylococcus epidermidis and Other Coagulase-Negative Staphylococci* in *Principles and Practice of Pediatric Infectious Diseases (Fifth Edition)* 5th edition (Elsevier, 2018). doi:https://doi.org/10.1016/B978-0-323-40181-4.00116-X.
32. Oliveira, W. *et al.* Staphylococcus aureus and Staphylococcus epidermidis infections on implants. *Journal of Hospital Infection* **98,** 111–117. doi:10.1016/j.jhin.2017.11.008 (2018).
33. Otto, M. Staphylococcus epidermidis - The 'accidental' pathogen. *Nature Reviews Microbiology* **7,** 555–567. doi:10.1038/nrmicro2182 (2009).
34. Sakanaka, A., Takeuchi, H., Kuboniwa, M. & Amano, A. Dual lifestyle of Porphyromonas gingivalis in biofilm and gingival cells. *Microbial Pathogenesis* **94",** 42–47. doi:10.1016/j.micpath.2015.10.003 (2016).
35. Nakayama, M. & Ohara, N. Molecular mechanisms of Porphyromonas gingivalis-host cell interaction on periodontal diseases. *Japanese Dental Science Review* **53,** 134–140. doi:10.1016/j.jdsr.2017.06.001 (2017).
36. Challacombe, S. J., Shirlaw, P. J. & Thornhill, M. H. *Chapter 102 - Immunology of Diseases of the Oral Cavity* in *Mucosal Immunology* 4th edition (Academic Press, 2015). doi:https://doi.org/10.1016/B978-0-12-415847-4.00102-6.
37. Pye, A., Lockhart, D., Dawson, M., Murray, C. & Smith, A. A review of dental implants and infection. *Journal of Hospital Infection* **72,** 104–110. doi:10.1016/j.jhin.2009.02.010 (2009).
38. Fang, D. *et al.* A peptide coating preventing the attachment of Porphyromonas gingivalis on the surfaces of dental implants. *Journal of Periodontal Research* **55,** 503–510. doi:10.1111/jre.12737 (2020).
39. Smith, R., Wright, K. L. & Ashton, L. Raman spectroscopy: an evolving technique for live cell studies. *Analyst* **141,** 3590–3600. doi:10.1039/C6AN00152A (2016).
40. Delfino, I., Ricciardi, V., Manti, L., Lasalvia, M. & Lepore, M. Multivariate analysis of difference Raman spectra of the irradiated nucleus and cytoplasm region of SH-SY5Y human neuroblastoma cells. *Sensors* **19,** 3971. doi:10.3390/s19183971 (2019).
41. Pahlow, S. *et al.* Isolation and identification of bacteria by means of Raman spectroscopy. *Advanced Drug Delivery Reviews* **89,** 105–120. doi:10.1016/j.addr.2015.04.006 (2015).
42. Butler, H. J. *et al.* Using Raman spectroscopy to characterize biological materials. *Nature Protocols* **11,** 664–687. doi:10.1038/nprot.2016.036 (2016).
43. Kuhar, N., Sil, S., Verma, T. & Umapathy, S. Challenges in application of Raman spectroscopy to biology and materials. *RSC Advances* **8,** 25888–25908. doi:10.1039/c8ra04491k (2018).
44. Senger, R. S. & Scherr, D. Resolving complex phenotypes with Raman spectroscopy and chemometrics. *Current Opinion in Biotechnology* **66,** 277–282. doi:10.1016/j.copbio.2020.09.007 (2020).
45. Gautam, R., Vanga, S., Ariese, F. & Umapathy, S. Review of multidimensional data processing approaches for Raman and infrared spectroscopy. *EPJ Techniques and Instrumentation* **2.** doi:10.1140/epjti/s40485-015-0018-6 (2015).
46. Hanson, Bryan A. *ChemoSpec: Exploratory Chemometrics for Spectroscopy* https://cran.r-project.org/web/packages/ChemoSpec/ChemoSpec.pdf.
47. Beleites, C. and Sergo, V. *HyperSpec: Work with Hyperspectral Data* https://cran.r-project.org/web/packages/hyperSpec/hyperSpec.pdf.

2 Experimental techniques

This chapter aims at providing an outline of the techniques employed for the physico-chemical characterization of the silicon nitride powders as well as for biological tests on bacterial culture. Starting from vibrational spectroscopies, infrared (IR) in section 2.1 and Raman in section 2.2, then X-Ray photoelectron spectroscopy (XPS) is presented in section 2.3 and section 2.4 completes the first set of techniques with zeta potential measurements. Concerning the biological side, section 2.5 is dedicated to a colorimetric microbial viability assay named WST-8 assay. For each characterization method, the main theoretical principles are explained with particular attention on which type of information can be gained and why this is advantageous for the present study.

2.1 Infrared (IR) spectroscopy

In the field of vibrational spectroscopy, infrared (IR) spectroscopy is one of the most common techniques and relies on a simple principle. As the term "vibrational" suggests, among the contributions to the energy of a molecule, what is addressed with this type of spectroscopy are the vibrations of the nuclei which constitute the molecule. IR spectroscopy generally exploits radiation in the mid-infrared range (4000 - 400 cm^{-1}) to interact with matter and excite a transition between vibrational energy levels [1]. The transfer of energy from the photon to the molecule is based on an absorption process which depends on a resonance condition between the oscillating frequency of radiation and the frequency of a vibrational mode [2].

The displacements involved in vibrational motion can be described with the harmonic oscillator model. Quantum mechanical calculations allow to derive the energy levels corresponding to each vibrational state and the rule for a transition to be allowed. In the harmonic approximation this corresponds to a change of ± 1 in vibrational quantum number (v) between final and initial state ($\Delta v = \pm 1$). These transitions are called *fundamentals*; under ordinary temperature conditions it can be shown from the Boltzmann distribution function that most molecules are in the vibrational ground level (v=0) and the transition v=1 $\leftarrow$ v=0 dominates the IR absorption spectra [3]. Transitions that originate from higher levels are called *hot bands* because their relative intensity increases with temperature (as the population of those levels does). With the introduction of anharmonicity in the model, *overtones* and *combination*[1] bands can also result [1, 4].

Apart from the absorption frequency, a fundamental concept is that the absorption intensity depends on the effectiveness of the energy transfer to the molecule, which is related to the change in the dipole moment occurring with the molecular vibration [3]. The photon has an oscillating electric field that exerts opposite forces on the positive and negative centers of charge of the molecule, tending to induce a change in their spacing and an oscillation of the dipole moment at the same frequency. For some frequency values a forced dipole moment oscillation will lead to activation of a nuclear vibration. In other words, these values correspond to molecular vibrational frequencies at which the nuclear vibration causes a dipole moment change. Conversely, those molecular vibrations that do not involve changes in dipole moment cannot be activated by a forced dipole moment oscillation. This is usually summarized in a well-known selection rule: for a molecular vibration to be IR active it must cause a change in the dipole moment of the molecule [1, 3].

Further to this point, the importance of molecular symmetry cannot be disregarded since it determines whether a vibration involves a change in dipole moment or not. Molecules can be classified on

[1] Overtones are integer multiples of the fundamentals ($\Delta v = \pm 2, \pm 3$), whereas combination bands arise from the sum or difference of two or more fundamentals

the basis of their symmetry, enabling to derive simple relationships between molecular structure and vibrational spectrum. Furthermore, group theory can be applied to mathematically predict which vibrations will be active [1]. However, calculations become increasingly difficult with the complexity of the molecules and empirical methods based on the identification of functional groups are often employed. In fact it is verified that to certain groups of atoms correspond characteristic vibrational frequencies, regardless of the rest of the molecule [4]. These are called *group frequencies*.

Dealing with crystalline solids such as silicon nitride, it should be added that in these structures the vibrational motions can have two possible origins: internal vibrational modes (equivalent to those already discussed) and lattice-based vibrations. The latter, also called phonons, are due to the relative motion of individual atoms or polyatomic species in a crystalline lattice; with many atoms vibrating in unison a collective motion propagates throughout the crystal [5]. Lattice vibrations can be divided into acoustic and optical modes, but only optical modes interact with light and can be probed by IR and Raman spectroscopy. A further classification of these modes is into longitudinal optical (LO) and transverse optical (TO) phonons[2].

Through the analysis and interpretation of the spectra different types of information can be gained for the elucidation of molecular structures, the identification of composition (both qualitatively and quantitatively) and chemical environment [2]. As regarding the instrumentation and sampling, several configurations and systems exist but the main components are always a radiation source, some optical elements for focusing and a detector. Wavelength-sorting devices are used to separate the light emerging from the sample into individual wavelength components; today most of the IR spectrometers use an interferometer to accomplish the task [6]. A time-dependent signal is then converted into the final IR spectrum by computation of the Fourier Transform (FT). Among the possible acquisition modes a peculiar and powerful one is by attenuated total reflectance (ATR), which is discussed in the following subsection (2.1.1).

2.1.1 Attenuated Total Reflectance (ATR) spectroscopy

ATR is a sampling method for IR spectroscopy based on the phenomenon of total internal reflection (TIR), thus it requires an internal reflection element (IRE) with high refractive index and excellent transmission of IR radiation [6]. The physical process is schematized in Figure 1: the radiation reaching the interface between IRE and sample with an angle wider than the critical angle[3] is totally reflected but there is the formation of a so-called *evanescent wave* on the other side of the reflecting interface [8]. This wave interacts with a certain portion of the sample and in correspondence of an absorption by the tested material the intensity of the reflected light is attenuated with respect to the incident beam [9]. The resulting spectrum resembles the conventional transmission one, however in the case of ATR the penetration depth (d_p) is directly proportional to the incident radiation wavelength (λ) and also depends on the incidence angle (θ) and the refractive indices of the IRE (n_1) and sample (n_2) through the expression reported in Eq.1:

$$d_p = \frac{\lambda}{2\pi n_1[\sin^2\theta - (n_2/n_1)^2]^{1/2}} \tag{1}$$

[2]A longitudinal wave involves compression and expansion where the displacement is parallel to the wave propagation direction. A transverse wave involves shear and stress where the displacement is perpendicular to the wave propagation direction [5]

[3]the critical angle θ_c is such that there is no refraction, hence from Snell's law $\sin\theta_c = n_2/n_1$, where n_2 and n_1 are the refractive indices of sample and IRE respectively and $n_1 > n_2$ [7]

As a consequence, in IR-ATR spectra the absorbances at higher wavelengths are proportionally greater than at lower ones; other effects such as peak shifts and band shape distortions can also be observed [6].

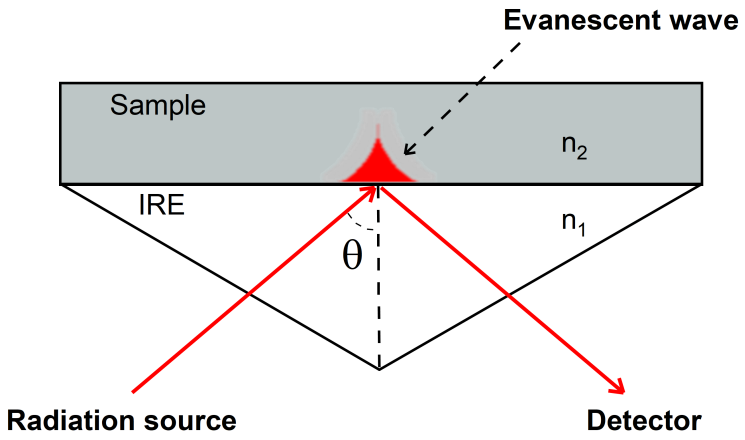

Figure 1: Schematic diagram of single reflection ATR: total internal reflection occurs at the boundary between IRE and sample, with the formation of an evanescent wave that penetrates into the sample. $\theta > \theta_c$, where "c" stands for "critical"; n_2 and n_1 are the refractive indices of sample and IRE respectively and it must be $n_1 > n_2$. The reflected light is then collected by a detector. Whenever the frequency of the source matches an absorption band of the sample the intensity of the reflected light is attenuated and a spectrum similar to the transmission one is obtained.

The collected signal of the reflected light is often converted into absorbance because it is more practical for subsequent procedures such as peak fitting. An *absorbance transform* is performed using the relationship $A = -\log_{10}(R)$, where A is absorbance and R is reflectance [10].

The ATR technique has become exceptionally popular since it is quick, nondestructive and it can analyze gases, liquids and solids (including films and powders) with basically no sample preparation [6]. Such characteristics are particularly suitable for the analysis of powders, in that powder samples can be directly placed on the ATR crystal and analyzed. In this regards, analysis is less laborious compared to transmission spectroscopy and diffuse reflection spectroscopy: in the first case skills to produce a pellet are required and the powder of interest must be mixed with another ("diluting") powder; in the second case no pellet is made but still careful mixing ratios and repeatable compaction of the mixture are needed [11]. With ATR the only need is to apply pressure on the neat powder to ensure appropriate contact with the IRE; collection and interpretation of the spectra are analogous to the case of other types of samples, and the powder can be recovered after the measurement.

In the present study FTIR-ATR spectroscopy is used to analyze Si_3N_4 powders by observing changes in the vibrational frequencies and inferring about if (and how) pH treatments can influence the crystalline structure of Si_3N_4.

2.2 Raman spectroscopy

Following from the previous section, Raman spectroscopy is a another type of vibrational spectroscopy and the information it can provide is similar to that obtained from IR spectroscopy, meaning the characteristic vibrational frequencies of the analyzed sample, which in turn help to elucidate the molecular structure of the material. In contrast with absorption and transmission phenomena, in this case the

technique is based on a scattering process. When a sample is irradiated with monochromatic radiation of frequency much higher than the vibrational frequencies (but lower than electronic frequencies) the incident photons can interact with the molecules of the sample which momentarily absorb the photon energy and get excited to an unstable virtual energy level [3]. With the subsequent de-excitation the molecule can return exactly to its original energy level, emitting a photon with the same energy of the incident photon, or it can fall to a different level, causing the emitted photon to differ in energy from the incident photon. In the former case the process can be viewed as an "elastic collision" between the photon and the molecule and is called *Rayleigh scattering*. Instead the latter type of "collision", named *Raman scattering* (after C. V. Raman [12]), is an inelastic one, since the energy of the molecule is changed by an amount equal to the difference between two vibrational levels ($\Delta E_{vib} = h\nu_{vib}$, where ν_{vib} is frequency of the involved molecular vibration). This amount is revealed as the energy difference between incident and scattered photon (for the conservation of energy). Considering this last process more in detail, two cases can be outlined: a) the molecule is initially in the ground vibrational level ($v = 0$), is brought to a high energy virtual state and, after de-excitation, falls to the vibrational level $v = 1$; b) the molecule is initially in the vibrational state $v = 1$ and then falls down to the ground vibrational level. These pathways are called Stokes and anti-Stokes Raman scattering, respectively [3]. The energy levels involved in the different transitions are schematized in Figure 2.

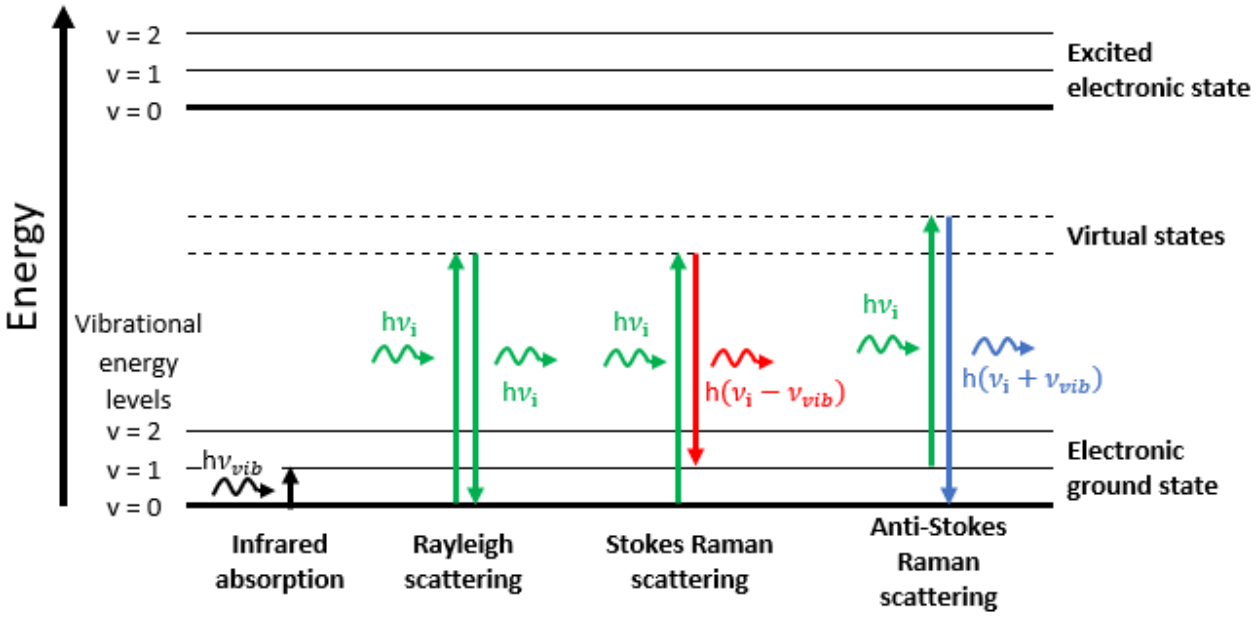

Figure 2: Energy levels involved in Rayleigh and Raman scattering and IR absorption. From left to right: in infrared absorption the molecule transitions to a higher vibrational level by absorbing an incident photon with the exact energy of the involved molecular vibration, $h\nu_{vib}$. In Rayleigh scattering the molecule is excited to a virtual state and then returns to its initial energy level, emitting a photon of frequency equal to the incident one. In Raman Stokes scattering, after excitation, the molecule falls down to a vibrational level higher than the initial one; the molecule has gained energy while the scattered photon has lower energy ($h\nu_s = h(\nu_i - \nu_{vib})$) compared to the incident one ($h\nu_i$), and precisely their difference is given by $\Delta E_{vib} = h\nu_{vib}$. In the last case, anti-Stokes Raman scattering occurs when the molecule returns to a vibrational level lower than the initial one. The molecule has lost an energy amount, which is gained by the scattering photon (with respect to the incident one). Again the absolute energy difference between the two photons coincides with the energy of the molecular vibration involved between the two vibrational levels, $h\nu_{vib}$.

The Raman spectrum reports the intensity of the scattered radiation as a function of the frequency difference $\Delta\nu$ between incident and scattered photon, the "Raman shift", usually expressed in wavenumber units (cm^{-1}). According to the Raman processes explained above, peaks appear in this spectrum when $\Delta\nu = \pm\nu_{vib}$, so that peaks are intrinsically linked to molecular vibrations and often in the abscissa only "wavenumber (cm^{-1})" is reported. Considering a given vibration, the ratio between the number of molecules in $v = 1$ state and those in the $v = 0$ state is given by the Boltzmann distribution function which indicates that at ordinary temperatures most of the molecules are in the vibrational ground level ($v = 0$) [3]. For this reason Stokes Raman signals have significantly greater intensities compared to anti-Stokes ones and therefore only the Raman Stokes part of the spectrum is usually recorded and reported in conventional Raman spectroscopy.

Among the outlined scattering processes, Rayleigh scattering is the most probable pathway, while only a small proportion of the molecules in the unstable energy level will de-excite through the Raman pathways: Rayleigh-scattered radiation intensity is $\sim 10^{-3}$ times the intensity of the incident radiation, whereas for Raman scattering the value goes down to $\sim 10^{-6}$ [1]. However, Rayleigh scattering does not provide information on molecular vibrations and this radiation must be filtered out in order to appreciate the Raman signals. In practice the instrumental setup typically includes: a laser source, which is focused on the sample; an optical collection system designed to maximize the collected Raman scattered radiation while eliminating the stronger Rayleigh part; a wavelength-sorting device or spectral analyzer (monochromators in dispersive systems and interferometers in Fourier Transform (FT) instruments) and a detector [6].

A fundamental remark is that not all molecular vibrations are "Raman active", i.e. can give rise to a signal in the Raman spectrum. In fact, the intensity of a spectral band relies on how effectively the energy is transferred from radiation to molecule [3]. The oscillating electric field of the electromagnetic radiation induces in the molecule an oscillating dipole moment μ (with the same frequency), which from classical theory is known to emit radiation in all directions (still with the same frequency). Some molecular vibrations can cause the molecule polarizability to vary and it can be shown that these changes result in an amplitude modulation of the induced oscillating dipole moment. In particular the expression of μ can be resolved into three components, each corresponding to a scattering pathway: one component has Rayleigh frequency while the other two have Stokes and anti-Stokes Raman frequencies, respectively. The amplitude of the first component is proportional to the equilibrium polarizability of the molecule, whereas the amplitude of the other two components is proportional to variations in polarizability. This means that when a molecular vibration does not cause a change in polarizability the Raman-frequency components of the induced dipole have zero amplitude and cannot provide a signal. In summary, the Raman selection rule can be expressed as: "in order for a molecular vibration to be Raman active, the vibration must be accompanied by a change in the polarizability of the molecule" [3].

In analogy with IR spectroscopy, the frequency, intensity and shape of Raman vibrational bands depends on the structure and dynamics of the molecules as well as on the chemical environment of the bonds. Hence, this type of information can be derived from the analysis of a Raman spectrum [2]. In principle each molecule has its own "fingerprint" or signature and its structure could be elucidated, but rather than understanding the absolute structure it is often preferred and more effective to monitor changes in the spectrum of a sample in response to some external perturbation [13]. This is particularly the case for biological systems, which yield fairly complex and convoluted spectra. Characteristic group frequencies are used as a basis to reveal which functional groups are present and how they are affected by the perturbation.

In the present study Raman spectroscopy is first used to characterize Si_3N_4 powders and evaluate if (and how) their treatment with solutions of different pH can influence the crystalline structure. Additionally, the technique is used to assess changes in the Raman bands of bacterial samples cultured in presence of Si_3N_4 at different pH, in the attempt of shedding light on the chemical and biological interactions of silicon nitride with the microorganisms.

2.3 X-ray photoelectron spectroscopy

The analysis of surfaces is of utmost importance in materials science because the surface of each material is involved in its interaction with the surroundings. These interactions are influenced by the nature of surfaces, therefore it is often necessary to investigate the surface physical and chemical properties. X-ray photoelectron spectroscopy (XPS) is one of the most common and used techniques for surface analysis [14]. The fundamental components of the electron spectrometer are: an excitation source (in this case a source of X-ray radiation), an electron energy analyzer and the specimen on a sample holder, all mounted in a vacuum chamber. The vacuum has a twofold purpose: to avoid contributions to the spectra by surface contamination and to avoid the scattering of emitted electrons by gas molecules between sample and analyzer [15]. The method in fact is based on a photoemission process in which X-ray photons with characteristic energy $h\nu$ impinge on the sample and interact with electrons of the atomic shells. The photon energy is transferred to the electrons that surmount their binding energy E_b (with respect to the Fermi level, E_F) and gain kinetic energy with which they start moving through the solid, being subject to scattering processes. An electron that is only elastically scattered can reach the sample surface without energy losses; here, after overcoming the sample workfunction (Φ_S), it is finally emitted in vacuum. The emitted electron (or photoelectron) travels to the analyzer with an energy given by $h\nu$ - E_b - Φ_S but the analyzer measures this energy diminished by Φ_A - Φ_S, where Φ_A is the analyzer workfunction [16]. So the measured kinetic energy is: $E_{kin} = h\nu - E_b - \Phi_S - (\Phi_A - \Phi_S)$ or simply $E_{kin} = h\nu - E_b - \Phi_A$. A scheme elucidating the relevant energy terms is presented in Figure 3.

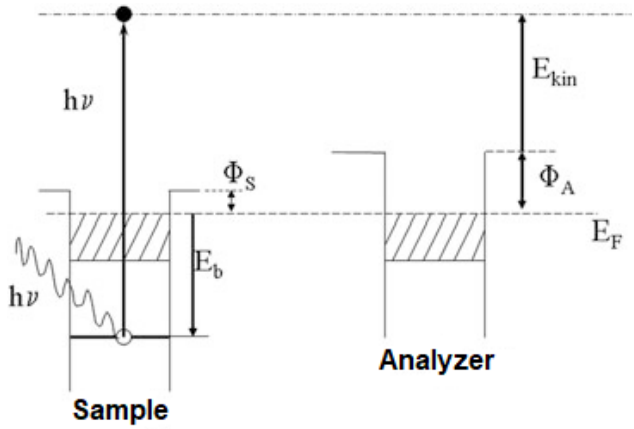

Figure 3: Relevant energy terms in photoemission: $h\nu$ is the energy of the X-ray photon impinging on the material, E_b is the binding energy of the electron excited by the photon, Φ_S is the sample workfunction, Φ_A is the analyzer workfunction, E_F is the Fermi level (in this case it is equal for sample and analyzer, considering both to be conductive materials). Adapted from [16].

The intrinsic material property is the electron binding energy, therefore the equation is usually reported as $E_b = h\nu$ - E_{kin} - Φ_A [4]. In practice, these calculations are performed by the data system associated to the detector and the operator directly selects an energy scale (binding or kinetic energy) for the data representation in the spectrum, which consists of a graph of intensity (counts or counts per second) as a function of the electron energy. Electrons that undergo inelastic scattering lose part of their energy and, if reaching the analyzer, contribute to the spectrum as background signals [15].

Since the electrons' binding energies are characteristic of the element of their origin, the first step of the analysis usually involves the recording of a survey spectrum (wide scan) over an energy range that provides strong peaks for almost all the elements of the periodic table (0-1000 eV range). This step allows the mere assessment of the elements present in the sample [15]. Subsequently, other spectra are acquired with higher resolution around the peaks of the elements of interest (narrow scan). Here information about the chemical state of the elements can be obtained because chemical bonding and changes of effective charge on an atom can affect the electron binding energies ("chemical shift"), as well as the peak shape and width [16]. The interpretation of the chemical shifts is commonly performed by comparison with standard spectra of compounds reported and tabulated in handbooks and databases.

Quantitative analysis of XPS spectra can also be performed in order to derive atomic concentrations from the measured photoelectrons intensities. To this purpose, data processing procedures such as background subtraction and decomposition of overlapping peaks are crucial and several factors, both sample-related and instrument-related, are involved in the mathematical relation between peak intensity and concentration [16]. Detection limits usually range between 0.1 and 0.5 at% [17].

The high surface sensitivity of this characterization technique arises from the fact that electrons in solids can only travel short distances without experiencing energy losses. In particular, the depth from which the characteristic photoelectrons can escape unaffected is typically limited a few nanometers [16]. Two relevant parameters that determine the surface sensitivity of XPS are the inelastic mean free path (IMFP), defined as the mean distance travelled by an electron before its engagement in an inelastic scattering process, and the attenuation length (λ), a characteristic decay length which takes into account both elastic and inelastic scattering. These parameters vary with electron energy and material properties [15].

In the present study XPS is used to characterize Si_3N_4 powders, specifically addressing changes in surface structure after conditioning the powders in solutions with different pH values for selected time intervals.

2.4 Zeta potential measurements

Surface chemistry and in particular the surface charges of particles immersed in a liquid affect processes at the solid-liquid interface, such as the adsorption of ions, as well as the interaction among particles (which in turn affects the stability towards aggregation) but also the sedimentation behavior [18]. In the attempt to explain these interfacial phenomena it is important to gain information about the electrical potential in the proximity of the particles. A key concept is that of electrical double layer, where the zeta potential (ζ) finds its definition. Distinct layers develop in the liquid surrounding a solid particle in suspension: in the immediate neighbourhood of the particle there are ions compactly adsorbed on the solid, forming what is called the Stern layer, whereas going further out the ions are non-uniformly

[4] It has to be noted that this equation is strictly valid only for conductive samples, which have the same E_F as the analyzer, while for insulators there may be an energy shift [16]

distributed in a "diffuse" layer, in which the charge density varies with the distance from the interface until reaching the same conditions of the bulk liquid [19]. In the diffuse layer lies an imaginary surface called *surface of shear* within which the fluid is stationary with respect to the solid [18], i.e. if the particle and the bulk liquid are in relative motion, then the fluid contained between the particle surface and the surface of shear moves along with the particle (as a kinetic unit). The zeta potential is defined as the electrical potential at the surface of shear with respect to a location in the bulk of the fluid. To better visualize this theoretical construction a schematic of the different layers and surfaces with the respective potentials is reported in Figure 4.

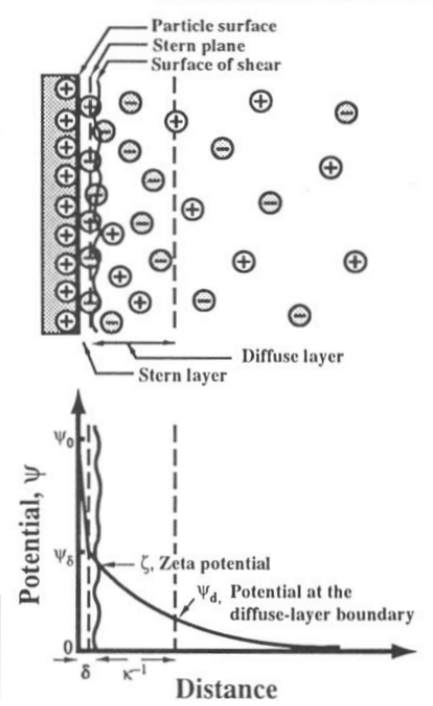

Figure 4: Schematic illustration of charge distribution and potential in the electrical double layer. **Top**: charge distribution in the solid and liquid phase. In the latter there is an inner (Stern) layer of adsorbed ions and an outer (diffuse) layer that fades into the bulk of the liquid. The Stern plane is located at a distance δ from the particle surface, passing through the center of the adsorbed ions. **Bottom**: electrical potential as a function of the distance from the particle surface (here assumed to be positively charged). ψ_0 and ψ_δ are the potential at the solid surface and at the Stern plane, respectively. κ^{-1} is the reciprocal of the Debye-Hückel parameter. Adapted from [20].

The zeta potential is a modeled quantity, not directly measured but rather calculated, and in general the measured quantity is an electrokinetic parameter called *electrophoretic mobility* (EPM). Considering a system composed of a solid phase dispersed in a liquid phase, with charges distributed at the interface in the form of a double layer, *electrokinetic effects* are those phenomena which arise when one phase moves tangentially past the second phase [18]. If an electric field is applied to induce the movement of solid particles through the liquid, the process is called *electrophoresis* and the EPM is the particle velocity per unit electric field. The most common measurement technique is based on electrophoretic light scattering (ELS): a dispersion is introduced into a cell containing two electrodes across which a voltage is applied, causing migration of the charged particles; simultaneously the dispersion is illuminated by a laser light source and the light scattered by the moving particles is sampled by an optical system connected to a photodetector. A signal processing system then allows to obtain the particle mobility from shifts in either the frequency or the phase of the scattered light (measured with respect to a reference laser beam) [21].

Different models have been proposed for the relation between EPM and ζ, all based on the balance between electric and viscous forces but with different assumptions on the properties of both the particle

and the liquid (references [22, 23] provide a thorough treatment). Of fundamental importance is Henry's equation:

$$u = \frac{v}{E} = \frac{2\varepsilon\zeta F(\kappa a)}{3\eta} \tag{2}$$

for non-conductive spherical particles, where u is the electrophoretic mobility ($m^2 \cdot s^{-1} \cdot V^{-1}$), v is the particle velocity, E is the electric field strength, ε and η are the dielectric constant and the viscosity of the liquid, respectively; $F(\kappa a)$ is a dimensionless function called Henry's function, which depends on the particle radius (a) and the Debye-Hückel parameter (κ) [23]. κ depends on the strength and concentration of electrolytes in the liquid [19]. In the limit of $\kappa a \to \infty$ Henry's function takes the value $3/2$, while for $\kappa a \to 0$ then $F(\kappa a) \to 1$. The former case, known as the Smoluchowski approximation, is valid for systems in which the double layer is thin compared to the particle size ($\kappa a > 100$), whereas the latter is the case of systems with thick double layer ($\kappa a < 0.1$) and coincides with Hückel model [23]. In most measurement systems a software allows to vary Henry's function according to the knowledge of particle size and solution ionic strength; the chosen value can significantly affect the resulting zeta-potential value. Usually the Smoluchowski approximation holds for particles of hundreds of nanometers in diameter suspended in aqueous media [24].

A relevant factor that can induce physical or chemical changes on the particles, affecting their surface charge, is the pH of the liquid. Variations in both magnitude and sign of the zeta potential are seen when the pH is shifted from low to high values and the pH value at which $\zeta = 0$ is termed the isoelectric point (IEP, pH_{iep}). Monitoring these changes can serve as an indicator of the stability of a system as well as a diagnostic for particle surface changes in different systems, hence the measurement of ζ is frequently performed as a function of pH [24].

In the present study the measurement of zeta potential is performed on treated and non-treated Si_3N_4 powders. The treatments consist in the immersion of the powder in solutions with different pH for selected time intervals, prior to the electrokinetic measurements. The aim is to evaluate if and how the prolonged exposure of Si_3N_4 powder to different pH can influence its electrokinetic behavior, providing a basis for inference on the possible changes in surface functionalities.

2.5 Microbial viability assays

Different types of assays are available for the assessment of microbial viability, often based on the measurement of a biochemical marker to evaluate metabolic activity of the cells. Colorimetric assays exploit reagents that develop a color in response to some cellular metabolic process; then the color can be promptly monitored with a spectrophotometer. These assays are easy to perform and applicable for both adherent and suspended cell lines [25]. Several commercial kits are accessible and usually contain experimental procedures and guidelines; the kit used in this study is the WST-8 kit by Dojindo [26].

WST stands for Water-Soluble Tetrazolium salts, of which many variants have been synthesized. In the presence of an electron mediator, the salt can be reduced to a water-soluble formazan dye, but for the reaction to occur it is essential to have activity of a cellular reducing agent such as NAD(P)H. Therefore the production of formazan is proportional to the NAD(P)H concentration, which is linked to the number of viable microorganisms [27]. The process is schematized in Figure 5. In the specific case of WST-8[5] the formazan product has an orange color whose maximum absorption wavelength is around 450-460 nm. It is worth noting that the formazan product of WST-8 is water soluble, meaning

[5] 2-(2-methoxy-4-nitrophenyl)-3-(4-nitrophenyl)-5-(2,4-disulfophenyl)- 2H tetrazolium, monosodium salt

that there is no requirement of solubilization prior to the spectrophotometric detection. The method therefore becomes applicabile in real-time assays and it is advantageous compared those in which the tetrazolium salt is reduced into an insoluble formazan (e.g. MTT[6]) [28].

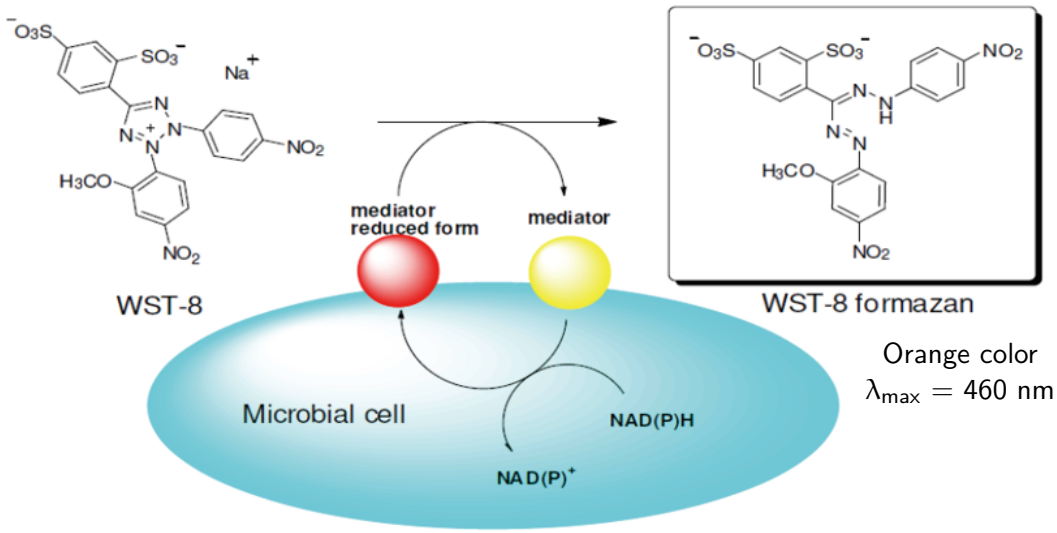

Figure 5: Schematics of the reactions in the WST-8 assay, adapted from [26]. λ_{max} is the wavelength corresponding to the absorption maximum of the formazan product.

Assays using WST-8 are more sensitive than the ones with WST-1[7], especially at neutral pH [29]. Furthermore, the WST-8 method displays greater reactive efficiency for measuring bacterial viability compared to assays based on the tetrazolium salt XTT[8], moreover in antimicrobial susceptibility applications WST-8 was reported to be comparably effective but significantly more rapid with respect to the standard broth microdilution method [28]. An additional point is that WST-8 is not cell permeable, thus resulting in low cytotoxicity [25]. Despite the advantages, it is important to carefully consider that changes in intracellular metabolic activity which may have no effect on the cell viability can also impact on the reduction of the assay substrates [25]. Comprehensively, the WST-8 colorimetric method is very appealing and useful for rapid determination of NAD(P)H and is considered a valuable tool for monitoring cell viability [27].

In this study the assay was used to assess the effects of Si_3N_4 powders on the viability of two bacterial strains, namely *S. epidermidis* (ATCC® 14990™) and *P. gingivalis* (ATCC® 33227™). The tests were performed on the bacterial cultures after treatments with the powders in different pH conditions and for multiple time frames.

[6] 2-(4,5-dimethyl-2-thiazolyl)-3,5-diphenyl-2H-tetrazolium bromide
[7] 2-(4-iodophenyl)-3-(4-nitrophenyl)-5-(2,4-disulfophenyl)-2H tetrazolium, monosodium salt
[8] 2,3-bis(2-methyloxy-4-nitro-5-sulfophenyl)-5-[(phenylamino)carbonyl]-2H-tetrazolium hydroxide

References

1. Larkin, P. J. *Chapter 2* in *Infrared and Raman Spectroscopy* 2nd edition (Elsevier, 2018). doi:10.1016/C2015-0-00806-1.
2. Larkin, P. J. *Chapter 1* in *Infrared and Raman Spectroscopy* 2nd edition (Elsevier, 2018). doi:10.1016/C2015-0-00806-1.
3. Colthup, N. B., Daly, L. H. & Wiberley, S. E. *Chapter 1* in *Introduction to Infrared and Raman Spectroscopy* 3rd edition (Academic Press, 1990). doi:10.1016/B978-0-08-091740-5.50004-1.
4. Nakamoto, K. *Chapter 1* in *Infrared and Raman Spectra of Inorganic and Coordination Compounds* 6th edition (John Wiley & Sons, 2008). doi:10.1002/9780470405888.
5. Larkin, P. J. *Chapter 4* in *Infrared and Raman Spectroscopy* 2nd edition (Elsevier, 2018). doi:10.1016/C2015-0-00806-1.
6. Larkin, P. J. *Chapter 3* in *Infrared and Raman Spectroscopy* 2nd edition (Elsevier, 2018). doi:10.1016/C2015-0-00806-1.
7. Milosevic, M. *Chapter 4* in *Internal reflection and ATR spectroscopy* (John Wiley & Sons, 2012). doi:10.1002/9781118309742.
8. Milosevic, M. *Chapter 1* in *Internal reflection and ATR spectroscopy* (John Wiley & Sons, 2012). doi:10.1002/9781118309742.
9. Colthup, N. B., Daly, L. H. & Wiberley, S. E. *Chapter 2* in *Introduction to Infrared and Raman Spectroscopy* 3rd edition (Academic Press, 1990). doi:10.1016/B978-0-08-091740-5.50004-1.
10. Milosevic, M. *Chapter 4* in *Internal reflection and ATR spectroscopy* (John Wiley & Sons, 2012). doi:10.1002/9781118309742.
11. Milosevic, M. *Chapter 19* in *Internal reflection and ATR spectroscopy* (John Wiley & Sons, 2012). doi:10.1002/9781118309742.
12. Raman, C. V. & Krishnan, K. S. A new type of secondary radiation. *Nature* **121,** 501–502. doi:10.1038/121501c0 (1928).
13. Kuhar, N., Sil, S., Verma, T. & Umapathy, S. Challenges in application of Raman spectroscopy to biology and materials. *RSC Advances* **8,** 25888–25908. doi:10.1039/c8ra04491k (2018).
14. Baer, D. R. *et al.* Practical guides for x-ray photoelectron spectroscopy: First steps in planning, conducting, and reporting XPS measurements. *Journal of Vacuum Science & Technology A* **37,** 031401. doi:10.1116/1.5065501 (2019).
15. Watts, J. F. & Wolstenholme, J. *An Introduction to Surface Analysis by XPS and AES* 2nd edition. doi:10.1002/9781119417651 (John Wiley & Sons, 2019).
16. Hofmann, S. *Auger- and X-Ray Photoelectron Spectroscopy in Materials Science: A User-Oriented Guide* doi:10.1007/978-3-642-27381-0 (Springer, 2013).
17. Oswald, S. *X-Ray Photoelectron Spectroscopy in Analysis of Surfaces* in *Encyclopedia of Analytical Chemistry* (John Wiley & Sons, 2013). doi:10.1002/9780470027318.a2517.pub2.
18. Hunter, R. J. *Chapter 1: Introduction* in *Zeta Potential in Colloid Science* (Academic Press, 1981). doi:10.1016/C2013-0-07389-6.
19. Hunter, R. J. *Chapter 2: Charge and potential distribution at interface* in *Zeta Potential in Colloid Science* (Academic Press, 1981). doi:10.1016/C2013-0-07389-6.
20. Hiemenz, P. C. & Rajagopalan, R. *Chapter 11: The electrical double layer and double-layer interactions* in *Principles of Colloid and Surface Chemistry* 3rd edition (CRC Press, 1997). doi:10.1201/9781315274287.
21. Corbett, J. C. & McNeil-Watson, F. *Electrophoretic Light Scattering* in *Encyclopedia of Biophysics* (Springer, 2018). doi:10.1007/978-3-642-35943-9_288-1.
22. Hunter, R. J. *Chapter 3: The calculation of Zeta potential* in *Zeta Potential in Colloid Science* (Academic Press, 1981). doi:10.1016/C2013-0-07389-6.
23. Hiemenz, P. C. & Rajagopalan, R. *Chapter 12: Electrophoresis and other electrokinetic phenomena* in *Principles of Colloid and Surface Chemistry* 3rd edition (CRC Press, 1997). doi:10.1201/9781315274287.
24. Lowry, G. V. *et al.* Guidance to improve the scientific value of zeta-potential measurements in nanoEHS. *Environmental Science: Nano* **3,** 953–965. doi:10.1039/c6en00136j (2016).
25. Aslantürk, Ö. S. *In Vitro Cytotoxicity and Cell Viability Assays: Principles, Advantages, and Disadvantages* in *Genotoxicity - A Predictable Risk to Our Actual World* (2018). doi:10.5772/intechopen.71923.
26. Dojindo. *Microbial Viability Assay Kit-WST* https://www.dojindo.eu.com/store/p/141-Microbial-Viability-Assay-Kit-WST.aspx.
27. Chamchoy, K., Pakotiprapha, D., Pumirat, P., Leartsakulpanich, U. & Boonyuen, U. Application of WST-8 based colorimetric NAD(P)H detection for quantitative dehydrogenase assays. *BMC Biochemistry* **20.** doi:10.1186/s12858-019-0108-1 (2019).
28. Tsukatani, T. *et al.* Colorimetric microbial viability assay based on reduction of water-soluble tetrazolium salts for antimicrobial susceptibility testing and screening of antimicrobial substances. *Analytical Biochemistry* **393,** 117–125. doi:10.1016/j.ab.2009.06.026 (2009).
29. Tominaga, H. *et al.* A water-soluble tetrazolium salt useful for colorimetric cell viability assay. *Analytical Communications* **36,** 47–50. doi:10.1039/a809656b (1999).

3 Characterization of Si_3N_4 powders

The aim of this Chapter is to report about the experiments performed with Si_3N_4 powders to assess the effects of pH treatments on the powder itself. The powders were immersed in culture media in five different pH conditions, for up to 24h and 72h, then characterized. The pH values at the onset of the treatment were: pH 5.5, 6.5, 7.5, 8 and 8.5.

3.1 Materials and methods

3.1.1 Powder treatment

The powders used in this study were commercially available Si_3N_4 powders (99% β-Si_3N_4) with average particle size d_{50} [9] = 0.9 μm and density 3.19 g/cm^3, as indicated by the manufacturer. The treatments were designed as to replicate the conditions to which the powder was exposed during the tests with bacteria, therefore the powders had to be immersed in culture medium. In particular, brain heart infusion (BHI) broth was prepared and modified to obtain specific pH values. The starting liquid had pH 7.5, then it was added with tetraborate [10] to achieve more alkaline conditions: pH 8 and pH 8.5. Analogously, two batches of more acidic media were prepared by adding phtalate [11] to the starting BHI broth, obtaining the pH values 6.5 and 5.5. For each sample an eppendorf tube was filled with 1 mL of medium where the Si_3N_4 powder was dispersed, in the ratio of 16 mg/mL. The vials were closed and placed on a rotator to ensure constant agitation of the powder and prevent its deposition on the bottom of the tube. A complete set of vials, containing all the five pH treatments, was withdrawn from the rotator after 24h while a second complete set after 72h. At this point the samples were centrifuged at 10000 rpm for 3 min at 4 °C and the liquid phase was removed. In order to remove glucose and other nutrients that may remain on the powders, three washing steps were performed: the first two times with deionized water and the last one with ethanol. Each step was followed by centrifugation with the aforementioned parameters. Lastly the ethanol phase was discarded and the powders were left to dry overnight under a chemical fume hood, then the samples were stored in closed vials and ready for characterization.

3.1.2 FTIR spectroscopy

Infrared spectra were collected with the Jasco spectrometer FT/IR-4700 (Jasco, Easton, MD, USA) equipped with a single-reflection ATR accessory having a diamond prism as internal reflection element (IRE), allowing acquisitions in the range 400-4000 cm^{-1}. The angle of incidence of the light source on the IRE was 45°. No sample preparation was required and the powders were simply spread onto the ATR crystal (contact area diameter = 1.8 mm) and pressure was applied using an integrated clamp in order to ensure good contact between sample and IRE. Three measurements were performed for each sample and each output was the result of the average of 60 consecutive acquisitions. An ATR correction algorithm (available in the acquisition software Jasco Spectra Manager) was applied on the raw spectra, then the signal was converted from reflectance to absorbance through the relationship $A = -\log_{10}(R)$, where A is absorbance and R is reflectance. Baseline subtraction, normalization and peak deconvolution were then carried out using the softwares LabSpec (Horiba, Kyoto, Japan) and OriginPro 2018 (OriginLab Corp., Northampton, Massachusetts).

[9] Considering the particle size distribution, d_{50} is the median diameter, for which 50% of the distribution has smaller size and 50% larger size

[10] tetraborate pH standard solution, pH 9.18 (25°C), FUJIFILM Wako Pure Chemical Corporation

[11] phtalate pH standard solution, pH 4.01 (25°C), FUJIFILM Wako Pure Chemical Corporation

3.1.3 Raman spectroscopy

The instrument used in these experiments was the triple configuration Raman spectrometer T64000 (Jobin-Ivon/Horiba Group, Kyoto, Japan) equipped with a charge-couple device (CCD) detector. A green laser was used as light source (Argon ion laser), with excitation wavelength 514 nm and nominal operating power of around 200 mW. The spectrometer was provided with an integrated confocal microscope with a pinhole of aperture-diameter 100 μm for shallowing the probe to the order of few μm in depth; the lateral resolution was in the order of 1 μm. For analysing the powders it was necessary to sprinkle them onto an adhesive tape previously placed on a sample stub. The sample was then placed on the stage under a 100x objective lens. The focus was manually adjusted before acquiring the spectra, which were collected in square maps using an automated, two-axes sample stage. The maps were 30×30 μm^2 with a step of 10 μm, for a total of 9 spectra for each sample, where each spectrum was the average of 14 successive acquisitions in the same point (each with an exposure time of 8 s). In terms of spectral region, the acquisition was run in the extended range mode, defining two intervals: from 150 to 675 cm^{-1} and from 650 to 1100 cm^{-1}. Post-processing of the spectra (i.e. baseline subtraction, normalization and fitting) was carried out using the softwares LabSpec 5 (Horiba, Kyoto, Japan) and OriginPro 2018 (OriginLab Corp., Northampton, Massachusetts).

3.1.4 X-ray photoelectron spectroscopy

XPS measurements were executed with the JPS-9010 photoelectron spectrometer (JEOL Ltd., Tokyo, Japan) using a monochromatic source of MgK_α X-rays (10 kV, 10 mA). Analogously to the preparation of Raman samples, in this case the powders were sprinkled onto carbon conductive tape previously placed onto the sample holder. The analyses were performed in a vacuum chamber at $\sim 2 \cdot 10^{-7}\,\mathrm{Pa}$. For each sample first a survey scan was conducted, with a voltage step of 1 eV and five scan repetitions, then narrows scans were acquired in the regions of interest for Si_3N_4 using a voltage step of 0.1 eV and 10 scan repetitions. In both the wide scan and the narrow scans the dwell time was 100 ms. The following energy regions were investigated with the narrow scans: 98-112 eV for emissions from silicon atoms (Si2p), 280-295 eV for carbon (C1s), 394-409 eV for nitrogen (N1s) and 526-544 eV for oxygen (O1s). Referencing of the binding energy (BE) scale was accomplished using the acquired C1s spectrum from adventitious carbon and setting the C–C component to 284.8 eV. Shirley background removal was applied to each raw spectrum from the software supplied with the instrument (SpecXPS 1.2, Jeol). Peak deconvolution was carried out with the commercially available software LabSpec (Horiba, Kyoto, Japan) using mixed Gaussian-Lorentzian functions.

3.1.5 Zeta potential measurements

The instrument used in this study was the Zeta-potential & particle size analyzer ELSZ-2000 (Otsuka Electronics Co., Ltd., Osaka, Japan) complemented with the pH titrator system ELSZ-PT for automatic titration of the samples, allowing to obtain the zeta potential as a function of pH. Essential parameters have to be defined before the measurements and concern both the powders and the electrolyte solution used as medium during the analyses. It is important to report solution conditions, material properties and theoretical model, since these factors affect the calculated zeta-potential value. A number of articles in the literature report about zeta potential measurements of Si_3N_4 powders and the parameters of interest that were used in such studies are summarized in Table I.

Table I: Zeta potential measurement technique and experimental conditions in reference studies

Ref.	Measurement	Particle size	Solid loading	Electrolyte	Titration solutions
[1]	ELS	$d_{50} = 0.75$ µm	0.015 vol %	NaCl 0.01 M	not specified
[2]	ESA	$d_{50} = 0.50$ µm	2 vol %	NaCl 0.01 M	NH_4OH and HCl
[3]	ESA	$d_{avg} = 0.40$ µm	10 vol %	NaCl 0.01 M	not specified
[4]	ELS	$d_{avg} = 0.42$ µm	0.01 vol %	KCl 0.001 M	NH_4OH and HNO_3

ELS = Electrophoretic Light Scattering; ESA = Electroacoustic Sonic Amplitude;

d_{50} = median particle diameter, referring to the particle size distribution

d_{avg} = mean particle diameter, when reference articles did not refer to the size distribution

Considering the Si_3N_4 samples of this study, the average particle size as reported by the manufacturer was $d_{50} = 0.9$ µm and the zeta-potential measurement technique was Electrophoretic Light Scattering (ELS), hence the other parameters were selected as follows:

- **Electrolyte**: NaCl 0.01M
- **Titration solutions**: NaOH and HCl, both 1 M;
- **Solid loading** in the electrolyte solution: 0.015 vol %, which corresponds to 5 mg of powder in 10 mL of liquid.

The zeta potential measurements were conducted in the range from pH 4 to pH 11, with acquisition steps of $\Delta pH \simeq 1$.

The system to be analyzed was composed of particles of hundreds of nanometers in diameter suspended in aqueous media with moderate electrolyte concentration, therefore the Smoluchowski approximation was applied for the relationship between electrophoretic mobility and Zeta potential [5], which then reads as:

$$u = \frac{v}{E} = \frac{\varepsilon\zeta}{\eta} \tag{3}$$

for non-conductive spherical particles, where u is the electrophoretic mobility ($m^2 \cdot s^{-1} \cdot V^{-1}$), v is the particle velocity, E is the electric field strength, ζ is the zeta potential, ε and η are the dielectric constant and the viscosity of the liquid medium, respectively.

3.2 Results

3.2.1 FTIR spectroscopy

3.2.1.1 Average spectra and peak fitting

The FTIR spectrum of Si_3N_4 powders was divided in two spectral windows: range 1 from 400 cm^{-1} to 650 cm^{-1} and range 2 from 650 cm^{-1} to 1250 cm^{-1}. More evident changes were present in the second range when comparing the spectra of untreated and treated powders, therefore the subsequent analyses only focused on range 2. All the spectra were normalized from 0 to 1 and a visual comparison of the average spectra of the different samples is reported in Figure 6, where the top row contains graphs from the powders treated for 24h while the bottom row contains the 72h treatment groups. A broadening of the overall spectral shape can be appreciated for the sample treated at pH 5.5 for 24h (top left panel) and for all the 72h-treated samples (bottom panels). A shift towards lower wavenumbers seems to be present in many of the treatment groups, but most likely it is an apparent feature generated by a different contribution of the same bands. In this regards a tentative deconvolution of the spectral profile was performed, trying to keep fixed the position and the number of bands for all the spectra. In some cases an additional band was introduced at 1230 cm^{-1} (arrows in Fig. 6).

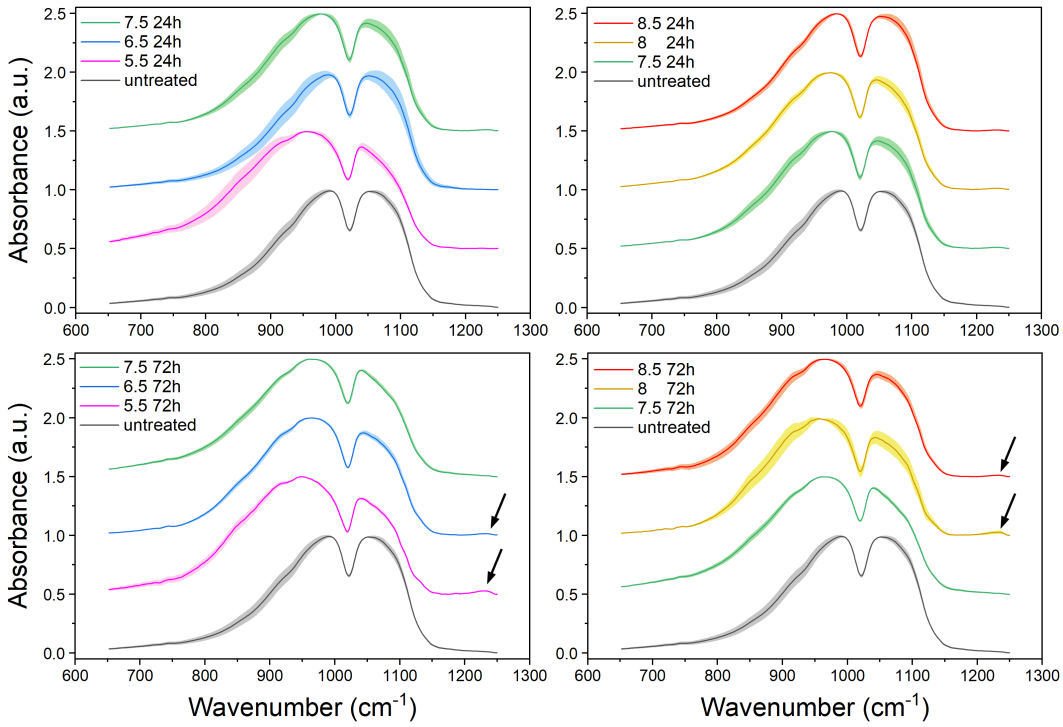

Figure 6: Normalized average FTIR spectra of Si_3N_4 powders - region 2 (from 650 cm^{-1} to 1250 cm^{-1}). Y offset among different spectra for clarity. Top row: powders immersed in BHI solutions of different pH for 24h; acidic pH set on the left, basic pH set on the right. The almost neutral pH-group (7.5) is shown on both sides. Bottom row: powders immersed in BHI solutions of different pH for 72h; acidic and basic pH sets as above. Shaded areas represent the standard deviation (SD). Arrows indicate the presence of a new small spectral feature.

Mixed Gaussian-Lorentzian functions were used for the peak fitting procedure, which was carried out using the software LabSpec. An example of fitted spectrum is provided in Figure 7, for this specific

spectrum the peak positions are the following: band 1 - 748 cm^{-1}, band 2 - 854 cm^{-1}, band 3 - 910 cm^{-1}, band 4 - 958 cm^{-1}, band 5 - 1000 cm^{-1}, band 6 - 1035 cm^{-1}, band 7 - 1052 cm^{-1}, band 8 - 1086 cm^{-1}, band 9 - 1132 cm^{-1}, band 10 - 1227 cm^{-1}. These positions were maintained fixed throughout the procedure and only slightly adapted (by a couple of cm^{-1}) when the introduction of a minor shift would result in a major improvement of the fit.

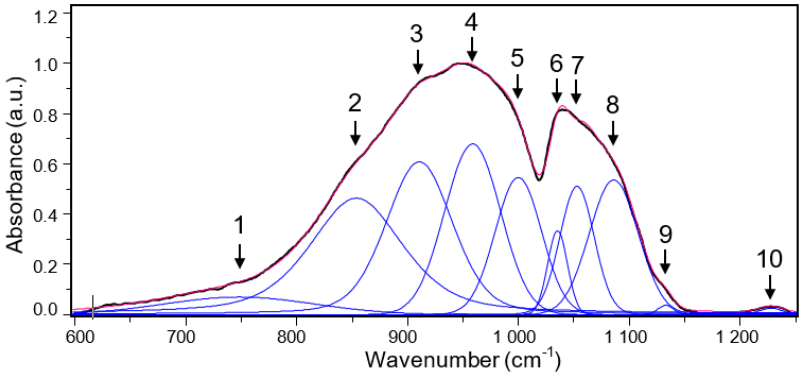

Figure 7: Example of FTIR fitted spectrum of Si_3N_4 powder - range 2 (from 600 cm^{-1} to 1250 cm^{-1}). The black line is the experimental data, the blue are the fitted peaks and the red is the cumulative fitting curve. Arrows indicate the central position of each peak.

The logical continuation of the study would have been the assignment of each band to a certain type of bond vibration, however in this case it turned out to be anything but straightforward because of the overlap between Si-N and Si-O IR modes. The issue is exemplified in Tables II-III, where some literature values are listed for each bond. To overcome this problem an additional experiment was performed (Section 3.2.1.3).

Table II: Literature for Si–N related IR bands

Mode	wavenumber (cm^{-1})	ref.
A_u	910; 917;	[6, 7]
(β-Si_3N_4)	848 (TO); 1056 (LO)	[8]
E_{1u}	985; 952;	[6, 7]
(β-Si_3N_4)	886 (TO); 1026 (LO)	[8]
E_{1u}	1040; 1041;	[6, 7]
(β-Si_3N_4)	1021 (TO); 1150 (LO)	[8]
Si–N	826 (TO); 1125 (LO);	[9]
	830 (TO); 970 - 1150 (LO);	[10]
	825 (TO); 1050 - 1125 (LO)	[11]
Si–N–Si	800 - 1100	[12]

TO: transverse optical phonon; LO: longitudinal optical phonon

Table III: Literature for Si–O related IR bands

Mode	wavenumber (cm^{-1})	ref.
Si–O–Si (δ)	790; 814	[13, 14]
TO_2	810	[15]
LO_2	820	[15]
TO_3	1020 - 1090	[15]
LO_3	1215 - 1260	[15]
TO_4	1200	[15]
LO_4	1160	[15]
Si–O	1076 (TO); 1256 (LO);	[9]
	1075 (IP), 1130-1150 (OOP)	[14]
O–Si–O	1190	[12]

IP: in-phase stretching; OOP: out-of-phase stretching

3.2.1.2 Band ratios: intensities and areas

The varying contribution of the fitted peaks to the overall spectrum was analyzed in terms of intensity and area. Statistical tests were not performed due to the low number of replicates (3 spectra per group).

In the evaluation of intensity variations, the main changes were noticed for band n. 2, 4, 5, 8 and 9. For these bands, intensity ratios were calculated pairwise and the ratios displaying more relevant trends are reported in Figure 8. It can be appreciated that in all cases the ratios in the 72h dataset have values higher than the 24h ones, in particular the values at pH 5.5 (72h) are always markedly different from the other groups, suggesting that this treatment induced more significant changes in the powder structure. Comparing groups from pH 6.5 to 8.5 and taking into account the scarcity of data and the in-group spread, no great differences in the mean values can be identified.

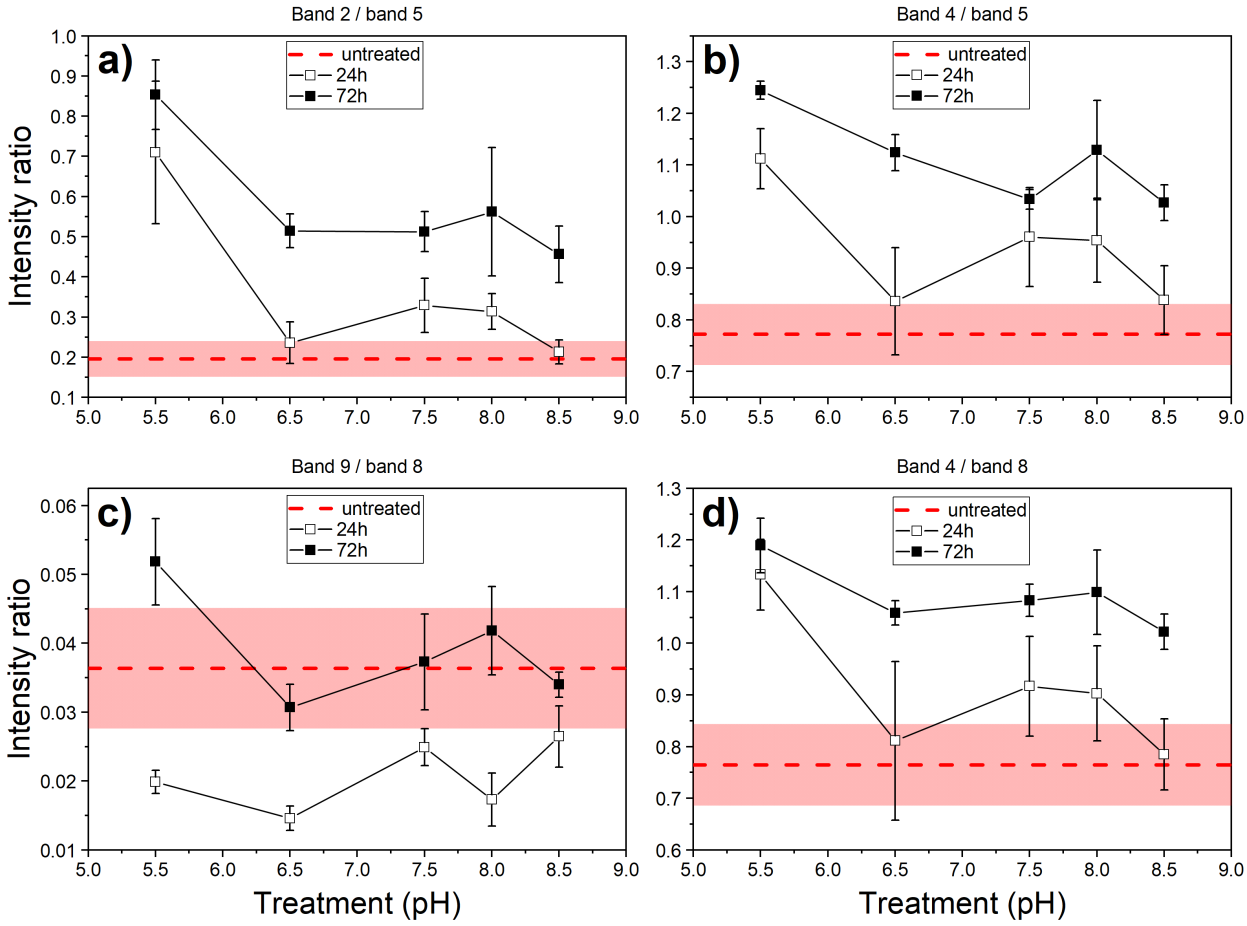

Figure 8: Intensity ratios - FTIR bands of Si_3N_4 powders. For each sample the data is reported as mean $\pm$ SD, black symbols are used for the 72h-treatment dataset whereas white symbols for the 24h dataset. The mean values for the untreated sample are reported as dashed red lines with shaded areas representing the standard deviation.

For three ratios - panels **a)**, **b)**, **d)** - the values calculated for the treated powders stand above the "threshold" value delimited by the mean values obtained for the untreated sample. This means that, in the tested pH range, the immersion of the powders in BHI for 24-72h consistently drives the increase of some bands at expense of some others. Namely: the intensity of band 2 increases w.r.t. band 5 and the intensity of band 4 increases w.r.t. both band 5 and band 8. Such changes suggest that the treatments can alter the bonding structure, but the understanding of the underlying phenomenon is dependent on the labeling of the bands, which however was not accomplished in this study. As regarding the results

in panel **c)**, at both time points the values are close to the untreated sample value, even though in this case the 24h-data stand below the dashed line. As a note: band 9 is rather small with respect to band 8 (two orders of magnitude less intense), therefore their ratio may not be very reliable.

An alternative analysis was carried out (for bands from 2 to 8) by taking the ratio between the area of each band and the total integral of the spectrum in that region. Band 1, 9 and 10 were excluded from the calculations because considered not significant for this type of analysis: band 1 basically fills the left tail of the spectrum and has a flat and broad shape, almost constant for all the spectra; bands 9 and 10 are considerably small with respect to all the other bands; furthermore band 10 is only present in some of the spectra. The most interesting results are shown in Figure 9, where the values obtained for the untreated sample can be distinguished from all the others by the red color of the spots.

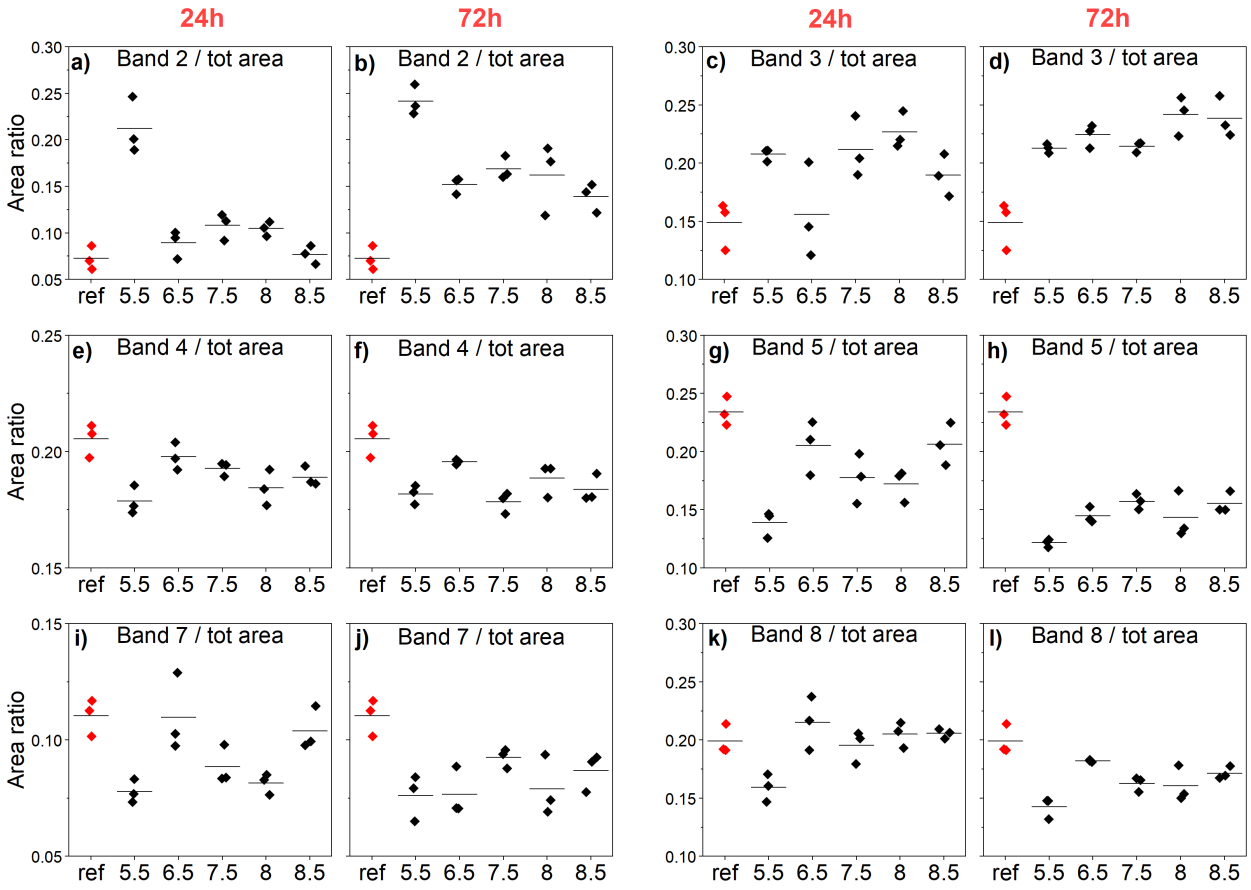

Figure 9: Area ratios - FTIR bands of Si_3N_4 powders. Treatments (pH) are indicated on the x-axis, the treatment duration is reported on top of each column of plots; the "ref" sample corresponds to the untreated powder, whose data are highlighted with red symbols instead of black ones. For each sample the horizontal line represents the mean value. "tot area" is the sum of the area of bands 2-8. The ratio band 6 / tot area is not reported because of excessive variability in each group.

As it can be observed, the situation is similar for all the bands, with trends that start to delineate in the 24h dataset and are then confirmed or accentuated in the 72h dataset, usually accompanied by a decrease in in-group variability. Bands 2 and 3 - panels **a)** to **d)** - are the only ones whose ratio over the total area is clearly higher for the treated samples compared to the untreated one. Accordingly, some effects of the treatments could be deduced from the increased contribution of these two bands to

the overall spectrum. The increase is especially high for band 2 in the pH 5.5 group. Again referring to the untreated sample, the area contribution of the other bands - panels **e)** to **l)** - is lower in the treated samples, without significant differences among the five treatment groups. Nevertheless, it is worth noting that for bands 5 and 8 the pH group 5.5 is distinguished from the others, scoring the lowest ratios.

3.2.1.3 Bulk vs powder Si_3N_4

Additional measurements were performed in order to obtain a rough idea of the effect of oxidation on the FTIR spectrum of Si_3N_4 and to elucidate which bands may arise from the vibration of Si-O bonds. Two bulk Si_3N_4 samples were analyzed: of two polished disks, one was left untreated and the other one was heated in a furnace at 200°C for 5 hours. FTIR spectra were collected using the same parameters that were previously used for the powder samples. In Figure 10**a** the spectra of polished and baked Si_3N_4 are compared, their difference (baked - polished) is also shown to highlight the contributions due to thermal oxidation. The oxidized sample displays a much broader feature from 600 cm^{-1} to 850 cm^{-1}, a more intense band at 1008 cm^{-1} and an additional band centered at 1235 cm^{-1}.

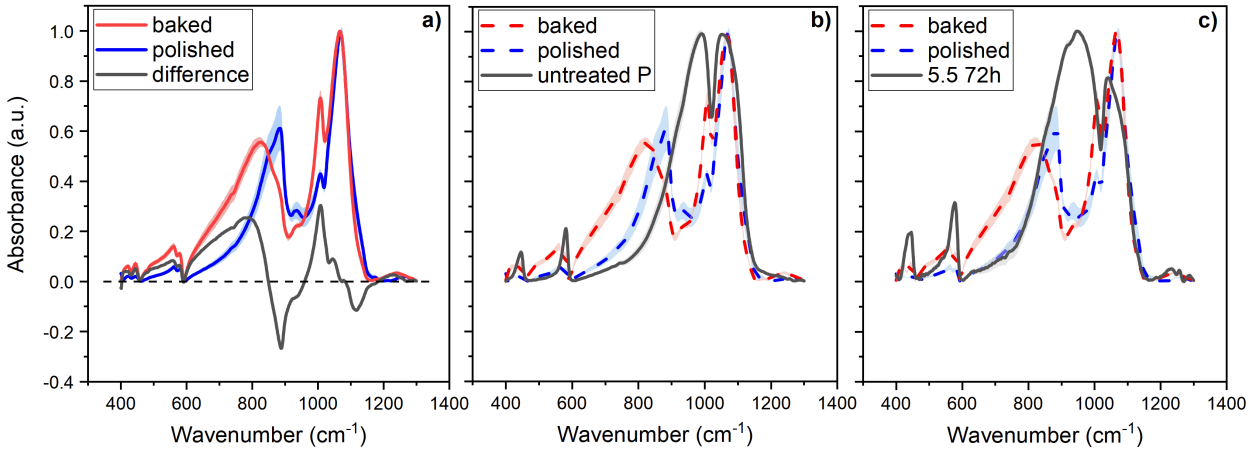

Figure 10: Normalized average FTIR spectra of Si_3N_4 (bulk and powders) - from 400 cm^{-1} to 1300 cm^{-1}. Shaded areas represent the standard deviation. **a)** Comparison of two bulk samples. The "difference" line stands for baked minus polished spectrum. Dashed line: Y = 0. **b)**,**c)** Spectra of the bulk samples are now plotted with dashed lines; full line for powder samples. "untreated P" is the untreated powder while "5.5 72h" is the powder immersed in BHI at pH 5.5 for 72h.

These spectra were then compared with the spectrum of the untreated powder and the powder treated at pH 5.5 for 72h - Figure 10 **b)-c)**. The latter sample was chosen for the comparison since it revealed more peculiar features in the previous analyses. Unexpectedly there was a striking difference between the spectral line shape of the bulk samples and the powder samples, so that the interpretation was still not free of ambiguities. In particular, the intense and broad signal between 900 cm^{-1} and 1000 cm^{-1} in the powder spectra did not find a matching feature in the bulk ones. Conversely the broad band from 600 to 850 cm^{-1} of the thermally oxidized sample was not found in the pH-treated powder. Yet, comparing the two powder samples, there is an appreciable intensity increase in this spectral area for the treated powder. The region corresponds to bands 1 and 2 (Fig. 7), suggesting that these two bands may be linked to oxidation phenomena and assigned to Si–O vibrations (bending modes [13, 14]). Absent in the spectra of the polished bulk sample and untreated powder, whereas present for treated powders and baked bulk sample, band 10 ($\sim$ 1230 cm^{-1}) is likely to be another oxidation-related

band and could be assigned to Si–O–Si asymmetric stretching [16, 17]. Finally, it is not clear why band 5 (1000 cm^{-1}) shows a clear intensity increase with the thermal treatment (bulk sample) but it has a decrease in intensity and area contribution with the pH treatments (powder samples, Section 3.2.1.2).

3.2.1.4 Summary

The effect of different pH treatments on Si_3N_4 powders was here investigated by analysing changes in the FTIR spectrum of the samples, in particular the region from 600 to 1250 cm^{-1} was addressed. Comparing the treated powders with the untreated samples, no clear trend could be extracted from the data and few relevant differences were found, mainly in the 72h treatment dataset:

- **visual comparison**: apparent band shift to lower wavenumber; intensity increase in the tail region (750-900 cm^{-1}); appearance of a small band at 1230 cm^{-1} after 72h at pH 5.5, 6.5, 8, 8.5;
- **intensity ratios**: increased contribution of band 2 with respect to band 5 and of band 4 over band 5 and 8, major effects for pH group 5.5 at both time points;
- **area ratios**: the pH treatments resulted in a higher contribution of bands 2 and 3 and a decrease in area for the other investigated bands, especially band 5 and 8 for pH group 5.5;
- **comparison with bulk samples**: the striking difference between bulk and powder Si_3N_4 spectra prevented a direct comparison of the bands; minor features shared by the pH-treated powders and the thermally-treated bulk sample suggested that bands 1, 2 and 10 may be involved in oxidation phenomena and assigned to Si–O vibrations.

3.2.2 Raman spectroscopy

3.2.2.1 Average spectra and peak fitting

The Raman spectrum of Si_3N_4 powders was divided in three regions: range 1a from 165 to 250 cm^{-1}, 1b from 250 to 675 cm^{-1} and range 2 from 675 to 1100 cm^{-1}. After baseline subtraction all the spectra were normalized from 0 to 1; the average spectrum of the untreated powder is displayed in Figure 11 **a**.

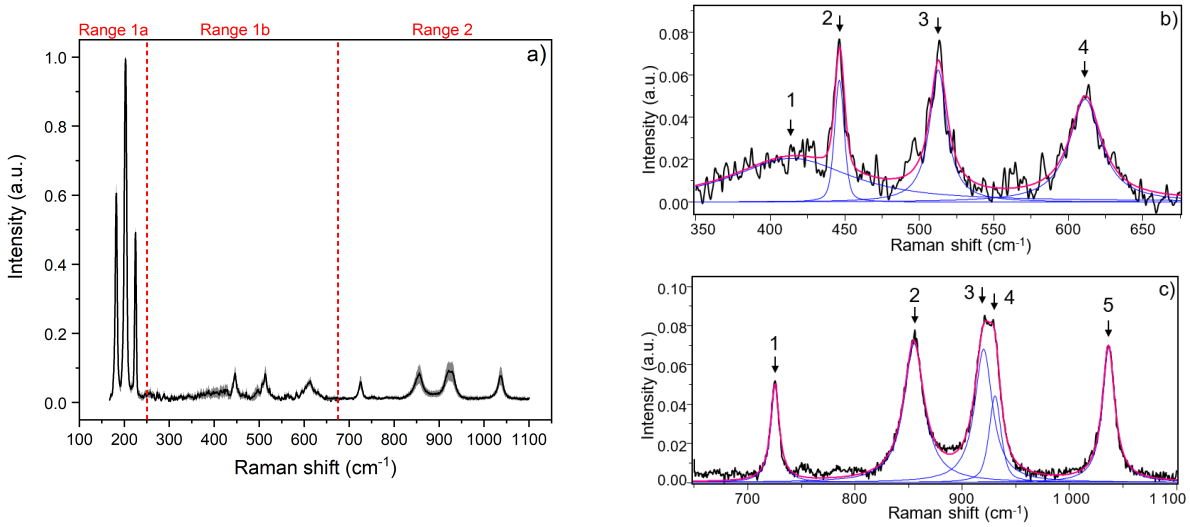

Figure 11: Normalized average Raman spectrum of Si_3N_4 powder and peak fitting. **a)** Average spectrum of untreated powder with range definition. Shaded area represents the SD. **b)** Example of fitting in region 1b. Bands centered at: 413, 446, 512 and 612 cm^{-1}. **c)** Fitting in region 2, bands centered at: 725, 854, 920, 930 and 1037 cm^{-1}.

In order to compare band shifts and variations in intensity or broadening, a fitting procedure was carried out in the three ranges. Examples of fitted spectra are reported in Figure 11 **b)-c)** for region 1b and 2. Region 1a is analysed in detail in Section 3.2.2.3. The main peaks were compared to the literature (experimental [6, 18] and theoretical [8] Raman modes of β-Si_3N_4) and identified as follows:

	Region 1a			**Region 1b**		**Region 2**				
Band n.	1	2	3	2	4	1	2	3	4	5
cm $^{-1}$	182	203	225	446	612	725	854	920	930	1037
Mode	E_{2g}	A_g	E_{1g}	E_{2g}	E_{2g}	A_g	E_{1g}	E_{2g}	A_g	E_{2g}

Additional features were found in region 1b: band 1 at 413 cm^{-1}, which can be related to amorphous Si_3N_4 vibrations [6] and band 3 at 513 cm^{-1} which is likely to arise from the vibration of Si–Si bonds from silicon nanoclusters [19].

The average spectra were visually compared to spot major differences. The results are presented in Figures 12-13, where the acidic pH data set is on the left column and the alkaline pH data set on the right one; the top row contains graphs from the powders treated for 24h while the bottom row contains the 72h treatment groups. Arrows indicate intensity increases and peak shifts.

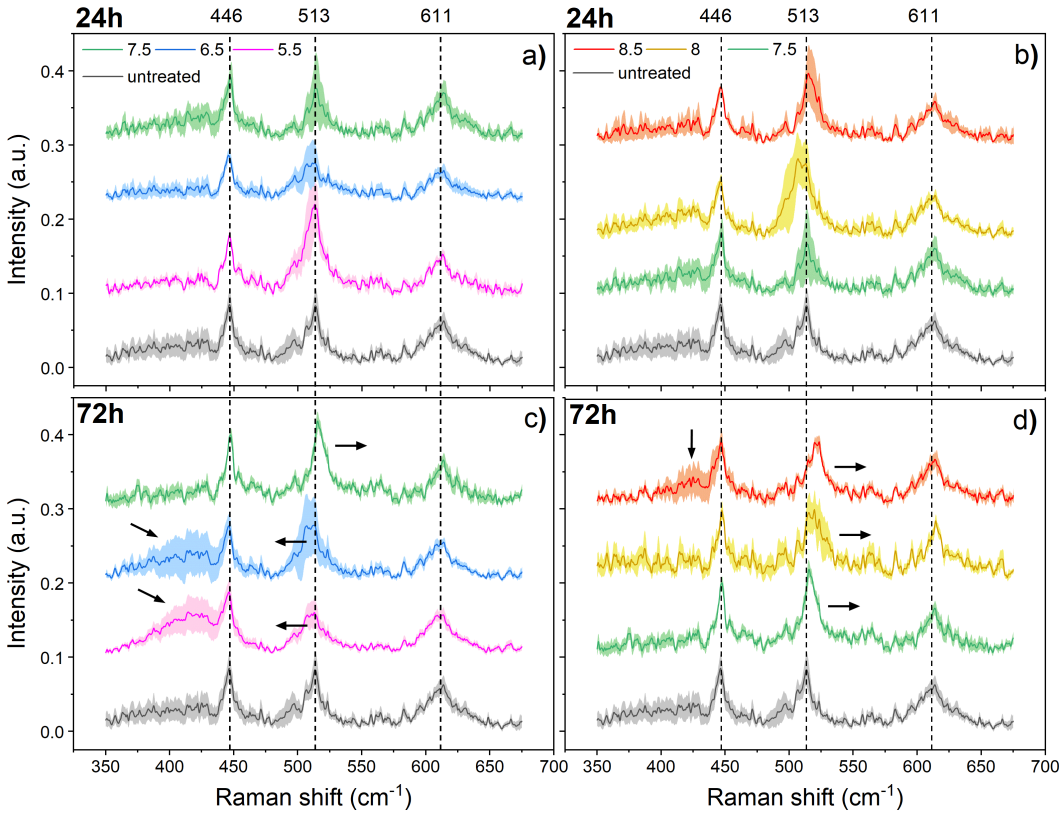

Figure 12: Normalized average Raman spectra of Si_3N_4 powders - region 1b (from 350 cm^{-1} to 675 cm^{-1}). Values in the color legend stand for the pH. Y offset among different spectra for clarity. Top row: powders immersed in BHI solutions for 24h; a) acidic pH set, b) basic pH set. The almost neutral pH-group (7.5) is shown on both sides. Bottom row: powders immersed in BHI solutions for 72h; c) acidic and d) basic pH set, respectively. Shaded areas represent the standard deviation (SD). Dashed lines correspond to the average peak position for the untreated powder, wavenumbers are reported at the top. Arrows indicate identified variations.

In both spectral regions the 72h scenario presents more evident variations when comparing the treated powders with the untreated sample, whose spectrum was considered the reference one.

Considering region 1b, it can be observed that in the acidic set (72h) there is an intensity increase in the region from 400 to 435 cm^{-1}, giving rise to a broad band which is almost absent in the spectrum of the untreated powder and the one treated at pH 7.5. To a lower degree the broadening is also present for pH group 8.5 (72h). This broad band, probably related to the presence of amorphous Si_3N_4 [6], was investigated quantitatively in terms of intensity variation versus pH but the noisy signal of this region resulted in a poorly reliable fitting and no trend was found due to high in-group variability. Still in the 72h dataset, looking at the band around 513 cm^{-1} there is a shift towards lower wavenumbers for pH groups 5.5 and 6.5 whereas for pH groups 7.5, 8 and 8.5 the shift is towards higher wavenumbers (arrows in Fig. 12). The same trend was identified in region 2 (72h data set), mainly for the bands centered at 725 and 1037 cm^{-1} (Fig. 13).

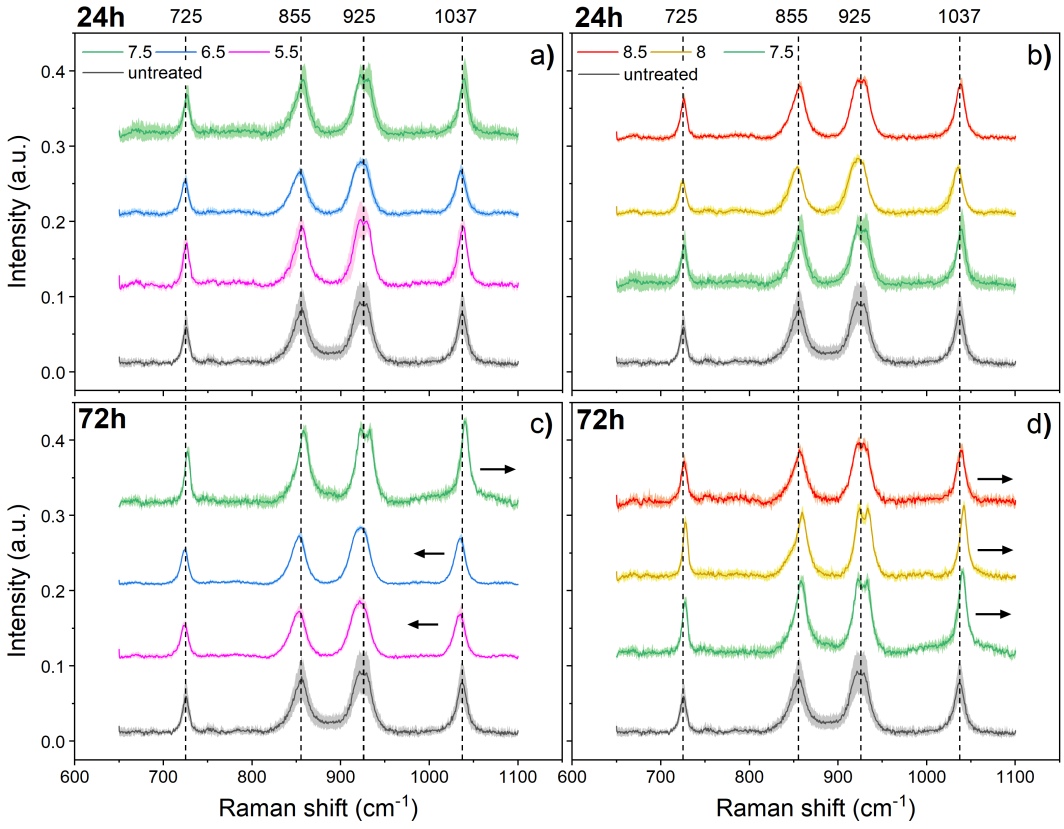

Figure 13: Normalized average Raman spectra of Si_3N_4 powders - region 2 (from 675 cm^{-1} to 1100 cm^{-1}). Values in the color legend stand for the pH. Y offset among different spectra for clarity. Top row: powders immersed in BHI solutions for 24h; a) acidic pH set, b) basic pH set. The almost neutral pH-group (7.5) is shown on both sides. Bottom row: powders immersed in BHI solutions for 72h; c) acidic and d) basic pH set, respectively. Shaded areas represent the standard deviation (SD). Dashed lines correspond to the average peak position for the untreated powder, wavenumbers are reported at the top. Arrows indicate identified variations.

3.2.2.2 Band shifts - region 1b and 2

In the attempt to rationalize the observed trends the apparent shifts were monitored by taking - for each individual spectrum - the peak position values from the outcome of the fitting procedure. Specifically, the selected bands were band 1 and 5 in region 2 and band 3 in region 1b. Average position value and standard deviation were calculated for each sample and plotted as a function of the treatment pH. The results are shown in Figure 14, here the untreated sample was considered as a reference value and reported in the form of dashed horizontal line with a shaded area representing the error.

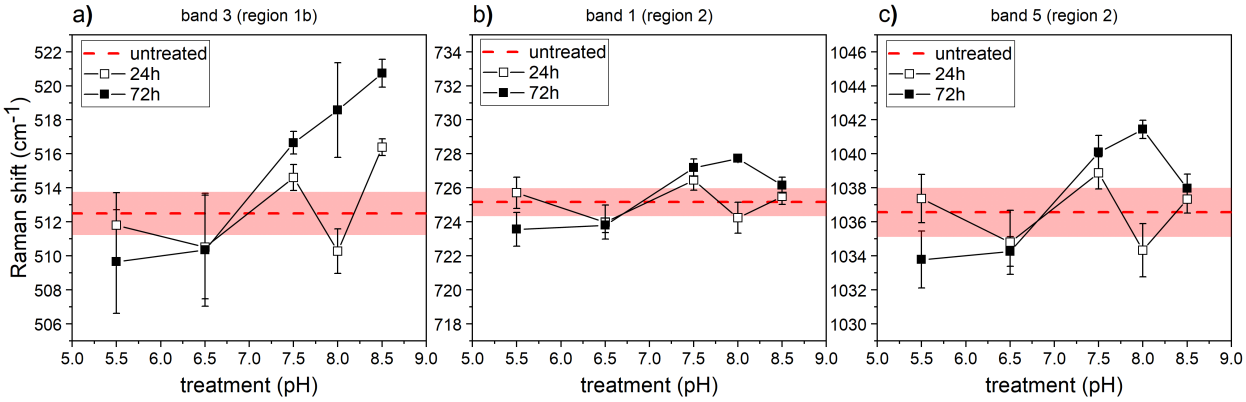

Figure 14: Si_3N_4 Raman band shifts - region 1b and 2. Shifts are reported as a function of the treatment pH. Symbols with error bars represent the average value of each sample $\pm$ standard deviation. The average value of the untreated powder is displayed as a reference horizontal line (red, dashed), in this case the shaded area is SD.

After 24h of treatment the effects were mostly within the error range of the untreated powder and no clear trend was identified. Conversely, with the 72h immersion there was a quite defined separation between the effects of acidic and alkaline treatments: the former caused band shifts towards lower wavenumbers (w.r.t. the untreated powder spectrum) while the latter caused no significant shifts (pH group 8.5 in region 2) or shifts towards higher wavenumbers (pH groups 7.5 and 8 in region 2; 7.5, 8 and 8.5 in region 1b). Considering band 3 in region 1b (centered at $\pm$ 513 cm^{-1} for the untreated powder), which was assigned to the presence of elemental silicon, it can be assumed that the peak shifts correspond to a variation in the size of silicon nanoclusters; in fact other studies reported that this band has a shift to higher wavenumbers when the size of Si-clusters in Si_3N_4 increases [19, 20]. In this case this would mean that the cluster size increases with the alkaline treatments while decreases with the exposure of the powders to acidic pH conditions.

3.2.2.3 Analysis of Si_3N_4 triplet

The portion of the β-Si_3N_4 Raman spectrum that goes from 165 cm^{-1} to 250 cm^{-1} was termed "region 1a" and consists of three bands corresponding to Si–N vibration modes: E_{2g}, A_g, E_{1g} [6, 8], "band 1", "band 2" and "band 3" henceforth. All the spectra were normalized from 0 to 1 with respect to the intensity of the central peak. A visual inspection of the average spectra of the different samples is reported in Figure 15. Minor differences emerged in terms of peak position: after 24h of pH treatment a slight shift to lower wavenumbers can be seen for the sample treated at pH 6.5, while after 72h for the samples treated at pH 7.5 and 8 the three bands appear shifted to higher wavenumber. No evident differences can be appreciated as regarding band width and relative intensities.

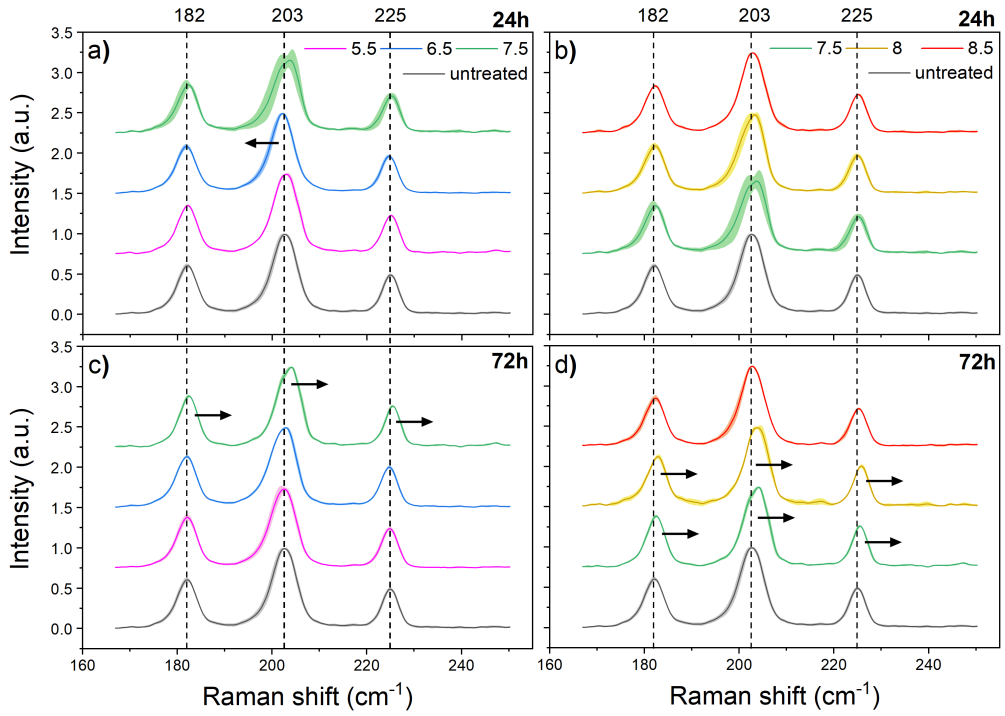

Figure 15: Normalized average Raman spectra of Si_3N_4 powder - region 1a (from 165 cm^{-1} to 250 cm^{-1}). Y offset among different spectra for clarity. Top row: powders immersed in BHI solutions of different pH for 24h; acidic pH set on the left, basic pH set on the right. Bottom row: powders immersed in BHI solutions of different pH for 72h; acidic and basic pH sets as above. Shaded areas represent the standard deviation (SD). Dashed lines correspond to the average peak position for the untreated powder. Arrows indicate band shifts.

To obtain a more accurate comparison, the spectra were fitted with three bands and, for each band, the following characteristics were monitored as a function of pH: position, width, intensity.

The obtained trends of the band shift are reported in Figure 16, where data is displayed as avg $\pm$ SD in the form of horizontal lines for the untreated sample and symbols with error bars for the other samples. As noticed in the visual inspection, the clearest deviations from the peak positions of the untreated sample arise for pH 6.5 - 24h and pH 7.5 and 8 - 72h.

For each band, normality of the data in each group was checked by Shapiro-Wilk test [21] and met by almost every group, exceptions were assumed to be still acceptable for the test. Homoschedasticity was checked with Levene's test [21]; the assumption was mainly satisfied in the 72h dataset while violated in the 24h one. These issues were considered as not-compromising for the performance of one-way ANOVA tests [21]. All the tests were performed with OriginPro. At 24h, significant difference among population means was obtained for band 2 and band 3, with p-values of 0.015 and 0.042 respectively. In both cases mean comparison with Tukey test [21] pointed out that the main difference lay between the treatment group pH 6.5 and the groups 7.5 and 8.5. In the 72h set, ANOVA was significant for all the three bands (band1 p=1.6·10^{-12}, band2 p=3.6·10^{-13}, band3 p=1.1·10^{-13}). Tukey tests confirmed that pH groups 7.5 and 8 were significantly different from all the others.

The same analysis was applied to the study of band width variations. For each band the average full-width at half maximum (FWHM) is plotted versus pH in Figure 17. Very high in-group variability

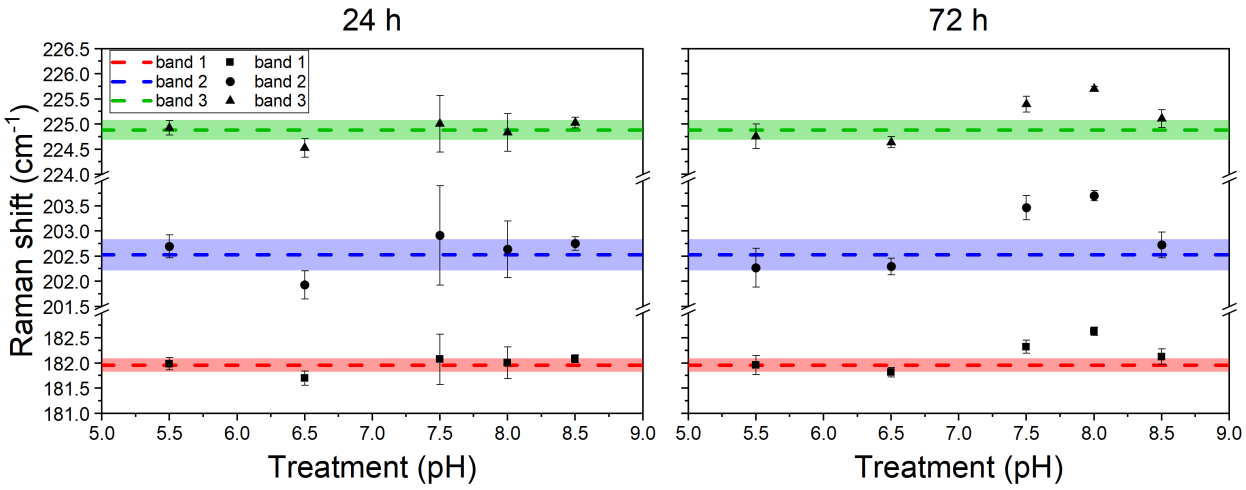

Figure 16: Band shift in Si_3N_4 Raman triplet. Dashed lines represent the average peak position for the untreated sample. Shaded areas represent the correspondent standard deviation. Data for the treated samples is also reported as mean peak position ± standard deviation (symbol with error bar). Left: results after 24h of treatment. Right: after 72h of treatment.

was found in the 24h set and statistical tests revealed no significant differences between the population means. In the 72h set the trends were slightly more pronounced and the results of one-way ANOVA suggested that there was significant difference among the groups (band1 p=1.6·10^{-7}, band2 p=0.03, band3 p=1.2·10^{-6}). The trend is similar for all the three bands: pH groups 5.5, 6.5 and 8.5 have band width values not far from the untreated group values, whereas groups 7.5 and 8 display significantly lower values compared to all the other groups.

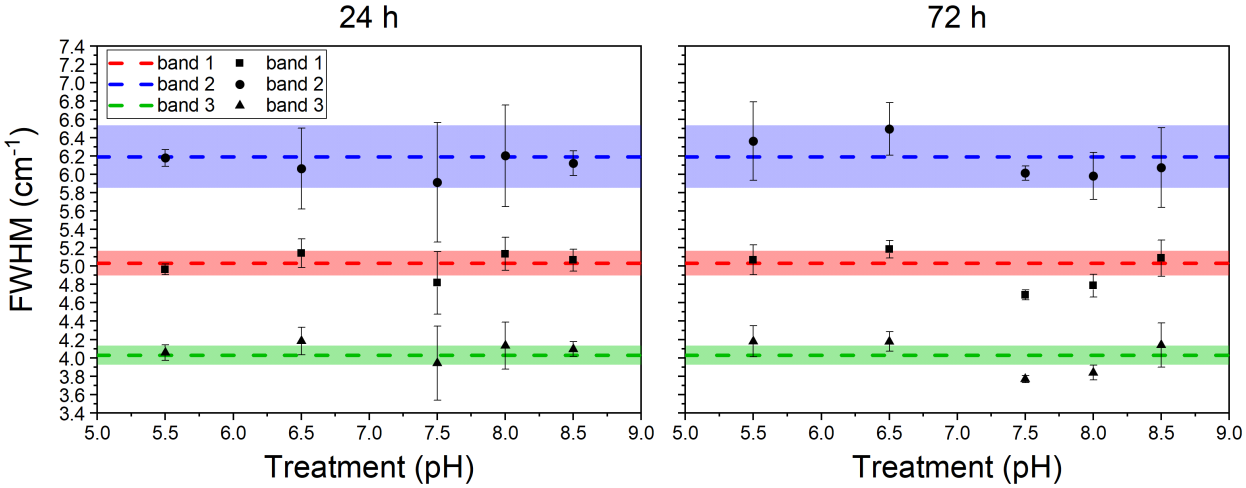

Figure 17: Band width in Si_3N_4 Raman triplet. Dashed lines represent the average peak position for the untreated sample. Shaded areas represent the correspondent standard deviation. Data for the treated samples is also reported as mean peak position ± standard deviation (symbol with error bar). Left: results after 24h of treatment. Right: after 72h of treatment.

Concerning the band intensity, the intensity of the central peak (band 2) was always set to 1 a.u. during the normalization procedure. Therefore, only the relative intensity of the other two peaks (band 1 and band 3) was considered for comparison of the different treatments. The intensity ratio of band

1 over band 3 was calculated and is reported in Figure 18 for the various treatment groups. Here box-and-whiskers plots were used to highlight in-group variability and outliers. Statistically significant differences were found only in the 72h dataset (normality and homoschedasticity assumptions were satisfied; ANOVA test, p=0.0074) and the highest difference was found between two pairs of treatment groups: pH 5.5 and 6.5 on the higher values side, pH 7.5 and 8 on the lower side. However, none of the groups was significantly different from the untreated one.

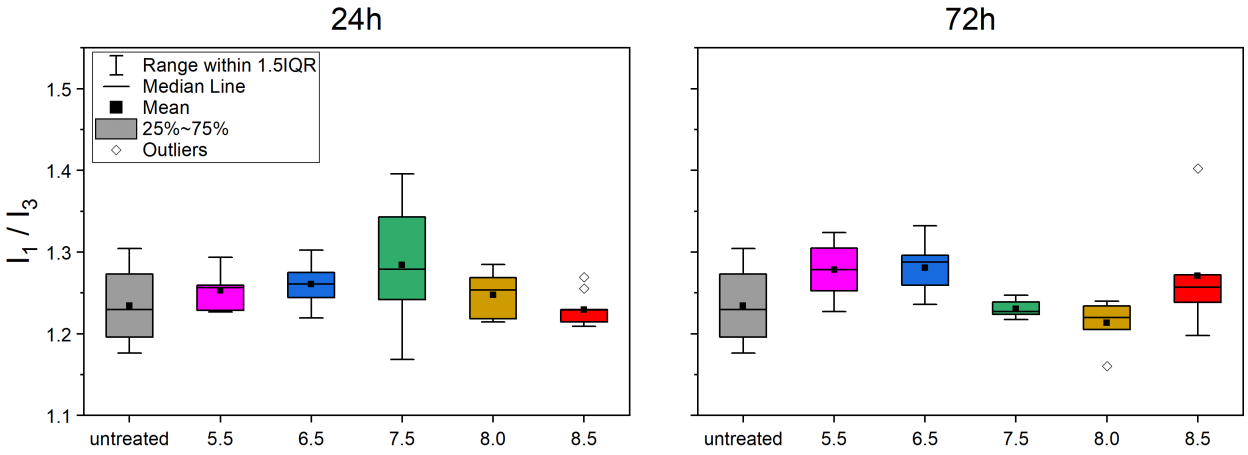

Figure 18: Intensity ratio of bands 1 and 3 of Si_3N_4 Raman triplet. Treatment groups are reported on the x-axis. IQR= interquartile range.

3.2.2.4 Summary

The effect of pH treatments on Si_3N_4 powders was here investigated by analysing changes in the Raman spectrum of the samples, which was divided into three regions. Although few significant differences were found, some trends could be highlighted from the data, mainly in the 72h treatment dataset.

Region 1a

- **band shifts**: 24h treatment - pH 6.5, shift to lower wavenumbers; 72h - pH 7.5 and 8, shift to higher wavenumbers (compared to the untreated sample);
- **band width**: 72h - pH 7.5 and 8, lower FWHM values compared to all the other groups;
- **intensity ratio band1/band3 ($\mathbf{182\,cm^{-1}}$ / $\mathbf{225\,cm^{-1}}$)**: 72h - pH 7.5 and 8, lower values compared to pH 5.5 and 6.5.

Region 1b

- **band shifts**: 72h - band 3 ($513\,cm^{-1}$) shifted towards lower wavenumbers with acidic treatments whereas towards higher wavenumbers for pH groups 7.5, 8 and 8.5, this could represent a decrease (and an increase) in the size of silicon nanoclusters with exposure to acidic (and alkaline) conditions;
- **intensity variations and broadenings**: 72h - apparent intensity increase and broadening of the band assigned to amorphous Si_3N_4 (400 to $435\,cm^{-1}$) for treatments at pH 5.5, 6.5 and 8.5.

Region 2

- **band shifts**: 72h - bands 1 ($725\,cm^{-1}$) and 5 ($1037\,cm^{-1}$) shifted towards lower wavenumbers with acidic treatments whereas towards higher wavenumbers for pH groups 7.5, 8.

3.2.3 X-ray photoelectron spectroscopy

The first step in the analysis of the XPS spectra of Si_3N_4 powders was the visual assessment of the narrow scans performed around Si2p, N1s and O1s. For each element the spectrum of the untreated powder was considered as a reference and used for making comparisons with the treated samples. The results for the Si2p spectra are reported in Figure 19 in the BE range 106-95 eV, where a clear separation between treated and untreated powders can be appreciated. The number of counts/s in the peak maximum was above 2000 for the untreated powder ($\sim$ 2500 counts/s) while it decreased to around 1600 counts/s with the 24h treatments and had a further decrease for the powders treated for 72h, to $\sim$ 1300 counts/s for pH groups 7.5 and 8.5 and to $\sim$ 1100 counts/s for pH groups 8, 6.5 and 5.5. In addition, for all the treatments the peak shape appeared to be more skewed compared to the untreated one. At this level of observation the results of acidic and basic pH treatments are very similar and cannot be associated to distinct effects; a minor difference can be evidenced in the 72h datasets, where looking at pH group 7.5 (green dots in figure) the spectra of the powders treated in more acidic conditions are "matching" with the left side of the green spectrum whereas the spectra of the more alkaline groups are slanted toward the right side.

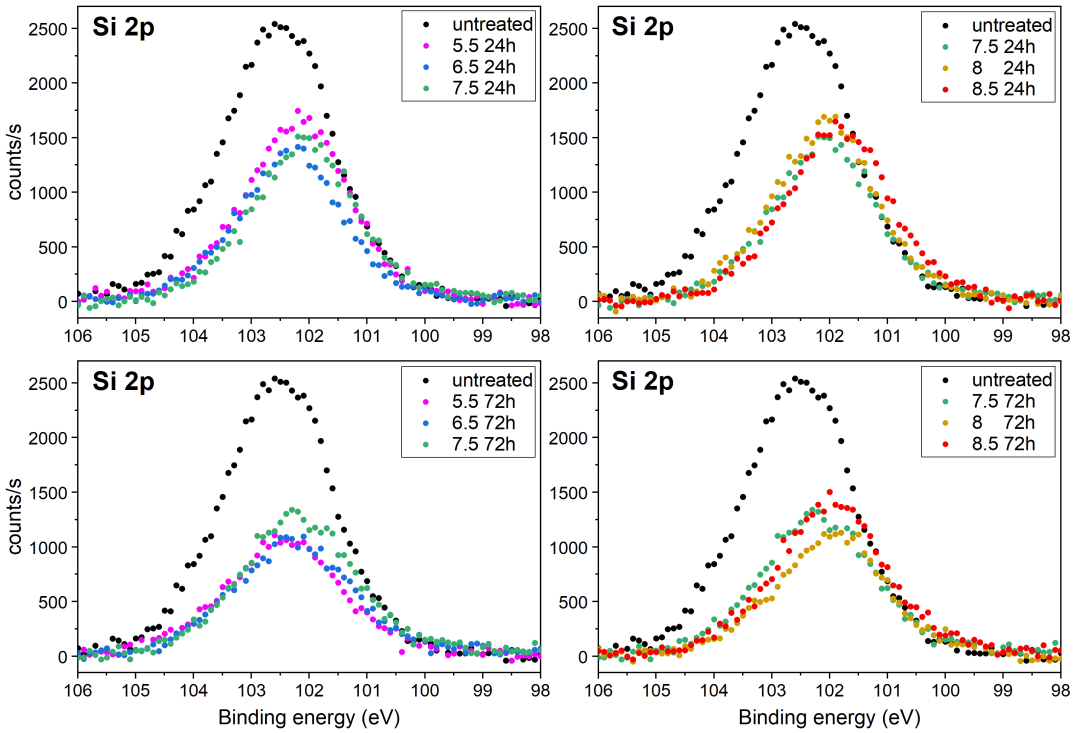

Figure 19: XPS Si2p narrow scans on Si_3N_4 powders. Top row: powders treated in BHI solutions of different pH for 24h; acidic pH set on the left, basic pH set on the right. The almost neutral pH-group (7.5) is shown on both sides. Bottom row: powders immersed in BHI solutions of different pH for 72h; acidic and basic pH sets as above.

The results for the N1s and O1s spectra are reported in Figures 20-21 in the binding energy ranges 404-392 eV and 537-528 eV, respectively.

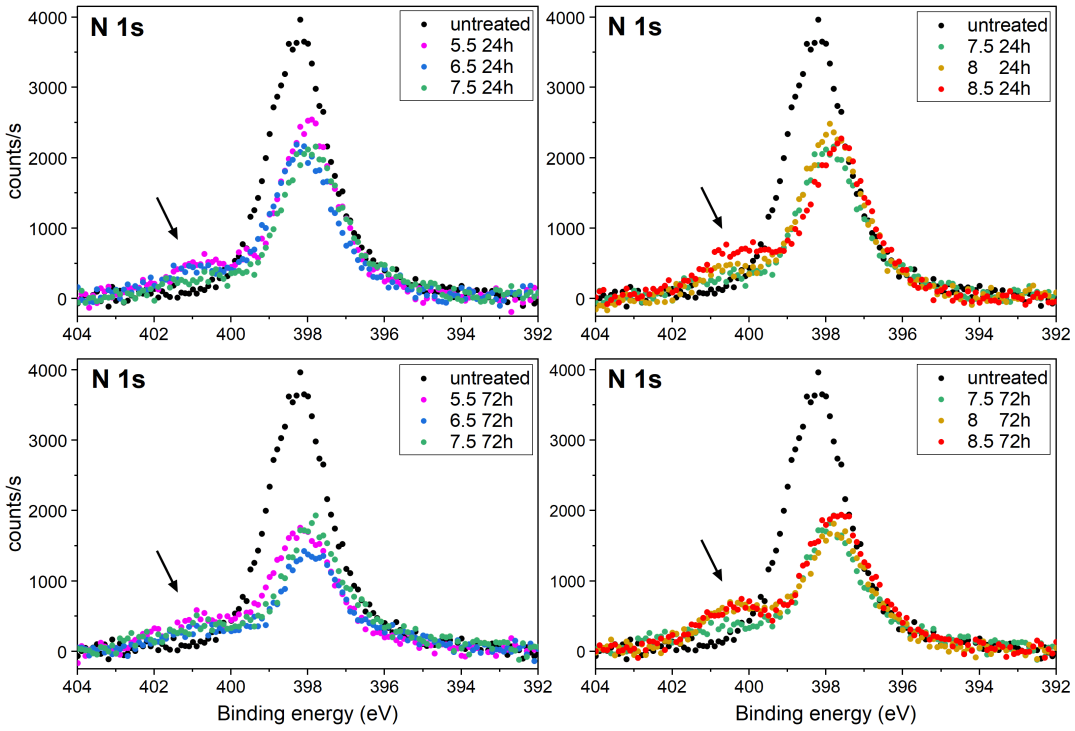

Figure 20: XPS N1s narrow scans on Si_3N_4 powders. Arrangements and colors as in Fig.19. Arrows indicate the presence of a new small spectral feature.

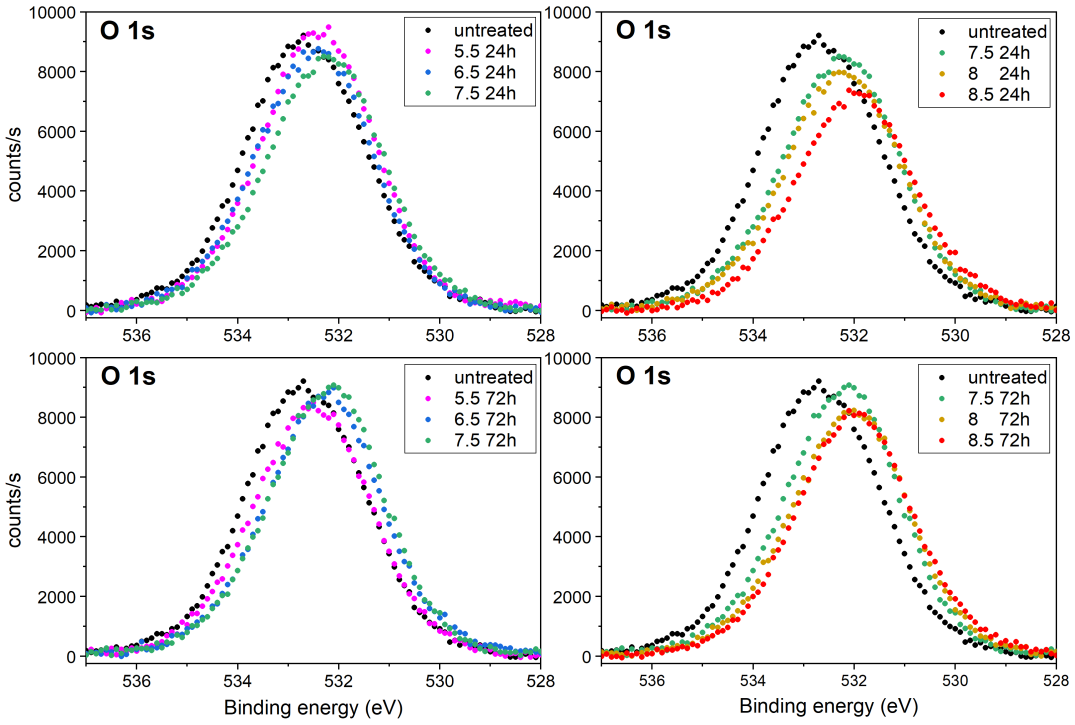

Figure 21: XPS O1s narrow scans on Si_3N_4 powders. Arrangements and colors as in Fig.19.

As for the Si2p spectra, the N1s spectra reveal a remarkable difference between untreated and treated powders, with the various pH conditions causing very similar effects. For the untreated powders the acquisition reached up to $\sim$ 4000 counts/s in the central position (around 398 eV) while it remained below 2500 counts/s for the 24h-treated powders and lastly it fell below 2000 counts/s with the longer treatments. Concurrently, a peak in the range 402-400 eV became evident with all the treatments (arrows in Fig.20) and in particular the signal was better defined for pH groups 8 and 8.5 (72h data set). Considering the O1s spectra (Fig.21) there was still a decrease in counts/s with the pH treatments compared to the untreated powder, this time the decrease was more evident with the alkaline treatments than with the acidic ones. All the treatments resulted in an apparent shift of the peak center towards lower binding energies.

In the light of these observations, a peak deconvolution procedure was carried out in the attempt to elucidate the differences in skewness in the Si2p spectra, the emergence of an additional peak in the N1s spectra and the apparent peak shift in the O1s spectra. The peak fittings and assignments were not only based on reference BE values, since XPS databases often contain values with large spread for the same chemical species [22]. The peak model relied in the first place on the underlying chemistry, using a number of components that could guarantee a decent fit and at the same time a clear interpretation of each component peak. Moreover, the model aimed at being qualitatively self-consistent when comparing the spectra of two elements involved in the same bond, e.g. a variation in a specific peak component in the Si2p spectrum related to $Si(–N)_4$ bonds should be reflected in the corresponding peak component in the N1s spectrum. Peak position, numbering and assignment are reported in Tables IV-V. The deconvolution for the Si2p untreated powder can be appreciated in Figure 22, along with a deconvoluted N1s spectrum of the untreated powder and the analogous for the powder treated at pH 8 for 24 h, in which an additional band was inserted.

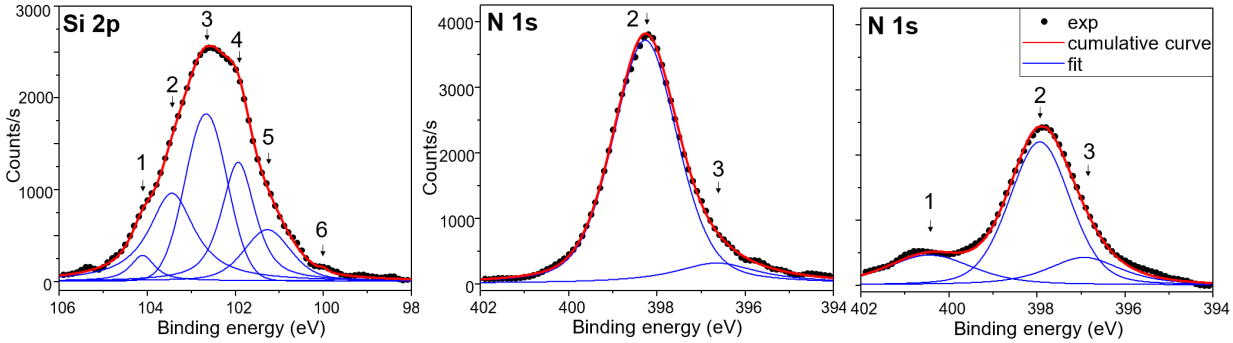

Figure 22: XPS deconvolution. Left: Si2p of untreated powder; center: N1s of untreated powder; right: N1s of powder treated at pH 8 for 24h.

Table IV: Si2p fitted peaks assignment

Band n.	Binding Energy (eV)	Bonding state	Ref.
1	104.1	$Si(–O)_4$	[23]
2	103.4	$(O–)_3Si–N$	[24]
3	102.7	$(O–)_2Si–N$	[24]
4	101.9	O–Si–N	[25]
5	101.3	$Si(–N)_4$	[25]
6	99.9	Si^0	[23]

Table V: N1s fitted peaks assignment

Band n.	Binding Energy (eV)	Bonding state	Ref.
1	400.5	$Si–N(–H)_2$	[26, 27]
2	397.9	$O–N(–Si)_2$	[24]
3	396.9	$N(–Si)_3$	[25]

The fitting of the Si2p signal was based on the idea that the surface layer of commercial silicon nitride particles is always oxidized and different degrees of oxidation are possible, each corresponding to a different degree of substitution of N atoms with O atoms in the tetrahedral crystalline units (see also Discussion 3.3). Within this framework, six bands were identified, starting from the highest degree of oxidation, $Si(–O)_4$, at higher binding energies, and progressively going towards lower BE as the oxidation decreases. As regarding the N1s spectra, for the untreated powder only two main peaks were identified: one corresponding to nitrogen involved in three bonds with silicon (as in silicon nitride) and the other, at slightly higher BE, related to an oxidized state in which one bond is with oxygen. The new band emerged around 400 eV after the pH treatments was assigned to amine groups, $Si–N(–H)_2$, which could reasonably form during the exposure of the powders to aqueous media.

A meaningful comparison of the varying contribution of bands in both Si2p and N1s spectra was obtained by taking the ratio between the area of the only band related to "pure" silicon nitride and the sum of the areas of the bands related to oxidation, that is: band 5 / (band 1 + band 2 + band 3 + band 4) in the case of Si2p; band 3 / band 2 for the N1s case. Similarly, for the N1s spectra also the area ratio of band 1 / band 2 was analyzed in order to evaluate how the contribution from amine groups varied with the treatment conditions. In every comparison the values obtained for the untreated powder were considered as a reference point. For the treated powders, both 24h and 72h treatments, the area of the component related to silicon nitride $Si(–N)_4$ evidently increased with respect to the components ascribed to the oxygen-substituted tetrahedra (Fig. 23, first two panels). The trend is more defined in the Si2p spectra, where the effect seems more pronounced with the alkaline pH treatments. Lastly, the effect of pH and time on the emergence of NH_2 surface groups was very mild, as it can be seen in the third panel, without remarkable differences among the ten treatment groups; the amine component peak reached the maximum relative area (w.r.t. band 2) in the treatment group at pH 8 for 72h.

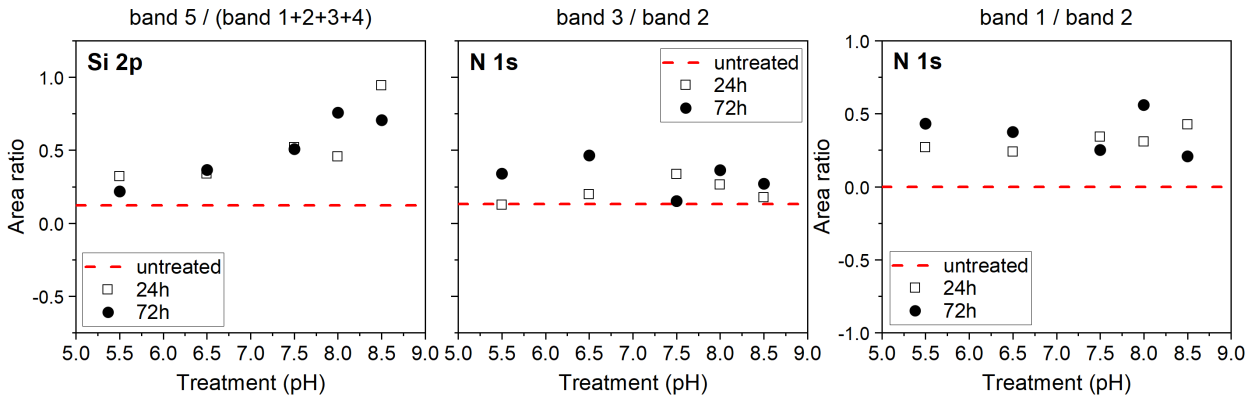

Figure 23: XPS component area ratios. From left to right: ratio between silicon nitride component peak and oxidation-related component peaks in Si2p spectra; ratio between silicon nitride component peak and oxidation-related component peak in N1s spectra; ratio between amine groups component peak and oxidation-related component peaks in N1s spectra.

3.2.4 Zeta potential measurements

Owing to the limited availability of the instrument, only some of the powders were analyzed, namely the untreated powder and the powders previously treated for 72h in BHI broth at initial pH 5.5, 7.5 and 8.5. The criteria for selecting these treatments groups were: the longest exposure time (72h), the most acidic condition (pH 5.5), the most alkaline one (pH 8.5) and the normal BHI (pH 7.5). The results

are displayed in Figure 24. At first sight it can be noticed that all the curves of the treated powders are remarkably different from the curve of the untreated powder, in fact the former ones display two points of charge inversion whereas the latter curve has no inversion point and the zeta potential remains negative throughout the whole pH range (from pH 4 to pH 11). The negative value may be attributed to a prevalence of surface silanol groups with respect to primary amine groups; in fact the Si-OH groups are dissociated into Si–O^- and H^+ for pH values higher than the isoelectric point. This trend resembles the typical behavior of silicon oxide particles, whose i.e.p. is around pH = 2 (for pure SiO_2) [28].

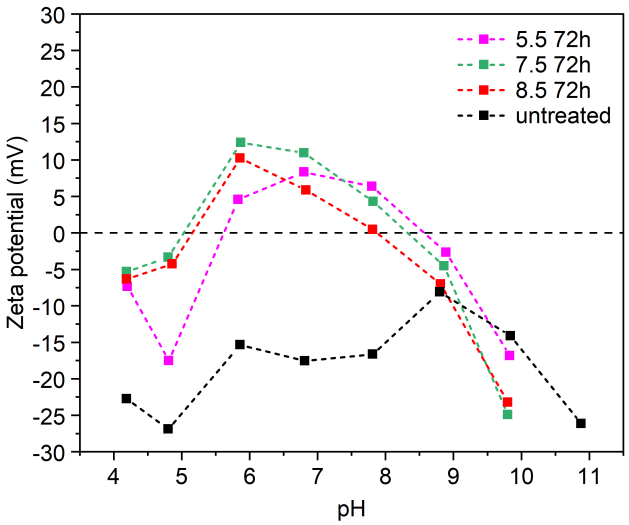

Figure 24: Zeta potential measurement as a function of pH.

Considering the treated powders, at pH $\sim$ 4 their zeta potential is less negative with respect to the untreated powder (5-7 mV compared to 22 mV below zero), suggesting the presence of a smaller fractional number of silanol sites compared to the untreated powder, to which coincides an almost neutral balance of negatively and positively charged groups (assuming no specific adsorption of ions from the aqueous NaCl solution [29]). The curves of treatment groups 7.5 and 8.5 have the same trend: negative zeta potential at about pH 4, increasing for 4 $<$ pH $<$ 6, with a sign inversion between pH 5 and pH 6, then decreasing for 7 $<$ pH $<$ 10. The second sign inversion point is at pH $\sim$ 8 for treatment group 8.5 while at a slightly higher pH value for treatment group 7.5. The remaining treatment group (pH 5.5 72h) presents a similar curve, except for the first pH range where, in this case, the zeta potential decreases from pH 4 to pH 5 and the first inversion point is shifted towards pH 6. The ascending part of the curves indicates an increase in positively charged groups and the highest zeta potential value probably corresponds to the saturation of the available sites. Higher pH values result in lower degrees of protonation, such that the positive charges around the particle surface can still neutralize the negative ones but the number of excess positive charges becomes lower and lower with the increase of pH from 7 to 10. This corresponds to the descending part of the curves, ending with negative potential values similar to the untreated powder.

It must be noted that all the measured zeta potential values fall within the range -30 mV to 30 mV, which according to the literature denotes unstable particle dispersions or suspensions, being susceptible to aggregation and flocculation due to attractive van der Waals forces [5, 30].

3.3 Discussion

Before discussing the overall results of the characterization of silicon nitride powders, it is essential to outline the general structure of a Si_3N_4 particle. To this purpose a simple yet effective model, presented by Greil et al. in 1991 [31], is here briefly recalled. First of all, commercial silicon nitride powders always contain a certain amount of oxygen due to the fact that the oxidation reaction of Si_3N_4 to silica (SiO_2) is thermodynamically favorable at room temperature (RT) both in oxygen- and water-containing atmospheres (even though the reaction kinetics is very slow at RT). The reactions, with the correspondent Gibbs free energy [32], are the following:

$$Si_3N_{4(s)} + 3\ O_{2(g)} \longrightarrow 3\ SiO_{2(s)} + 2\ N_{2(g)} \qquad \Delta G_r^\circ(298\ K) = -\ 1922\ KJ{\cdot}mol^{-1}$$

$$Si_3N_{4(s)} + 6\ H_2O_{(l)} \longrightarrow 3\ SiO_{2(s)} + 4\ NH_{3(g)} \qquad \Delta G_r^\circ(298\ K) = -\ 565\ KJ{\cdot}mol^{-1}$$

The oxygen is mainly contained in a surface layer where the oxygen concentration decreases towards the silicon nitride particle core. Such compositional gradient gives rise to different bonding states, forming two main "shells" which are schematized in Fig.25**a** : the outer shell is mainly silica-like while the inner one is silicon oxynitride-like. When exposed to aqueous media the particles are subject to hydrolysis and surface dissolution reactions which lead to the formation of a more complex siliceous surface with a "gel" layer (Fig.25**b**) in which silicon oxide and silicon nitride groups are hydrolyzed into silanols (Si-OH) and primary amines (Si-NH_2) [2, 31, 33]. These two groups undergo pH-dependent dissociation reactions which result in charged species, therefore the surface charging and potential of the particles will depend on occupancy of the surface sites by the different functional groups. The fundamental reactions are:

$$Si-OH_2^+ \rightleftharpoons Si-OH + H^+ \tag{4}$$

$$Si-OH \rightleftharpoons Si-O^- + H^+ \tag{5}$$

$$Si-NH_3^+ \rightleftharpoons Si-NH_2 + H^+ \tag{6}$$

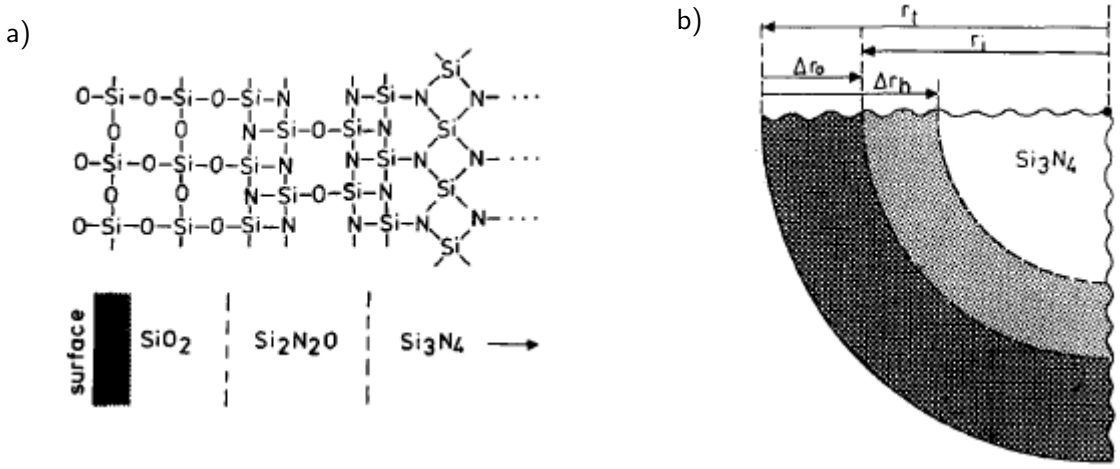

Figure 25: Surface layer model for oxygen-containing silicon nitride particle. (a) Compositional gradient and bonding structure from surface (left) towards core (right) of the particle; Si_2N_2O = silicon oxynitride. (b) Layers in aqueous environment: r_t = radius of oxide free particle, r_i = actual particle radius, $\Delta r_0 = r_t - r_i$ = oxide layer thickness, Δr_h = thickness of gel layer; where $\Delta r_0 \ll r_t$ and $\Delta r_h \ll r_t$. Schematics adapted from [31].

Oxygen can be incorporated in the tetrahedral units of the crystal up to different amounts, corresponding to different bonding scenarios which are comprehensively described by the Random Bonding Model (RBM) [34, 35]. In this representation one can expect five types of tetrahedron in accordance with the generic formula SiO_xN_{4-x} with $x = 0, 1, 2, 3, 4$, from the least to the most oxidized species.

Starting from the results of vibrational spectroscopies, the identified band shifts and broadenings provide evidence of an altered crystalline structure as a consequence of the exposure to aqueous medium for 24h and 72h. In fact the varying presence of oxygen can induce a certain amount of disorder in the β-Si_3N_4 network, with an overall weakening of Si–N bonds. The correspondent decrease in force constant correlates with a shift of vibrational frequencies towards lower wavenumbers [36], which could justify the band shifts (towards lower wavenumbers) observed in the Raman spectra of the powders exposed to acidic pH treatments. Interestingly, the powders treated in alkaline media displayed Raman shifts towards higher wavenumbers and lower FWHM when compared to the untreated powder, which could suggest a lower degree of oxidation. However, the complementary FTIR study revealed an increased contribution of the signals assigned to Si–O bonds in the spectra of the powders treated in both acidic and alkaline conditions (w.r.t. the untreated sample), even though the effect was more pronounced for the treatment at pH 5.5.

Considering the XPS results, in the Si2p and N1s spectra the peak area contribution of oxidized groups was lower in the pH-treated samples compared to the untreated powder. At the same time a decrease in counts/s was found in the O1s spectra of the treated powders, together with a shift towards lower binding energies, again suggesting a reduced presence of oxide layers [37] w.r.t. the untreated particles. From a complementary perspective, the contribution of non-oxidized Si_3N_4 peaks in Si2p and N1s spectra increased with the pH treatments, particularly when the powders were exposed to alkaline conditions for 72h. This finding is in agreement with the results of zeta-potential measurements. It is well-known that a higher degree of oxidation, thus a stronger silica-like behavior, should result in a more negative zeta-potential, with an i.e.p. at around pH = 2 (pure SiO_2) [28]; according to Greil et al. [31] the pH_{iep} of silicon nitride powders decreases linearly with an increase in surface oxygen. From the analyses of the present study it was the untreated powder to behave as the most oxidized sample, having only negative zeta potential values and no isoelectric point in the pH range 4-11, the same features were found in previous studies on thermally oxidized Si_3N_4 [3, 38]. Conversely, the other samples investigated in this study, meaning the pH-treated powders, displayed a transition towards positive potentials values approximately for $6 < pH < 8$.

An important factor to consider is that, during the immersion of the powders in BHI for 24-72h, the silicon nitride particles also undergo a hydrolysis reaction which produces silica and ammonia ($Si_3N_4 + 6\ H_2O \longleftrightarrow 3\ SiO_2 + 4\ NH_3$) and is particularly favoured at high pH since the produced silica can be gradually dissolved into silicic acid, resulting in a lower oxygen content in the particles and making new Si_3N_4 surface available [29, 39]. Therefore, from this perspective the untreated powder should have the most oxygen-rich surface oxide layer and it may explain why this sample resulted to be more silica-like according to the zeta potential measurements. On the other hand, for the treated powders the greater exposure of nitride groups, which become hydrolyzed, in turn facilitates the protonation of amine sites in the acidic pH range and could justify the zeta potential sign reversal and the positive potential values for $6 < pH < 8$. A study from Bergström and Bostedt (1990) [1] analyzed the effect of different conditioning treatments on the electrokinetic properties of Si_3N_4 powders, especially testing different conditioning pH values and timing, and it was found that both alkaline (pH = 9, pH = 11) and acidic (pH = 3) treatments caused an increase in pH_{iep} with respect to the as-received powders, with positive zeta-potential values for up to pH = 7.6. The same authors starting

from reactions (4)-(6), and assuming NaCl as electrolyte thanks to the absence of specific adsorption, were able to develop a model for the relationship between surface site occupancy and pH_{iep}, calculating that an equal number of silanol and primary amine sites would correspond to $pH_{iep} = 7.9$. This value is in agreement with the experimental i.e.p. found for the pH-treated powders in the present study (i.e. the second charge reversal point), nevertheless it remains unclear why the measured zeta-potential is negative for $4 < pH < 5.5$. The emergence of new non-oxidized Si_3N_4 surface, more markedly with alkaline pH treatments, could also explain the trends revealed by XPS analysis.

The information obtained from the first two characterization methods (FTIR and Raman spectroscopy) may appear in contrast with the results of the other two types of analysis (zeta-potential measurements and XPS), however it must be considered that the latter two techniques only assess the outermost surface of the particles - with a penetration depth up to few nanometers with XPS - while the information contained in the vibrational spectra comes from a depth of the order of micrometers, thus intrinsically preventing a direct correspondence of the results.

3.4 Conclusion

In order to evaluate the effect of pH on silicon nitride powder, different samples were prepared by exposing the powders to aqueous environment at initial pH 5.5, 6.5, 7.5, 8 and 8.5 for up to 24h and 72h and the purified powders were subsequently characterized by Raman spectroscopy, ATR-FTIR spectroscopy, X-ray Photoelectron Spectroscopy and zeta potential measurements. The results were always compared with the as-received Si_3N_4 commercial powder. All the experiments revealed that the chemistry and bonding structure of silicon nitride was altered after the treatments, with variations among the samples treated in different pH and time conditions. The characterization by vibrational spectroscopies mainly displayed the emergence of spectral features which can be related to the presence of oxygen in the crystalline structure, to a variable extent depending on the pH treatment: pH groups 5.5 and 8 emerged significantly in the FTIR analysis while in the Raman spectra there was a clear separation between the effects of acidic and basic pH treatments, suggesting a lower degree of oxidation of the powders in alkaline environment. Focusing on the very surface layers of the particles, XPS and zeta-potential measurements evidenced a decrease in oxygen-related signals and an increase in the relative number of nitride bonds, more evidently with the alkaline treatments and probably related to the dissolution of silicon oxide and the availability of new Si_3N_4 surface.

References

1. Bergström, L. & Bostedt, E. Surface chemistry of silicon nitride powders: Electrokinetic behaviour and ESCA studies. *Colloids and Surfaces* **49,** 183–197. doi:10.1016/0166-6622(90)80101-9 (1990).
2. Malghan, S. G. Dispersion of Si_3N_4 powders: surface chemical interactions in aqueous media. *Colloids and Surfaces* **62,** 87–99. doi:10.1016/0166-6622(92)80039-5 (1992).
3. Laarz, E. *Colloidal Processing of Non-Oxide Ceramic Powders in Aqueous Medium* PhD thesis (KTH, Royal Institute of Technology, Stockholm, 2000).
4. Zhang, J., Ye, F., Jiang, D. & Iwasa, M. Dispersion of Si_3N_4 powders in aqueous media. *Colloids and Surfaces A: Physicochemical and Engineering Aspects* **259,** 117–123. doi:10.1016/j.colsurfa.2005.02.006 (2005).
5. Lowry, G. V. *et al.* Guidance to improve the scientific value of zeta-potential measurements in nanoEHS. *Environmental Science: Nano* **3,** 953–965. doi:10.1039/c6en00136j (2016).
6. Wada, N., Solin, S. A., Wong, J. & Prochazka, S. Raman and IR absorption spectroscopic studies on α, β, and amorphous Si_3N_4. *Journal of Non-Crystalline Solids* **43,** 7–15. doi:10.1016/0022-3093(81)90169-1 (1981).
7. Kislyi, P., Posun'ko, L. & Malogolovets, V. Phase composition of Si_3N_4 powders synthesized by various methods. *Soviet Powder Metallurgy and Metal Ceramics* **27,** 407–410. doi:https://link.springer.com/content/pdf/10.1007/BF00797693.pdf (1988).
8. Cai, Y., Zhang, L., Zeng, Q., Cheng, L. & Xu, Y. First-principles study of vibrational and dielectric properties of β-Si_3N_4. *Physical Review B - Condensed Matter and Materials Physics* **74,** 174301. doi:10.1103/PhysRevB.74.174301 (2006).
9. Batan, A., Franquet, A., Vereecken, J. & Reniers, F. Characterisation of the silicon nitride thin films deposited by plasma magnetron. *Surface and Interface Analysis* **40,** 754–757. doi:10.1002/sia.2730 (2008).
10. Liang, C. H. *et al.* Correlation between composition, microstructure, and emission properties in Nd-doped Si-rich Si oxynitride films: Investigation into the nature of the sensitizer. *Nanotechnology* **30.** doi:10.1088/1361-6528/aaea23 (2019).
11. Huang, L., Hipps, K. W., Dickinson, J. T., Mazur, U. & Wang, X. D. Structure and composition studies for silicon nitride thin films deposited by single ion bean sputter deposition. *Thin Solid Films* **299,** 104–109. doi:10.1016/S0040-6090(96)09446-1 (1997).
12. Ni, Z. *et al.* Surface characterization of silicon nitride powder and electrokinetic behavior of its aqueous suspension. *Ceramics International* **46,** 9530–9537. doi:https://doi.org/10.1016/j.ceramint.2019.12.215 (2020).
13. Sahu, B. S. *et al.* Dependence of hydrogen and oxygen incorporation on deposition parameters in photochemical vapor deposited mercury free silicon nitride films. *Thin Solid Films* **446,** 23–28. doi:10.1016/S0040-6090(03)01320-8 (2004).
14. San Andrés, E. *et al.* Rapid thermal annealing effects on the structural properties and density of defects in SiO_2 and SiN_x: H films deposited by electron cyclotron resonance. *Journal of Applied Physics* **87,** 1187–1192. doi:10.1063/1.371996 (2000).
15. Debieu, O. *et al.* Structural and optical characterization of pure Si-rich nitride thin films. *Nanoscale Research Letters* **8.** doi:10.1186/1556-276X-8-31 (2013).
16. Ono, H., Ikarashi, T., Ando, K. & Kitano, T. Infrared studies of transition layers at SiO2/Si interface. *Journal of Applied Physics* **84,** 6064. doi:10.1063/1.368917 (1998).
17. Socrates, G. *Infrared and Raman Characteristic Group Frequencies: Tables and Charts* 3rd edition. ISBN: 978-0-470-09307-8 (John Wiley & Sons, 2004).
18. Honda, K., Yokoyama, S. & Tanaka, S.-i. Assignment of the Raman active vibration modes of β-Si_3N_4 using micro-Raman scattering. *Journal of Applied Physics* **85,** 7380–7384. doi:10.1063/1.369366 (1999).
19. Volodin, V. A., Efremov, M. D., Gritsenko, V. A. & Kochubei, S. A. Raman study of silicon nanocrystals formed in SiN_x films by excimer laser or thermal annealing. *Applied Physics Letters* **73,** 1212–1214. doi:10.1063/1.122130 (1998).
20. Biesuz, M. *et al.* First synthesis of silicon nanocrystals in amorphous silicon nitride from a preceramic polymer. *Nanotechnology* **30,** 255601. doi:10.1088/1361-6528/ab0cc8 (2019).
21. Everitt, B. S. & Skrondal, A. *The Cambridge Dictionary of Statistics* 4th edition. ISBN: 9780521766999 (Cambridge University Press, 2010).
22. Greczynski, G. & Hultman, L. X-ray photoelectron spectroscopy: Towards reliable binding energy referencing. *Progress in Materials Science* **107,** 100591. doi:10.1016/j.pmatsci.2019.100591 (2020).
23. Matsuoka, M., Isotani, S., Sucasaire, W., Zambom, L. S. & Ogata, K. Chemical bonding and composition of silicon nitride films prepared by inductively coupled plasma chemical vapor deposition. *Surface and Coatings Technology* **204,** 2923–2927. doi:10.1016/j.surfcoat.2010.02.071 (2010).
24. Ahmad, N. & Sueyoshi, H. Properties of Si3N4-TiN composites fabricated by spark plasma sintering by using a mixture of Si3N4 and Ti powders. *Ceramics International* **36,** 491–496. doi:10.1016/j.ceramint.2009.09.029 (2010).
25. Ni, Z. *et al.* Surface modification of ultrafine silicon nitride powders by calcination. *International Journal of Applied Ceramic Technology* **16,** 1364–1372. doi:10.1111/ijac.13232 (2019).
26. Graf, N. *et al.* XPS and NEXAFS studies of aliphatic and aromatic amine species on functionalized surfaces. *Surface Science* **603,** 2849–2860. doi:10.1016/j.susc.2009.07.029 (2009).
27. Shircliff, R. A. *et al.* Angle-Resolved XPS Analysis and Characterization of Monolayer and Multilayer Silane Films for DNA Coupling to Silica. *Langmuir* **29,** 4057–4067. doi:10.1021/la304719y (2013).

28. Avadiar, L. & Leong, Y. K. Interactions of PEI (polyethylenimine)-silica particles with citric acid in dispersions. *Colloid and Polymer Science* **289,** 237–245. doi:10.1007/s00396-010-2351-2 (2011).
29. Bergström, L. & Pugh, R. J. Interfacial Characterization of Silicon Nitride Powders. *Journal of the American Ceramic Society* **72,** 103–109. doi:10.1111/j.1151-2916.1989.tb05961.x (1989).
30. Raval, N. *et al. Importance of physicochemical characterization of nanoparticles in pharmaceutical product development* in *Basic Fundamentals of Drug Delivery* (Academic Press, 2018). doi:10.1016/B978-0-12-817909-3.00010-8.
31. Greil, P., Nitzsche, R., Friedrich, H. & Hermel, W. Evaluation of oxygen content on silicon nitride powder surface from the measurement of the isoelectric point. *Journal of the European Ceramic Society* **7,** 353–359. doi:10.1016/0955-2219(91)90058-8 (1991).
32. National Institute of Standards and Technology. NIST-JANAF Thermochemical Tables. doi:10.18434/T42S31 (1998).
33. Mezzasalma, S. & Baldovino, D. Characterization of silicon nitride surface in water and acid environment: A general approach to the colloidal suspensions. *Journal of Colloid and Interface Science* **180,** 413–420. doi:10.1006/jcis.1996.0320 (1996).
34. Scopel, W. L., Fantini, M. C., Alayo, M. I. & Pereyra, I. Local structure and bonds of amorphous silicon oxynitride thin films. *Thin Solid Films* **413,** 59–64. doi:10.1016/S0040-6090(02)00346-2 (2002).
35. Philipp, H. R. Optical and bonding model for non-crystalline SiOx and SiOxNy materials. *Journal of Non-Crystalline Solids* **8-10,** 627–632. doi:10.1016/0022-3093(72)90202-5 (1972).
36. Takase, A. & Tani, E. Raman spectroscopic study of β-sialons in the system Si_3N_4-Al_2O_3-AlN. *Journal of Materials Science Letters* **3,** 1058–1060. doi:10.1007/BF00719763 (1984).
37. Wang, L., Sigmund, W. & Aldinger, F. Systematic approach for dispersion of silicon nitride powder in organic media: I, Surface chemistry of the powder. *Journal of the American Ceramic Society* **83,** 691–696. doi:10.1111/j.1151-2916.2000.tb01260.x (2000).
38. Bock, R. M. *et al.* Surface modulation of silicon nitride ceramics for orthopaedic applications. *Acta Biomaterialia* **26,** 318–330. doi:10.1016/j.actbio.2015.08.014 (2015).
39. Crundwell, F. K. On the Mechanism of the Dissolution of Quartz and Silica in Aqueous Solutions. *ACS Omega* **2,** 1116–1127. doi:10.1021/acsomega.7b00019 (2017).

4 The effect of Si_3N_4 powder on bacteria: different concentrations

The experiment reported in this chapter was a preliminary study which focused on the interaction of silicon nitride powders with bacteria, particularly addressing the role of powder concentration. The most effective concentration value was selected for performing subsequent experiments in which other parameters were investigated (Chapter 5). The powder is not soluble in water nor in other aqueous media, hence the term "concentration" indicates the amount of powder dispersed in the liquid phase.

4.1 Materials and methods

4.1.1 Bacterial culture

S. epidermidis (14990® ATCC™) was cultured[12] in liquid at the Kyoto Prefectural University of Medicine using brain heart infusion (BHI) broth medium. Alternative media were prepared by adding selected amounts of Si_3N_4 powder to obtain two treatment groups as follows: 16 mg of Si_3N_4 per mL of BHI, 4 mg of Si_3N_4 per mL of BHI. A third group was cultured in BHI with no powder and constituted the control group. From now on the groups are labeled as "16 mg/mL", "4 mg/mL" and "CTRL", respectively. The powder was sterilized by UV irradiation before addition to the culture medium, then suspended in the liquid before inoculation. Incubation at 37°C took place under aerobic conditions for two time-points: 0 h (meaning less than one hour, around 30 minutes) and 24 h. All the samples were placed on a rotator which allowed constant agitation of the powder and prevented its deposition on the bottom of the culture vial.

4.1.2 Microbial viability assay

After the exposure time of 0 h and 24 h, bacterial metabolism was examined using a colorimetric assay (Microbial Viability Assay Kit-WST, Dojindo, Kumamoto, Japan). This assay employed a water-soluble tetrazolium salt (WST-8) which, in the presence of an electron mediator, is reduced by NAD(P)H to a formazan dye of a strong orange color. Since the amount of formazan product is proportional to the NAD(P)H concentration, it can be assumed to be directly proportional to the number of viable microorganisms. The coloring reagent was added to each sample and the solutions were analyzed using a microplate reader monitoring the absorbance at 450 nm, as specified in the manufacturer technical manual [1]. Four replicates have been used to calculate mean values and standard deviations.

4.1.3 Raman spectroscopy

Raman spectra were collected after culture of *S. epidermidis* in BHI broth as well as in BHI broth added with two different concentrations of Si_3N_4 powder. For each sample, after a thorough mix of the medium, few drops were immediately placed on a glass substrate and allowed to slightly dry in order to reduce the fluorescence background emitted by BHI broth. Spectra were collected using a confocal Raman microscope (Ramantouch; Nanophoton Corporation, Osaka, Japan), which employed a single monochromator connected to a thermoelectric-cooled CCD detector (1340 pixels for single-point measurement). The excitation wavelength was set at 532 nm with a power of $\sim$ 10 mW at the sample surface. A 50x objective lens was employed. The Raman spectra were acquired with an exposure time of 5 s. Average Raman spectra for each sample were calculated from 6 measurements at different

[12] details about initial CFU and dilutions in Appendix A

random locations. Raman spectral acquisition and pre-processing of raw data (i.e. baseline subtraction, smoothing, normalization and fitting) were carried out using commercially available softwares (LabSpec - Horiba, Kyoto, Japan and OriginPro 2018 - OriginLab Corp., Northampton, Massachusetts). Baseline subtraction for all the spectra has been obtained according to the polynomial method using a polynomial function of degree 8. Fitting was performed using Gaussian/Lorentzian functions. Intensity ratios of selected bands were quantified and used for comparisons as they are less affected by pre-processing methods and background fluctuations.

4.2 Results

4.2.1 Microbial viability assay

The results of the WST assay are reported in Figure 26, in the form of mean values with error bars representing the standard deviation. Statistical analysis was performed by two-sample Student's *t* tests, with significance indicated as: $**$ for $p < 0.01$, $*$ for $p < 0.05$, *n. s.* for non-significant ($p > 0.05$).

Viability was assessed at 0 h and 24 h. At both time steps the results in the different treatment groups showed a clear trend in which the control group (without silicon nitride) had the highest absorbance value (2.4 ± 0.73 at 0 h, 2.45 ± 0.7 at 24 h), indicating the largest number of living bacteria compared to the other investigated treatments. The lowest value was obtained for the 16 mg/mL Si_3N_4 powder concentration (0.46 ± 0.21 at 0 h, 0.17 ± 0.03 at 24 h), while the group with 4 mg/mL Si_3N_4 had an intermediate value (1.08 ± 0.21 at 0 h, 1.02 ± 0.24 at 24 h). The differences among mean values of different treatment groups pertaining to the same time point were significant, whereas comparing different time points for the same treatment group the only significant difference was obtained for the 16 mg/mL group, showing a much lower value at 24 h.

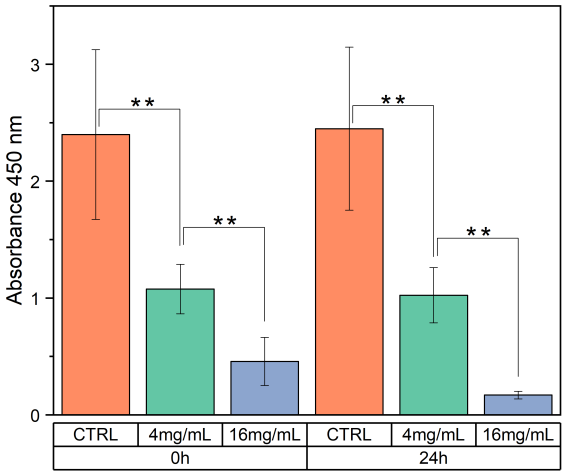

Figure 26: WST assay diagram for *S. epidermidis* culture with different Si_3N_4 concentrations.

4.2.2 Raman spectroscopy

All the spectra were acquired in the spectral range 834 - 1800 cm^{-1} and subjected to pre-processing. The spectrum of the glass substrate was also acquired and showed a broad band centered at 916 cm^{-1}, consequently a peak normalization procedure was carried out for all the spectra with respect to the highest signal in the "glass region" (874 - 950 cm^{-1}) which was assumed to be a constant throughout all the experiments. Hence, this spectral region was not considered for making comparisons among different treatment groups. Peak fitting was carried out for each spectrum, distinguishing two separate regions for clarity: region I (834 - 1290 cm^{-1}), region II (1290 - 1800 cm^{-1}). An example of a fitted spectrum for a sample of the control group at 0 h is shown in Figure 27 and Figure 28, respectively for the two regions, where the bands have been numbered. The vibrational modes for each individual band were assigned according to their physical origin trying to specify, when applicable, the cellular compounds in which they originate. The proposed assignments are reported in Table VI and Table VII.

Region I is characterized by the sharp band of phenylalanine ring breathing at 998 cm^{-1} [2, 3] (Band 14), followed by a series of bands related to C–C stretching in lipids from 1059 cm^{-1} to 1092 cm^{-1} [2, 4–6] (Bands 18-21). Band 21, in particular, can also be assigned to the stretching mode of phosphodioxy groups and sometimes is used as a reference signal for nucleic acids [2, 7]. Another relevant peak is located at 1121 cm^{-1} [2] (Band 24) for the stretching of the C–O bond in carbohydrates. This band has been suggested to be a potential marker for ribose [8].

The last section of region I is dominated by the amide III modes from 1231 cm^{-1} to 1280 cm^{-1} [2, 9] (Bands 34-37) comprehensive of C–N stretching coupled with N–H bending vibrations, which are reported to be sensitive to the protein secondary structure [9]. According to the same references, these bands are likely to have contributions also from =CH bending modes in lipids.

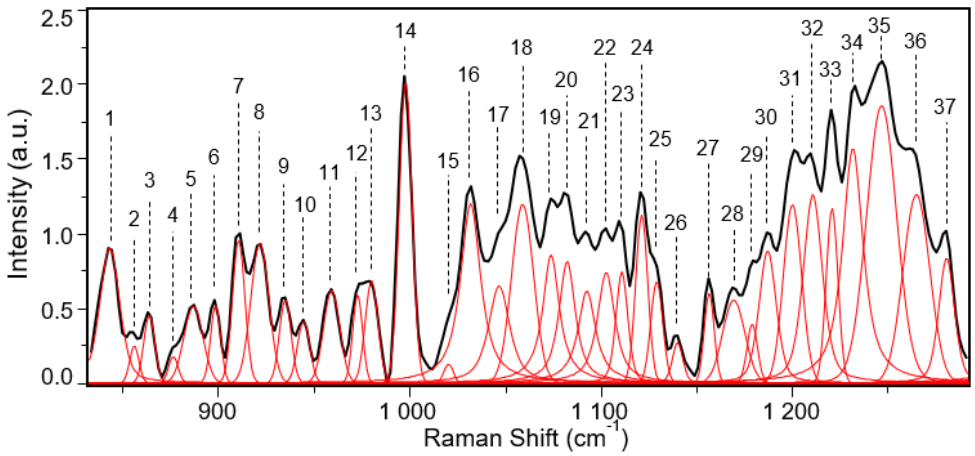

Figure 27: Normalized deconvoluted Raman spectrum in region I (*S. epidermidis*, CTRL group, 0h).

Table VI: Band labeling, tentative assignment and related references for Raman peaks in region I.

Band	Wavenumber (cm^{-1})	Assignment	References
1	843	tyrosine	[2, 3]
2	856	amino acid side chain vibrations of proline and hydroxyproline	[10]
3	864	C–C ring breathing, C–O–C 1,4 glycosidic link	[11, 12]
4	876	C–O–H ring in carbohydrates	[2]
5	887	CH_2 rocking	[3, 11]
6	898	C–O–C in plane symmetric ring deformation	[11]
7	910	C–O, C–C stretching in ribose	[7, 13]
8	921	proline	[3, 14]
9	935	C–C backbone stretching in proteins (α helix), C–O–H glycosidic in carbohydrates	[2, 12]
10	944	CH_2 rocking in membrane lipids	[12]
11	959	CH_3 (terminal) rocking	[11]
12	973	CH_3 rocking, CCH bending in proteins; ribose	[7, 15]
13	981	C–C in proteins (β sheet), =CH bend in lipids	[2]
14	998	symmetric ring breathing phenylalanine	[2, 3]
15	1020	carbohydrates peak for solutions	[8]
16	1031	C–H in plane phenylalanine	[2, 3]
17	1046	C–C aromatic ring	[12]
18	1059	*trans* C–C stretching in lipids	[4, 5]

Table VI: (continued)

Band	Wavenumber (cm^{-1})	Assignment	References
19	1073	chain C–C stretching in lipids; C–O, C–C stretching in carbohydrates	[2, 6]
20	1082	*gauche* C–C stretching in lipids	[4]
21	1092	PO_2^- stretching in nucleic acids, C–C stretching in lipids	[2, 4, 7]
22	1103	carbohydrates	[14]
23	1111	C–O, C–C in carbohydrates	[6]
24	1121	C–O stretching in carbohydrates (ribose marker)	[2, 8]
25	1129	C–C in lipids; C–N stretching in proteins	[2, 16]
26	1140	adenine ring breathing mode	[3, 17]
27	1156	C–C stretching in carotenoids	[6, 11]
28	1169	C–H of tyrosine	[2, 6, 18]
29	1179	tyrosine, phenylalanine, amide III	[6, 12]
30	1187	cytosine, guanine, adenine	[5, 19]
31	1200	hydroxyproline, tyrosine	[3, 5]
32	1210	C–C_6H_5 in phenylalanine and tryptophan	[2, 20]
33	1220	C–N stretching	[18]
34	1231	amide III (β sheets); =CH in lipids	[2, 9]
35	1246	amide III (random structures); =CH in lipids	[2, 9]
36, 37	1264, 1280	amide III (α helices); =CH in lipids	[2, 9]

In region II the numerous vibrational modes arise from all the principal constituents of the cellular material, comprising some of the building blocks of the bacterial cell wall. The first bands (38-40) from 1297 cm^{-1} to 1313 cm^{-1} are assigned to CH_2 deformation, rocking and twisting modes in lipids [2, 6, 12, 16] and could be assumed as a marker for membrane lipids [4]. At slightly higher wavenumber, Band 42 at 1335 cm^{-1} arises from the OH deformation in polysaccharides [3, 8, 12], but can also be assigned to tryptophan side chain [9]. In the present case the polysaccharide assignment potentially reflects the presence of teichoic acids (TAs), which are in fact rich in carbohydrates and hydroxyl groups. Since TAs can be attached to either the lipid membrane (lipoteichoic acid, LTA) or the peptidoglycan layer of the cell wall (wall teichoic acid, WTA), the analysis of changes related to Band 42 may reveal alterations in the bacterial wall and membrane structures.

Bands 43-44, respectively at 1349 cm^{-1} and 1369 cm^{-1}, are assigned to ring breathing modes of the nitrogenous bases adenine, guanine and thymine [2, 18] and are of particular interest for monitoring nucleic acids. An additional band which can be linked to the cell wall structure is located at 1388 cm^{-1} (Band 45) and assigned to CH_3 symmetrical deformation in N-acetylglucosamine (NAG) and N-acetylmuramic acid (NAM) [11], whose units are alternated and repeated several times in the peptidoglycan polymer which constitutes a thick layer in the cell wall of Gram-positive bacteria such as *S. epidermidis*. As regarding DNA-related signals, band 48 at 1429 cm^{-1} has been assigned to CH_2 deformation in deoxyribose [9, 19].

The very intense band at 1446 cm^{-1} (Band 49) pertains to the CH_2 scissoring mode from all cellular components [11, 12, 21], thus it is exploited in the following analysis as an internal reference peak to calculate intensity ratios and compare trends related to the biomolecules of major interest.

The bands from 1527 cm^{-1} to 1571 cm^{-1} (Bands 55-59) are specific of the amide II NH deformation and CN stretching [11, 12]. Other protein-related bands are found in the range 1590-1637 cm^{-1}, where Bands 61-64 are assigned to the C=C stretching in aromatic amino acids such as phenylalanine, tyrosine and tryptophan [2, 3, 6, 12], whereas Band 65 is assigned to C=O stretching in amide I β sheets [3, 9].

Finally the range 1703-1792 cm^{-1} (Bands 72-82) displays several peaks assigned to the C=O stretching in lipids [2, 3, 6, 9, 12, 22, 23].

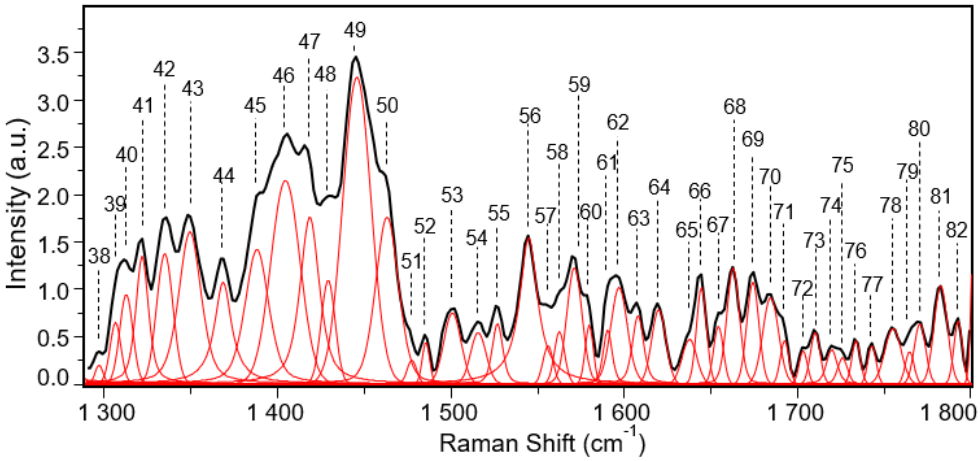

Figure 28: Normalized deconvoluted Raman spectrum in region II (*S. epidermidis*, CTRL group, 0h).

Table VII: Band labeling, tentative assignment and related references for Raman peaks in region II.

Band	Wavenumber (cm^{-1})	Assignment	References
38	1297	CH_2 deformation, CH_2 twist in lipids	[2, 16]
39, 40	1307, 1313	CH_2 rocking, CH_2 twist in lipids (membrane lipids)	[4, 6, 12]
41	1322	in plane CH_2 deformation	[11]
42	1335	OH deformation in polysaccharides, tryptophan	[3, 8, 9, 12]
43	1349	adenine and guanine, CH deformation in proteins	[2]
44	1369	T, A, G (ring breathing modes of the DNA/RNA bases)	[18]
45	1388	CH_3 symmetrical deformation (NAG, NAM)	[11]
46	1405	CO_2^- stretching in α-amino acids	[3, 12]
47	1419	CH_3 asymmetrical deformation	[11]
48	1429	CH_2 deformation (deoxyribose)	[9, 19]
49	1446	CH_2 scissoring (fatty acids, phospholipids, proteins, saccharides)	[11, 12, 21]
50	1463	CH_2 deformation (carbohydrates, lipids, proteins)	[2, 24]
51-53	1477-1501	CH_2 deformation	[2, 12]
54	1516	C=C stretching in carotenoids	[3, 6, 11, 14]
55, 56	1527, 1545	amide II, N-acetyl-related bands (amide II)	[12]
57-59	1556-1571	NH deformation and CN stretching in amide II	[11, 12]
60	1580	guanine and adenine ring stretching	[2, 16]
61, 62	1590, 1597	C=C in phenylalanine	[2, 6, 14, 16]
63	1608	C=C in phenylalanine and tyrosine	[2]
64	1620	C=C in tyrosine and tryptophan	[2, 3, 12]
65	1637	C=O stretching in amide I (β sheets)	[3, 9, 14]
66-71	1644-1692	C=O stretching in amide I C=C stretch in lipids (unsaturated fatty acids)	[2, 3, 12]
72, 73	1703, 1710	C=O stretching in lipids	[22]
74-80	1720-1771	C=O ester stretching in lipids	[2, 3, 6, 12]
81, 82	1782, 1792	C=O stretching in lipids	[9, 23]

NAG: N-acetylglucosamine; NAM: N-acetylmuramic acid

For each sample, an average spectrum was obtained from six spectra acquired from random locations. The average spectra of the different treatment groups are reported in Figure 29, where the bands of particular interest are highlighted with a grey shade. These bands were selected as markers for specific cellular components and exploited to assess intensity variations among different treatment groups.

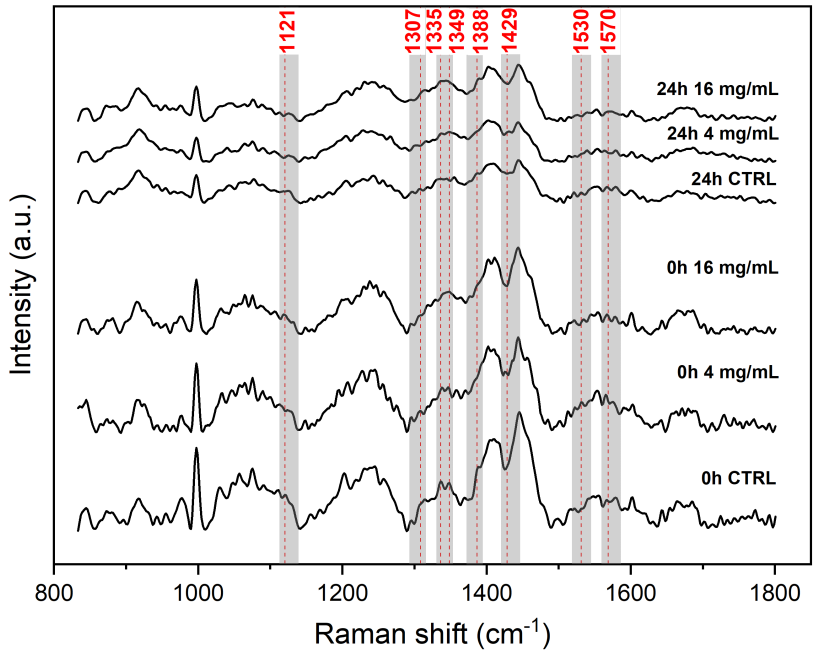

Figure 29: Average Raman spectra of *S. epidermidis* cultured with different Si_3N_4 concentrations at time points 0h and 24h. Regions highlighted by grey rectangles represent bands of interest which are used to calculate intensity ratios.

From lower to higher wavenumber the proposed markers are located as follows: 1121 cm^{-1} (Band 24) for ribose in RNA, 1307 cm^{-1} (Band 39) for membrane lipids, 1335 cm^{-1} (Band 42) for polysaccharides, 1349 cm^{-1} (Band 43) for adenine and guanine, 1388 cm^{-1} (Band 45) for NAG and NAM, 1429 cm^{-1} (Band 48) for deoxyribose in DNA, 1530 cm^{-1} and 1570 cm^{-1} (Bands 55, 59) for amide II in proteins. In each of the original spectra, as mentioned earlier, Band 49 (1446 cm^{-1}) was used to calculate intensity ratios with these selected bands and the results were reported in the form of box-and-whiskers plots to visualize both in-group and between-group variability. Given the small sample size for each treatment group and the presence of outliers, one-sided Mann-Whitney tests were performed to evaluate differences between groups, with significance expressed as: $**$ for $p < 0.01$, $*$ for $p < 0.05$, *n.s.* for non-significant.

As regarding nucleotide-related bands (Figure 30), the ratio of the band of ribose over Band 49 (CH_2 scissoring - all cellular components) was significantly lower for the treatment group with 16 mg/mL Si_3N_4 at both 0 h and 24 h (Figure 30 **a**) compared to 4 mg/mL and CTRL groups, suggesting a decrease in RNA content with the highest Si_3N_4 concentration. A similar trend is observed for the deoxyribose band at 24 h (Figure 30 **c**), however in this case at 0 h the only significant difference was between the 16 mg/mL group and the 4 mg/mL group. Lastly, considering adenine and guanine, at 0 h the ratio with Band 49 was significantly higher in the 4 mg/mL group compared to the CTRL group only, on the other hand at 24 h the difference was also significant between 4 mg/mL and 16 mg/mL, with the former group having the highest value (Figure 30 **b**).

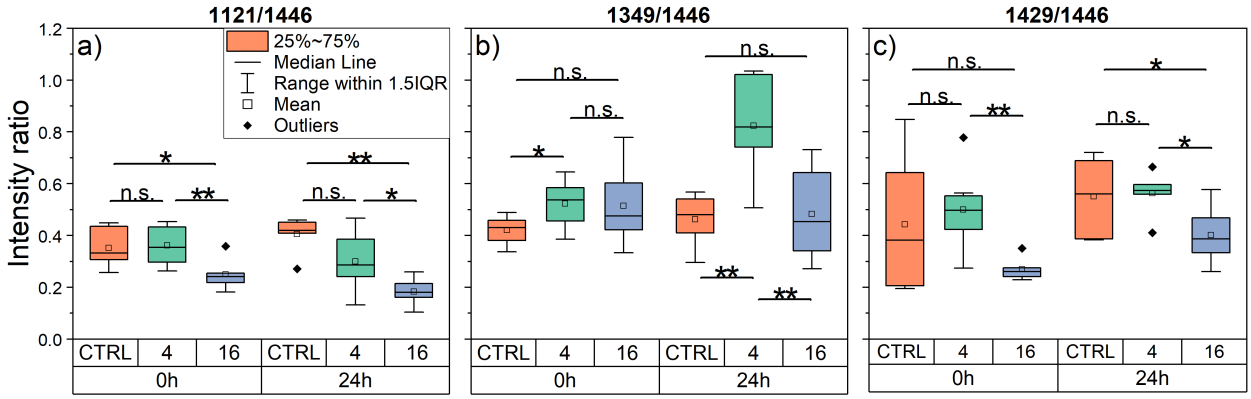

Figure 30: Intensity ratios for nucleotide-related Raman bands. **a)** Ribose in RNA (1121 cm^{-1}) over all cellular components (1446 cm^{-1}); **b)** adenine and guanine in nucleic acids (1349 cm^{-1}) over all cellular components (1446 cm^{-1}); **c)** deoxyribose in DNA (1429 cm^{-1}) over all cellular components (1446 cm^{-1}).

A closer insight into the relative changes in RNA and DNA content in *S. epidermidis* under different treatment conditions was obtained by calculating the direct ratio between ribose and deoxyribose bands. As it can be seen in Figure 31, at 0 h there were no significant variations between different groups whereas at 24 h the ratio was higher in the CTRL group compared to the other two groups, indicating that the presence of silicon nitride in the culture medium for 24 h caused a decrease in RNA content relative to DNA.

Changes in protein content were investigated by taking the intensity ratio between the amide II band at 1530 cm^{-1} and, once again, Band 49 (1446 cm^{-1}). At both time points the ratio was significantly lower for the group with the highest Si_3N_4 concentration compared to the CTRL group but not to the 4 mg/mL group (Figure 32), probably due to high in-group variability.

For what concerns bands related to cell membrane and bacterial cell wall, the investigated ratios are reported in Figure 33. The ratio between the band assigned to polysaccharides and Band 49 (CH_2 scissoring, all cellular components) displayed no significant differences at 0h while after 24 h of culture there was a significant decrease in the 16 mg/mL group compared to both 4 mg/mL and CTRL group (Fig.33 **b**). For membrane lipids the ratio was significantly higher for group 4 mg/mL with respect to the CTRL at 0h and to both the other groups at 24h (Figure 33 **a**). High in-group variability and no clear trend were obtained for the bands assigned to NAG and NAM, in this case the only significant difference was found at 24h between CTRL and the 16 mg/mL group, the latter having the lower value (Fig.33 **c**).

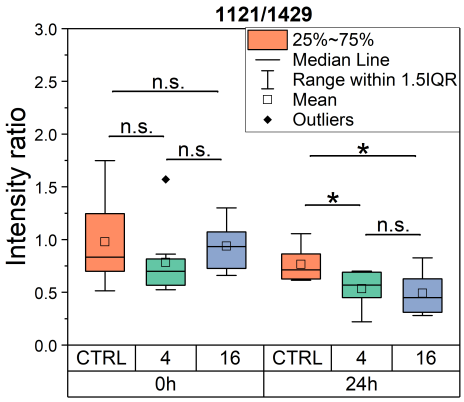

Figure 31: Intensity ratio between ribose and deoxyribose Raman band (1121 cm^{-1} and 1429 cm^{-1} respectively).

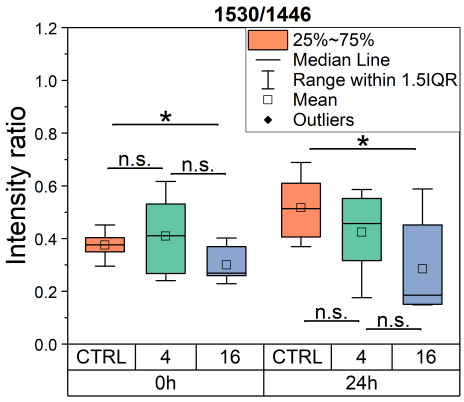

Figure 32: Intensity ratio for amide II Raman band (1530 cm^{-1}) over Band 49 (1446 cm^{-1}, CH_2 scissoring - all cellular components).

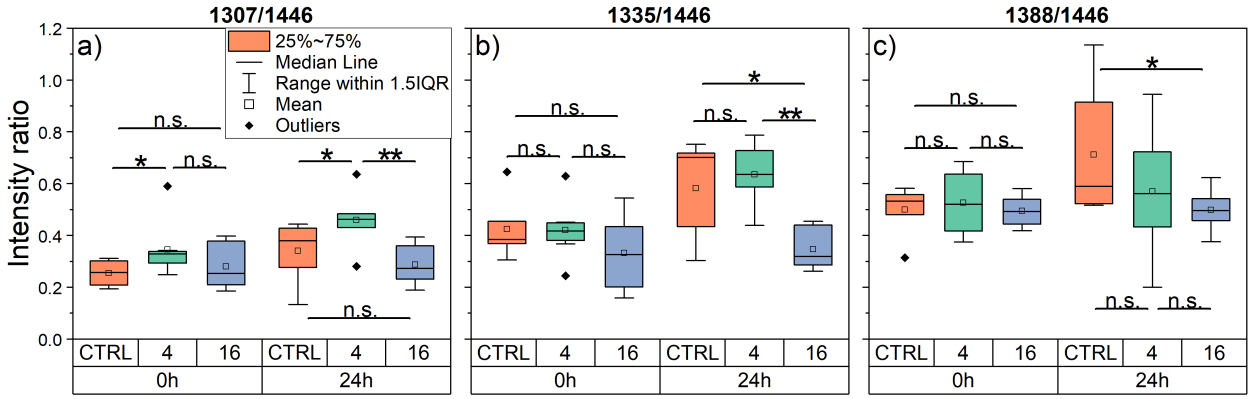

Figure 33: Intensity ratios for Raman bands related to cell membrane and cell wall. **a)** membrane lipids (1307 cm^{-1}) over all cellular components (1446 cm^{-1}); **b)** OH groups in polysaccharides (1335 cm^{-1}) over all cellular components (1446 cm^{-1}); **c)** NAG and NAM (1388 cm^{-1}) over all cellular components (1446 cm^{-1}).

4.3 Discussion

The interaction between bacteria and materials is complex and implies an intersection of physical, chemical and biological processes whose rigorous and exhaustive unveiling is far beyond the possibilities of this study. Nevertheless, the combination of cell viability assays with Raman spectroscopy constituted a valid tool to grasp important aspects underlying the phenomenon. Starting from the WST assay results, it is evident that the viability of *S. epidermidis* was detrimentally affected by the presence of Si_3N_4 in the culture medium since at all time points the Si_3N_4-treated samples were found to have significantly lower absorbance at 450 nm compared to the CTRL group (Fig.26). In particular, the highest powder concentration proved to be the most effective one, suggesting that the amount of dispersed Si_3N_4 is a relevant factor in the interaction with bacterial growth.

Several studies have reported on the surface chemistry of silicon nitride in aqueous solutions, showing that hydroxyl ions may start a nucleophilic attack on Si_3N_4, proceeding through a substitution reaction which results in hydrolysis and dissolution of the silicon compound [25, 26]. The proposed overall reaction is $Si_3N_4 + 6\ H_2O \longleftrightarrow 3\ SiO_2 + 4\ NH_3$ [26, 27], where the ammonia product is present both in its ionized (NH_4^+) and un-ionized (NH_3) form. The two forms have contradictory yet coexistent roles: on the one hand a nutrient, the preferred nitrogen source for most bacteria, on the other hand a cytotoxic agent [28]. The proportion between the two forms is strictly dependent on pH by the following relation: $f = 1/(10^{\,pK_a - pH} + 1)$, where f is the fraction of NH_3 over total ammonia ($NH_3 + NH_4^+$) and pK_a is the acid dissociation constant of ammonia, given by $pK_a = 0.09018 + 2729.29/T$ with T being the temperature in Kelvin [29]. For instance, at 298 K and pH 7 the fraction of unionized ammonia is about 0.56% while almost 5% at pH 8 and 36% at pH 9. Ammonia toxicity for bacteria has been traced back to at least two possible mechanisms: unprotonated ammonia, being more lipophilic and able to readily permeate through cellular membranes, could directly inhibit the functions of cytosolic enzymes; alternatively, if the intracellular pH is lower than the extracellular pH, part of the permeated NH_3 is converted into NH_4^+ intracellularly and the accumulation of this cation can influence the concentration of other important cations such as K^+, eventually causing osmotic or ionic stress [28, 30].

The effect of silicon nitride on *S. epidermidis* has been previously evaluated by culturing the bacteria on bulk samples of Si_3N_4 and ammonia was designated as a key player in the fatal destabilization of cellular mechanisms [31]. In the present study, a higher amount of ammonia is likely to be leached in

the culture medium for samples with a larger amount of dispersed powder (16 mg/mL Si_3N_4), resulting in more severe stress for *S. epidermidis*.

Despite the inherent complexity of Raman spectra of biological samples, the ratiometric analysis of selected Raman bands allowed to investigate variations in cellular components among the three treatment groups at 0h and 24h, getting insights on possible interaction mechanisms of *S. epidermidis* with Si_3N_4. Concerning RNA and DNA, the intensity of their marker bands were found to be significantly lower in the 16 mg/mL group compared to both 4 mg/mL and CTRL at all time points (Fig.30 **a**,30 **c**), suggesting that the highest Si_3N_4 amount has a detrimental effect on nucleic acids content. Although the same trend was identified for the two nucleic acids, a direct ratio of the two bands revealed that their proportion had no significant variations at 0h but at 24h the Si_3N_4-treated groups had lower RNA/DNA values with respect to the CTRL (Fig.31). This could be a consequence of unfavourable growth conditions and hampered growth rate, in fact the RNA/DNA ratio has been reported as an indicator of metabolic activity since it shows a positive linear correlation with growth rate for *E. coli* and other bacteria [32, 33]. For a given number of viable cells, the RNA content is more susceptible to metabolic changes in comparison with the more stable DNA content. Further to this point, researchers have shown that in osmotic stress conditions the bacterial nucleoid undergoes hyper-condensation with a concurrent transient dissociation of the RNA polymerase (RNAP), leading to a significant inhibition of transcription, hence a decrease in the amount of RNAs [34]. Other stress-related survival-mechanisms involve guanosine (penta)tetraphosphate, (p)ppGpp, an alarmone nucleotide which can hinder RNAP activity by binding to its β'- and ω- subunits, again resulting in a dramatic reduction of RNA levels [35, 36]. On the same theoretical grounds, the lower protein content for the group with higher Si_3N_4 concentration (Fig.32) may be justified by the fact that protein synthesis decreases as a direct consequence of the reduced levels of RNAs necessary for transcription and translation.

The effects with a 4 mg/mL powder concentration seemed to be less pronounced and more unclear, in particular the significant increase in adenine (A) and guanine (G) content seen in Figure 30 **b** did not find a matching increase in the 16 mg/mL group. One hypothesis is that depending on the initial concentration of silicon nitride the bacteria may face the stress conditions with a different timing, therefore the un-matched results between 4 mg/mL and 16 mg/mL groups probably correspond to different stages of the bacterial response mechanism. For example, in the beginning of a stress response, a temporary rise in ATP levels was reported for *E. coli* and attributed to the inhibition of energy-consuming processes [37], among which transcription and translation have a major role. Moreover, as mentioned before, it is probable that (p)ppGpp is involved in the mechanism and several studies reported on its accumulation and high levels during acute survival responses for both Gram-negative and Gram-positive bacteria [36, 38, 39]. High ATP and (p)ppGpp may have contributed to a relative increase in adenine and guanine content and in turn to an increase in the intensity of the A,G -related band for the 4 mg/mL group.

Additional support to the osmotic stress hypothesis was given by the changes in bands assigned to polysaccharides (1335 cm^{-1}) and lipids (1307 cm^{-1}), respectively related to cell wall and cell membrane. The ratio of the polysaccharide band on all cellular components was seen to decrease for the 16 mg/mL groups compared to the other two groups (Fig.33 **b**). Interestingly, a significant increase was identified at 24h for the CTRL and 4 mg/mL groups with respect to the values at 0h whereas the 16 mg/mL group maintained the same level at 0h and 24h. This trend could be interpreted as the cell wall teichoic acids being compromised in the sample with the highest Si_3N_4 concentration. Interestingly, the polysaccharide signal could also be related to polysaccharide intercellular adhesin (PIA) - a key factor for *S. epidermidis* cell-cell adhesion and biofilm formation on biomaterials [40] - and it was reported

that an induced decrease in PIA production could allow a better control of *S. epidermidis* infections [41]. The intensity ratio for the lipid band saw an increase in the 4 mg/mL group with respect to the CTRL and 16 mg/mL but no significant differences between CTRL and 16 mg/mL. In recent studies *S. epidermidis* was cultured on bulk Si_3N_4 and an initial enhancement of lipid bands was reported, followed by an intensity reduction at successive time points [42]. In that case the trend was supposed to arise from changes in the biophysical properties of membranes lipids during the bacteria adaptation to an external physiological stress. Again, this suggests that in the present study the bacteria in the 4 mg/mL group and 16 mg/mL group were probably engaged in different stages of a stress response.

The increase in local pH due to ammonia leaching from Si_3N_4 was formerly considered as a trigger for the deregulation of enzymes, such as peptidoglycan hydrolases, that are fundamental for cell wall integrity [42]. The anomalous activity of these enzymes causes an excessive degradation of peptidoglycans which results in a compromised cell wall, unable to maintain osmotic balance and leading the cell to a depolarized status prone to cell lysis [43]. Although high in-group variability was found in the analysis of the band related to NAG and NAM (constituents of the peptidoglycan), there was a significant decrease in the 16 mg/mL group compared to the CTRL group at 24h (Fig.33 **c**). This could be a distinctive feature of peptidoglycan degradation.

As a general remark to the spectroscopic investigation, it must be noted that a higher number of observations (spectra) for each treatment group would have allowed a more significant analysis and even the implementation of multivariate data analysis methods by which meaningful minor variations may have come to light.

4.4 Conclusion

Taking the first steps into the investigation of the antibacterial properties of Si_3N_4 powders, alterations in the Gram-positive bacteria *S. epidermidis* were analysed after its culture in BHI broth and BHI broth containing two different concentrations of Si_3N_4, for time up to 24 h. Microbial viability assays revealed that, among the tested values, the highest amount of dispersed powder caused a remarkably lower number of viable cells at all time points. A detailed comparison of selected Raman bands by means of intensity ratios shed light on the possible metabolic changes involved in the bacterial response. Raman bands related to DNA and RNA showed relevant decreases in the Si_3N_4-treated samples, in particular the stronger drop for RNA was attributed to the inhibition of transcription as part of a stress response. In agreement with the literature, significant alterations seen for bands related to cell wall polysaccharides, membrane lipids and peptidoglycan were interpreted as the result of cell wall degradation, osmotic imbalance and stress caused by local pH changes and ammonia penetration in the cells. Differences between the results obtained with the two concentration values supported the hypothesis that the ongoing biological activity is not identical in the two conditions and may correspond to different stages of the response. The Raman data was in agreement with the biological test, both suggesting that the presence of Si_3N_4 powder in the culture medium compromised cell growth up to a different degree depending on the powder concentration, with the value of 16 mg/mL causing the more dramatic changes. This amount of powder was therefore used in the experiments reported in the following sections.

5 The effect of Si_3N_4 powder on bacteria: pH

This chapter reports about a series of experiments whose focus was on the effect of pH on the interaction of silicon nitride powders with bacteria. Specifically five different pH conditions were investigated, with the following initial pH values at the onset of cell culture: pH 5.5, 6.5, 7.5, 8 and 8.5. For each pH value bacteria were allowed to proliferate with and without silicon nitride in their growth medium. Experiments were carried out analogously using one Gram-negative and one Gram-positive bacterial strain, with the aim of assessing if bacteria are affected differently on the basis of their cell wall structure.

5.1 Materials and methods

5.1.1 Bacterial culture

Bacteria were cultured in liquid at the Kyoto Prefectural University of Medicine using brain heart infusion (BHI) broth medium. The two bacterial strains, namely *S. epidermidis* (14990® ATCC™) and *P. gingivalis* (ATCC® 33227™), were initially cultured in BHI broth at 37°C for 24h and 96h respectively, then subcultured in fresh medium and ready for inoculation (details in Appendix A). In the case of *P. gingivalis*, which is anaerobe, the anaerobic condition was guaranteed by placing the culture tubes in a rectangular jar equipped with an oxygen absorber and CO_2 generator [13]. Alternative culture media were prepared by adding a selected amount of Si_3N_4 powder to obtain 0.5 vol% Si_3N_4 in BHI (16 mg/mL), these constitute treatment groups marked with "SN". BHI with no powder was used for the control groups (CTRL). The powder was sterilized by UV irradiation before addition to the culture medium, then suspended in the liquid before inoculation. The starting liquid had pH 7.5. Two sets of experiments were performed for each bacterial strain, one set with acidic pH conditions and the other with alkaline conditions. Considering the basic pH set, after withdrawing the required aliquotes for the preparation of sample with normal medium (pH 7.5), the starting liquid was added with tetraborate [14] to obtain pH 8. Aliquotes were withdrawn for the correspondent samples, then tetraborate was added again until reaching pH 8.5 and the last samples were prepared. An analogous procedure was followed for the acidic pH set, using phtalate [15] instead of tetraborate and obtaining the pH values 6.5 and 5.5.

After inoculation, *S. epidermidis* samples incubation took place at 37°C for two time-points: 0 h (meaning around 30 minutes) and 24 h. Whereas *P. gingivalis* was incubated at 37°C for 0 h (meaning less than one hour, around 30 minutes) and 72 h. All the samples were placed on a rotator which allowed constant agitation of the powder and prevented its deposition on the bottom of the culture vial.

5.1.2 Microbial viability assay

After the exposure times of 0 h, 24 h, and 72 h, bacterial metabolism was examined using the colorimetric assay WST-8 (Microbial Viability Assay Kit-WST, Dojindo, Kumamoto, Japan) as in the previous Chapter (Sec. 4.1.2). Four replicates were used to calculate mean values and standard deviations.

5.1.3 Raman spectroscopy

Raman spectra were collected after bacterial culture in BHI broth as well as BHI broth added with Si_3N_4 powder, at different initial pH values. The instrument, the selected parameters and the characterization

[13] AnaeroPack™ - Anaero, Mitsubishi Gas Chemical
[14] tetraborate pH standard solution, pH 9.18 (25°C), FUJIFILM Wako Pure Chemical Corporation
[15] phtalate pH standard solution, pH 4.01 (25°C), FUJIFILM Wako Pure Chemical Corporation

procedure were exactly the same as in Section 4.1.3.

5.2 Raman data analysis overview

The information contained in the Raman spectra of bacteria is very complex and difficult to extract, hence two strategies were planned for data analysis (Figure 34).

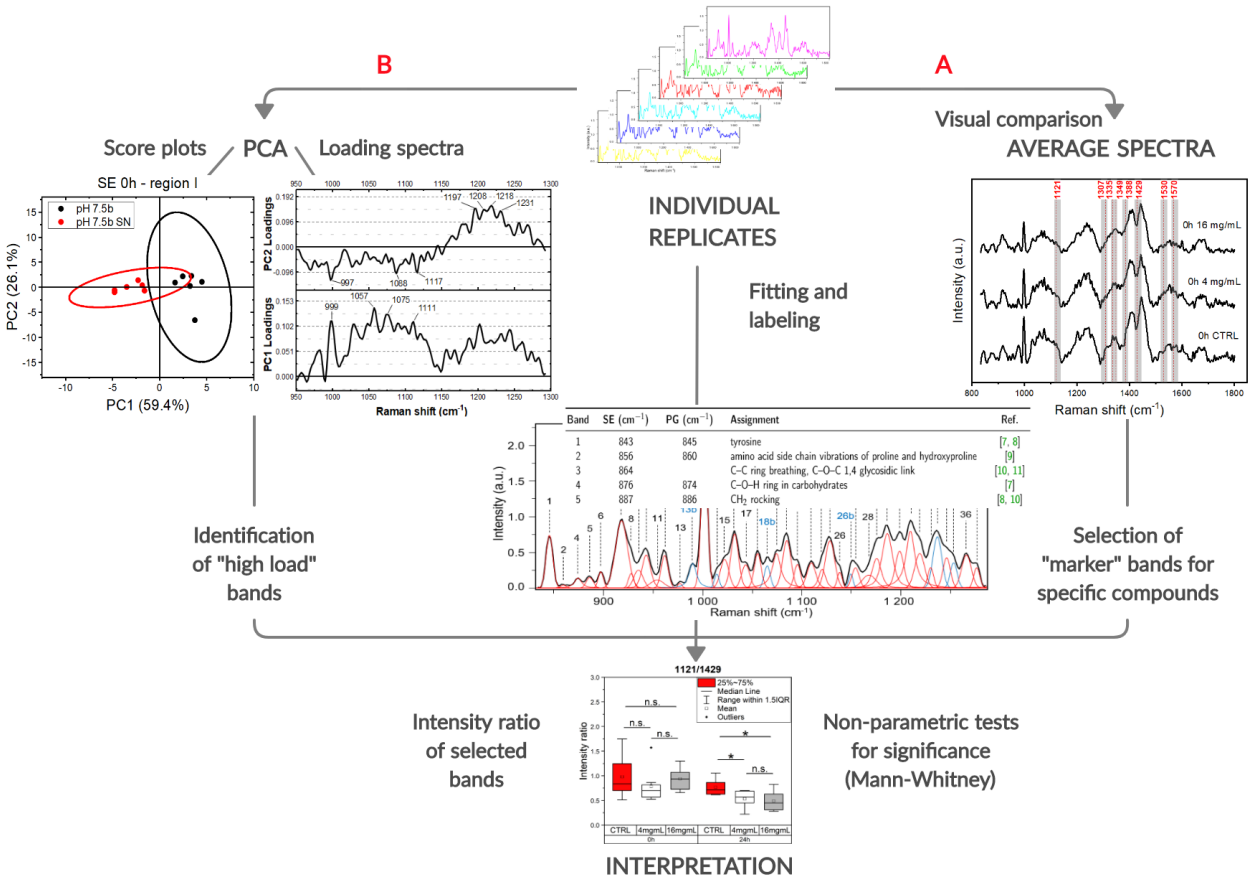

Figure 34: Strategy for the analysis of Raman spectra of bacteria. Starting from the pre-processed individual replicate spectra, two routes are sketched: route **A** exploits the visual comparison of average spectra to identify major changes between treatment groups and selected biologically relevant bands ("markers"); route **B** employs Principal Component Analysis (PCA) to find bands that are statistically relevant for spectral variance. Concurrently all the individual spectra are fitted and peak labeling and assignment are carried out. At this point intensity ratios of the bands selected along route **A** and **B** can be calculated in order to make specific comparisons among treatment groups.

A simple way of comparing different treatment groups is to calculate the average spectrum for each group and to visually check for differences, as it was done in the previous Chapter. In parallel the individual replicate spectra (6 for each group in the present study) can be fitted and the deconvoluted peaks can be assigned to specific molecular vibrations according to the literature. At this stage some bands that are biologically interesting and show apparent variations in the average spectra can be selected to perform intensity ratios in the individual spectra, then the results can be summarized in box-and-whiskers plots that allow to appreciate both in-group and between-group variations. Intensity ratios are useful for making comparisons as they are less affected by pre-processing methods and background

fluctuations [9]. This analysis route is indicated with the letter **A** in Figure 34, where another route is also sketched. The alternative route was planned because the selection of bands from the visual comparison of average spectra is rather subjective and subtle - yet important - differences may go unnoticed. Route **B** employs statistical methods to explore the data and give "loads" to the various spectral positions, guiding the selection of relevant bands and reducing arbitrariness. Path **B** is based on the multivariate data analysis technique called Principal Components Analysis (PCA) which allows to project a dataset with high number of variables (i.e. wavenumbers in spectroscopy) onto a smaller set of independent variables, called principal components (PCs), that are linear combinations of the original variables. These new variables represent the directions of maximal variation and usually the most relevant information is retained in the first few components [44, 45]. In this framework, 2D score plots display the projection of each object (i.e. each spectrum) in a plane defined by two PCs and are useful for identification of groups and exploration of patterns. Moreover the contribution of each original variable to each PC can be plotted in a loading "spectrum", which is helpful for the identification of important variables (bands) [46–48]. Bands selected through this procedure are then sent to the intensity ratio analysis and the results are used as a complement to the ones obtain from path **A**.

5.3 Results

5.3.1 Microbial viability assay

The results of the WST assay are reported in Figure 35. In all the analyzed cases the addition of Si_3N_4 powder ("16 mg/mL" in the graphs) caused a dramatic decrease in the metabolic activity of both bacterial strains w.r.t. the corresponding control groups (CTRL); numerically the absorbance value was always less than half of the CTRL one. An exception was found in the 0h acid pH set for *S. epidermidis*, where the absorbance in the CTRL groups was lower than in the "16 mg/mL" ones (Fig.35**b**). This unexpected outcome may be due to a systematic experimental error in the execution of the assay or some issues with the mother culture used for that batch of samples; in fact there is an otherwise unexplained inconsistency between the absorbance in the CTRL-0h-pH 7.5 group of the acidic set and the same group in the basic pH set (red ovals in Fig.35 **a**-**b**).

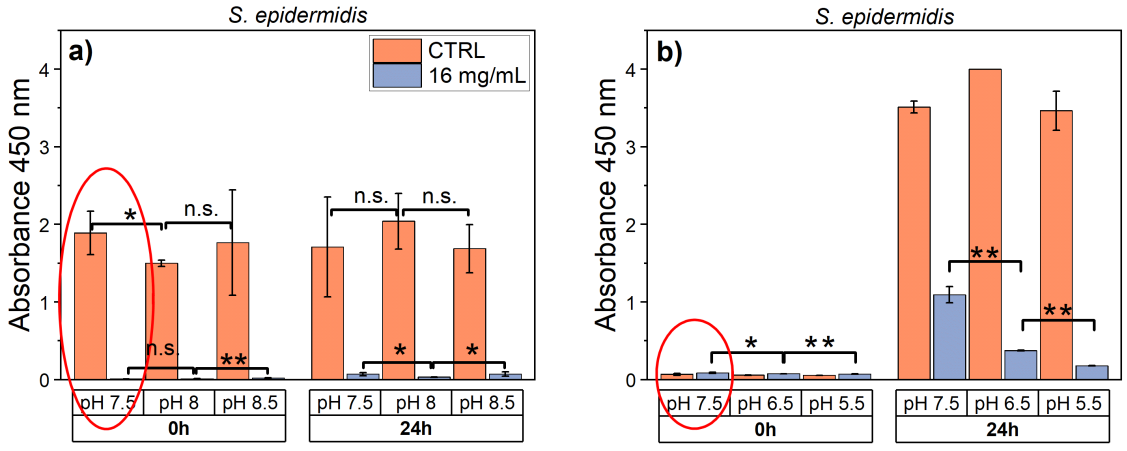

Figure 35: WST assay results. Cont.

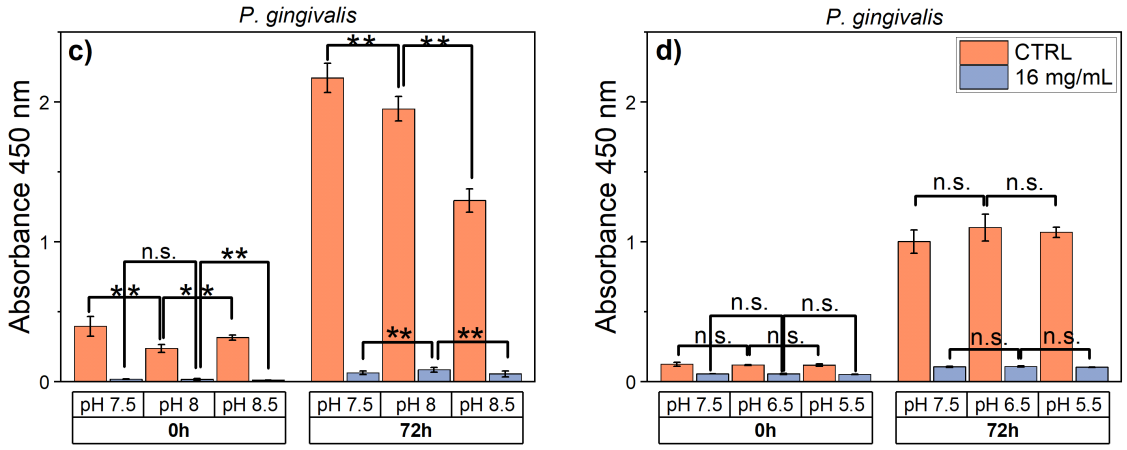

Figure 35: WST assay results. "CTRL" stands for samples cultured without Si_3N_4; "16 mg/mL" represents samples with 16 mg of Si_3N_4 powder per mL of BHI broth. Average absorbance measured at 450 nm. Error bars for SD. Statistical analysis performed by two-sample Student's t tests, with significance indicated as: $**$ for $p < 0.01$, $*$ for $p < 0.05$, *n. s.* for non-significant ($p > 0.05$). Basic pH set on the left column (**a**)(**c**), acidic pH set on the right (**b**)(**d**). The almost neutral pH-group (7.5) is shown on both sides since it was the normal BHI broth condition.

Another unclear observation is that in the basic pH set the absorbance level for *S. epidemidis* CTRL groups was the same at 0h and 24h, again probably deriving from culture-related issues. Still considering this strain, after 24h of culture no significant differences were found among the samples without Si_3N_4 (CTRL) neither in the basic pH set (Fig. 35**a**) nor in the acidic one (Fig. 35**b**). The same holds after 72h of culture of *P. gingivalis* in the acidic pH set (Fig. 35**d**), while for this strain there were evident differences in the basic pH set: for the CTRL groups the absorbance value significantly decreased with the increase of treatment pH from 7.5 to 8.5 (Fig. 35**c**). With the addition of Si_3N_4 in the culture medium, some trends emerged in the 0h datasets and were confirmed and more clearly defined after the prolonged treatments (24h or 72h). For *S. epidermidis* the absorbance value significantly decreased with the pH decrease from 7.5 to 5.5, whereas in the range 7.5-8.5 the lowest absorbance was scored by the group treated at pH 8. Conversely, group pH 8 had the highest absorbance values for *P. gingivalis* (compared to groups 7.5 and 8.5) and no differences were found in the acidic pH set in this case.

On account of the lower significance of the tests at 0h and the greater relevance of timing differences in the execution of the assay (of the order of 10 minutes on a 30 min culture period), it is reasonable to focus on the results of the prolonged experiments for subsequent analyses. In this regards, it must be noted that serial dilutions of the growth media were performed to obtain different pH conditions, resulting in different nutrient concentrations. Therefore a more rigorous comparison among treatment groups was made by taking the absorbance ratio between powder-treated and CTRL group for each pH condition (same pH, same nutrients) and then comparing the ratios. The outcome of the calculation is reported in Figure 36, here to higher y-values corresponds a lower effectiveness of the Si_3N_4 powder against the bacteria. For each bacterial strain, it is hard to compare acidic and basic pH set because the sets of experiments were made on different days and with different mother cultures, causing poor reproducibility of the assays as evidenced by the results for the samples cultured at pH 7.5 in the two occasions.

Notwithstanding, some important considerations can be made within each pH set. For *S. epidermidis* the worst conditions, i.e. when the efficiency of Si_3N_4 is highest, were pH 5.5 and pH 8. As for *P.*

gingivalis, instead, no significant differences can be highlighted in the acidic pH range while in the basic pH set Si_3N_4 seemed to have a greater impact at pH 7.5 compared to pH 8.

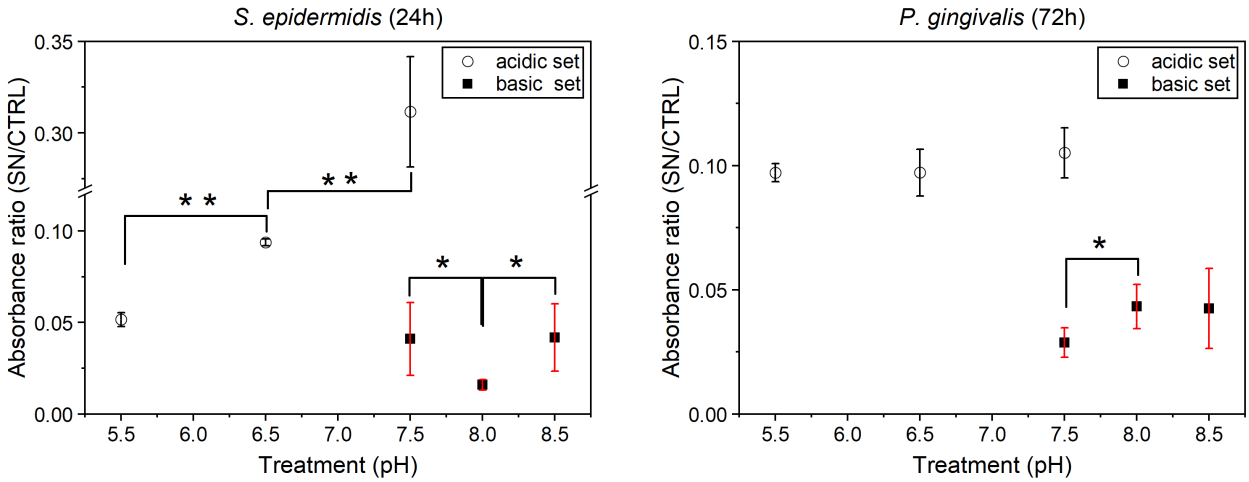

Figure 36: WST assay absorbance ratio. The Y axis reports the ratio of the mean absorbance value for the sample groups with silicon nitride (SN) over the mean value for the correspondent group without silicon nitride (CTRL). Error bars represent the uncertainty on the ratio, calculated considering the error propagation for a function of two independent variables, where the uncertainty of each variable is the standard deviation of the mean. Statistical analysis performed by two-sample Student's t tests, with significance indicated as: $**$ for $p < 0.01$, $*$ for $p < 0.05$, *n. s.* for non-significant ($p > 0.05$)

5.3.1.1 Summary

The effect of different pH on the antibacterial activity of Si_3N_4 was here investigated by analysing changes in viability through the WST-8 assay. As a common factor, the presence of Si_3N_4 powders in the culture media resulted in a clear decrease of metabolic activity compared to the CTRL groups (without Si_3N_4). With the pH variations some patterns were identified in the CTRL data, which however differ from the ones that emerged in the 16mg/mL data, suggesting that pH indeed affects the mechanism of action of Si_3N_4 against the microorganisms. The effects on viability were different for the two tested strains, in particular it is worth highlighting the following results:

- ***S. epidermidis***: 24h - major effects on viability in cultures with initial pH 5.5 and 8;
- ***P. gingivalis***: 72h - unvaried effects in the pH range 5.5-7.5, higher effects with pH 7.5 compared to pH 8.

5.3.2 Raman spectroscopy

5.3.2.1 Deconvolution and assignment

All the spectra were acquired in the spectral range 834 - 1800 cm^{-1} and subjected to pre-processing. The spectrum of the glass substrate was also acquired and showed a broad band centered at 916 cm^{-1}, consequently a peak normalization procedure was carried out for all the spectra with respect to the highest signal in the "glass region" (874 - 950 cm^{-1}) which was assumed to be a constant throughout all the experiments. Hence, this spectral region was not considered for making comparisons

among different treatment groups. Peak fitting was carried out for each spectrum, distinguishing two separate regions for clarity: region I (834 - 1290 cm^{-1}), region II (1290 - 1800 cm^{-1}). An example of fitted spectrum for *S. epidermidis*, with the correspondent assignments, was reported in the previous Chapter. The example spectra for *P. gingivalis* are displayed in Figure 37 and Figure 38 for the first and second spectral range, respectively. For convenience, band numbering was kept the same as for the *S. epidermidis* case and newly found bands have been added the suffix "b" and are shown in blue. The vibrational modes for each individual band were assigned according to their physical origin trying to specify, when applicable, the cellular compounds in which they originate.

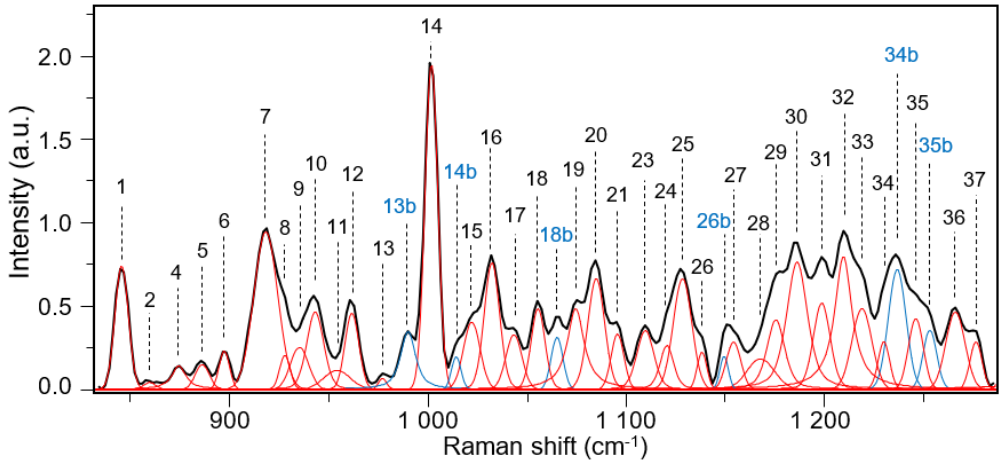

Figure 37: Normalized deconvoluted Raman spectrum in region I (*P. gingivalis*, pH 7.5 0h).

The proposed assignments are listed in Table VIII and Table IX, where Raman shifts are reported in the columns named SE and PG (short for *S. epidermidis* and *P. gingivalis* respectively).

Table VIII: Band labeling, tentative assignment and related references for Raman peaks in region I

Band	SE (cm^{-1})	PG (cm^{-1})	Assignment	Ref.
1	843	845	tyrosine	[2, 3]
2	856	860	amino acid side chain vibrations of proline and hydroxyproline	[10]
3	864		C–C ring breathing, C–O–C 1,4 glycosidic link	[11, 12]
4	876	874	C–O–H ring in carbohydrates	[2]
5	887	886	CH_2 rocking	[3, 11]
6	898	897	C–O–C in plane symmetric ring deformation	[11]
7	910	918	C–O, C–C stretching in ribose	[7, 13]
8	921	928	proline	[3, 14]
9	935	935	C–C backbone stretching in proteins (α helix), C–O–H glycosidic in carbohydrates	[2, 12]
10	944	943	CH_2 rocking in membrane lipids	[12]
11	959	954	CH_3 (terminal) rocking	[11]
12	973	962	CH_3 rocking, CCH bending in proteins; ribose	[7, 15]
13	981	977	C–C in proteins (β sheet), =CH bend in lipids	[2]
13b		990	carbohydrates peak for solutions	[8]
14	998	1002	symmetric ring breathing phenylalanine	[2, 3]
14b		1014	carbohydrates peak for solutions	[8]
15	1020	1022		
16	1031	1032	C–H in plane phenylalanine	[2, 3]

Table VIII: (continued)

Band	SE (cm^{-1})	PG (cm^{-1})	Assignment	Ref.
17	1046	1043	C–C aromatic ring	[12]
18	1059	1055	*trans* C–C stretching in lipids	[4, 5]
18b		1065	*trans* C–C stretching in lipids; C–O, C–C stretching in carbohydrates	[2, 4, 5]
19	1073	1074	chain C–C stretching in lipids; C–O, C–C stretching in carbohydrates	[2, 6]
20	1082	1085	*gauche* C–C stretching in lipids	[4]
21	1092	1096	PO_2^- stretching in nucleic acids, C–C stretching in lipids	[2, 4, 7]
22	1103		carbohydrates	[14]
23	1111	1110	C–O, C–C in carbohydrates	[6]
24	1121	1120	C–O stretching in carbohydrates (ribose marker)	[2, 8]
25	1129	1128	C–C in lipids; C–N stretching in proteins	[2, 16]
26	1140	1138	adenine ring breathing mode	[3, 17]
26b		1149	C–N and C–C stretching in carbohydrates or in lipids	[49]
27	1156	1154	C–C stretching in carotenoids	[6, 11]
28	1169	1168	C–H of tyrosine	[2, 6, 18]
29	1179	1175	tyrosine, phenylalanine, amide III	[6, 12]
30	1187	1186	cytosine, guanine, adenine	[5, 19]
31	1200	1199	hydroxyproline, tyrosine	[3, 5]
32	1210	1210	C–C_6H_5 in phenylalanine and tryptophan	[2, 20]
33	1220	1219	C–N stretching	[18]
34	1231	1230	amide III (β sheets); =CH in lipids	[2, 9]
34b		1237		
35	1246	1246	amide III (random structures); =CH in lipids	[2, 9]
35b		1253		
36, 37	1264, 1280	1264, 1276	amide III (α helices); =CH in lipids	[2, 9]
37b		1291		

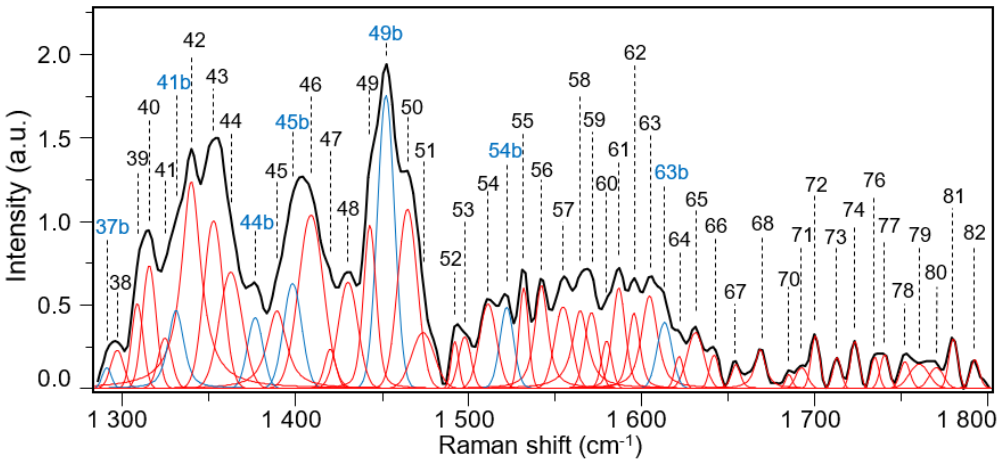

Figure 38: Normalized deconvoluted Raman spectrum in region II (*P. gingivalis*, pH 7.5 0h).

Table IX: Band labeling, tentative assignment and related references for Raman peaks in region II.

Band	SE (cm^{-1})	PG (cm^{-1})	Assignment	Ref.
38	1297	1297	CH_2 deformation, CH_2 twist in lipids	[2, 16]
39, 40	1307, 1313	1309, 1316	CH_2 rocking, CH_2 twist in lipids (membrane lipids)	[4, 6, 12]
41	1322	1325	in plane CH_2 deformation	[11]
41b		1331	NH_2 stretching in adenine and polyadenine	[49, 50]
42	1335	1340	OH deformation in polysaccharides, tryptophan	[3, 8, 9, 12]
43	1349	1353	adenine and guanine, CH deformation in proteins	[2]
44	1369	1363	T, A, G (ring breathing modes of the DNA/RNA bases)	[18]
44b		1377	CH_3 symmetric stretching in lipids	[15]
45	1388	1389	CH_3 symmetrical deformation (NAG, NAM)	[11]
45b		1398	CH_3 bend in lipids; COO^- symmetric stretching	[6]
46	1405	1409	CO_2^- stretching in α-amino acids	[3, 12]
47	1419	1420	CH_3 asymmetrical deformation	[11]
48	1429	1430	CH_2 deformation (deoxyribose)	[9, 19]
49	1446	1443	CH_2 scissoring (fatty acids, phospholipids, proteins, saccharides)	[11, 12, 21]
49b		1452		
50	1463	1465	CH_2 deformation (carbohydrates, lipids, proteins)	[2, 24]
51-53	1477-1501	1474-1498	CH_2 deformation	[2, 12]
54	1516	1511	C=C stretching in carotenoids	[3, 6, 11, 14]
54b		1522		
55, 56	1527, 1545	1532, 1542	amide II, N-acetyl-related bands (amide II)	[12]
57-59	1556-1571	1555-1571	NH deformation and CN stretching in amide II	[11, 12]
60	1580	1580	guanine and adenine ring stretching	[2, 16]
61, 62	1590, 1597	1587, 1595	C=C in phenylalanine	[2, 6, 14, 16]
63	1608	1604	C=C in phenylalanine and tyrosine	[2]
63b		1613	C=C in tyrosine and tryptophan	[2, 5, 16]
64	1620	1622	C=C in tyrosine and tryptophan	[2, 3, 12]
65	1637	1631	C=O stretching in amide I (β sheets)	[3, 9, 14]
66-71	1644-1692	1642-1692	C=O stretching in amide I, C=C stretch in lipids (unsaturated fatty acids)	[2, 3, 12]
72, 73	1703, 1710	1700, 1713	C=O stretching in lipids	[22]
74-80	1720-1771	1723-1770	C=O ester stretching in lipids	[2, 3, 6, 12]
81, 82	1782, 1792	1780, 1792	C=O stretching in lipids	[9, 23]

NAG: N-acetylglucosamine; NAM: N-acetylmuramic acid

Here the bands that were designated as markers in the preliminary study (Chapter 4) are briefly recalled: 1120-1121 cm^{-1} (Band 24) for ribose in RNA, 1307-1316 cm^{-1} (Bands 39, 40) for membrane lipids, 1335-1340 cm^{-1} (Band 42) for polysaccharides, 1349-1453 cm^{-1} (Band 43) for adenine and guanine, 1388-1389 cm^{-1} (Band 45) for NAG and NAM, 1429-1430 cm^{-1} (Band 48) for deoxyribose in DNA, 1527-1571 cm^{-1} (Bands 55-59) for amide II in proteins. These bands were monitored again in this phase of the study, however other bands were selected in case these ones did not show relevant variations among the samples.

5.3.2.2 Visual comparison of average spectra

Due to the dilution of growth media to obtain more acidic or more alkaline pH, bacteria experienced different nutrient concentrations in the different pH groups, therefore a direct comparison is only possible between groups that were cultured with the same initial pH. This means that the spectra were compared pair by pair, where each pair was composed by groups between which the only difference was the presence or absence of silicon nitride in the medium: CTRL vs SN. To ease the visual detection of variations in the

spectral profiles the difference between the average spectrum of the CTRL group and the correspondent SN group average spectrum was calculated and plotted together with the two spectra. The results for *S. epidermidis* are presented in Fig.39a for the acidic pH set and Fig.39b for the basic pH set.

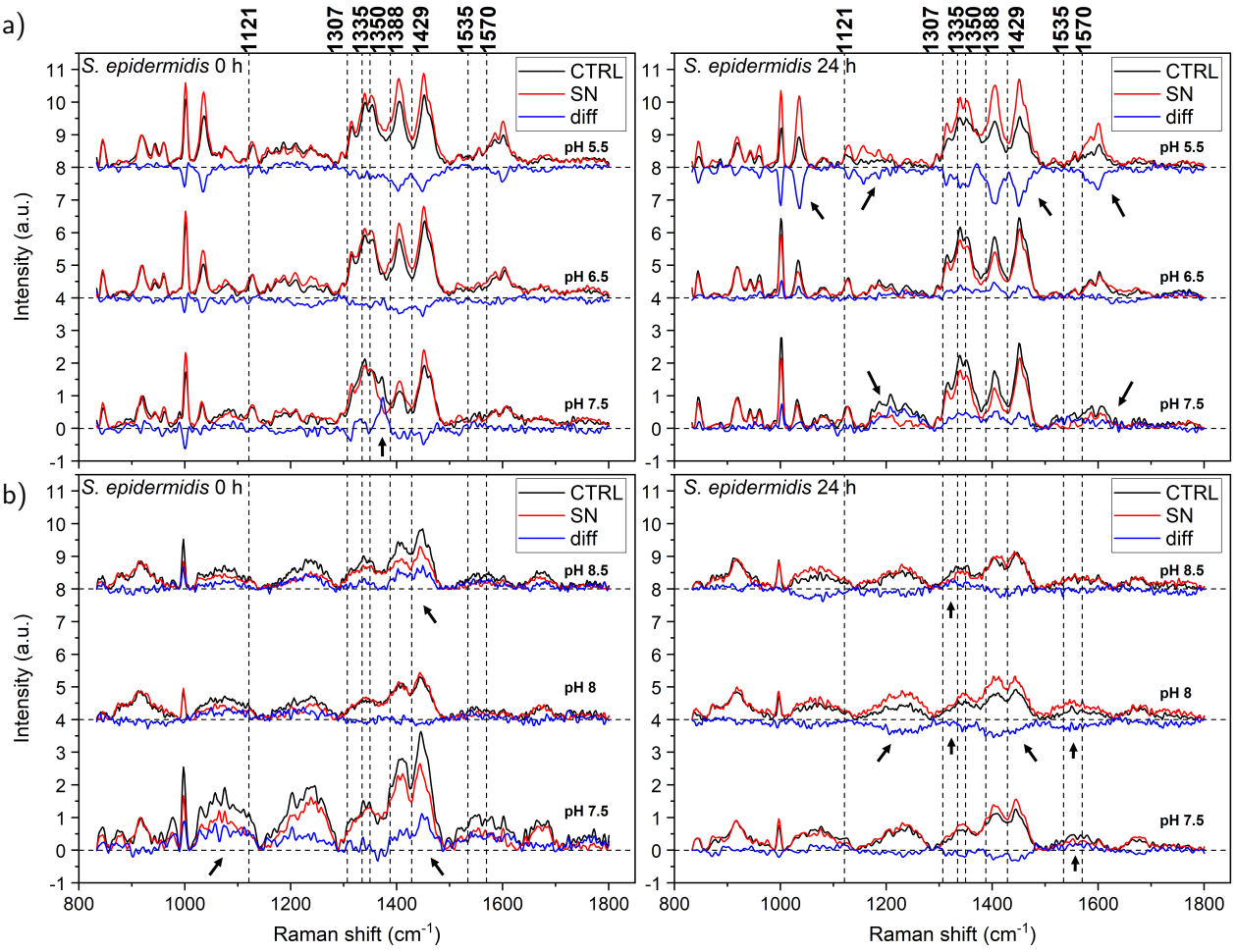

Figure 39: Average Raman spectra of *S. epidermidis* after pH treatments: left column 0h culture (up to 30 min), right column 24h culture. (a) acidic pH set, (b) basic pH set. SN stands for 16 mg/mL silicon nitride powder in the growth medium, CTRL is without it; "diff"= CTRL - SN. Vertical dashed lines correspond to the bands of interest that were selected in the preliminary study. Arrows point at regions with evident changes.

Considering the acidic pH groups treated for up to 30 min (0h) the difference between CTRL and SN spectra is very similar for initial pH 5.5 and 6.5, where the SN spectra have more intense features in the region from 1300 to 1490 cm^{-1} which comprises mainly CH_2 deformation modes from all cellular components but also includes some of the previously identified marker bands. This is also observable in the pH group 7.5, except for the bands around 1320-1331 cm^{-1} and 1360-1385 cm^{-1} which show an opposite behavior (arrow in the figure). The latter wavenumber range contains an interesting band related to nitrogenous bases (Band 44). Groups 6.5 and 5.5 also show an increase in the phenylalanine mode at $\sim$ 1034 cm^{-1} (Band 16). The situation changes with the 24h treatments: here for the more acidic pH condition there is a further increase in intensity for the SN sample with respect to the CTRL

one, now also localized in the ranges 1120-1200 cm^{-1} and 1570-1610 cm^{-1}. Conversely, for groups 7.5 and 6.5 there is a trend inversion in these spectral regions, with the CTRL spectra displaying higher (or equal) intensities compared to the respective SN spectra.
As regarding the basic pH set, at 0h in all the pairs the CTRL spectra present some bands with higher intensity with respect to their SN correspondent, particularly around 1015-1130 cm^{-1} and 1385-1490 cm^{-1}. Even in this case some trend inversions appear in the 24h-treated groups: here the intensities in such regions rise up for the SN spectra at pH 7.5 and 8, but remain almost equal to the CTRL spectrum in the pH group 8.5. A difference between group 7.5 and 8 is found for amide II bands, between 1530 and 1570 cm^{-1}, that show opposite trends in the two pairs. An analogous variation can be observed in the range 1300-1335 cm^{-1} when comparing pH group 8 with 8.5.

The results for *P. gingivalis* are presented in Fig.40a and Fig.40b for the acidic and basic pH sets respectively.

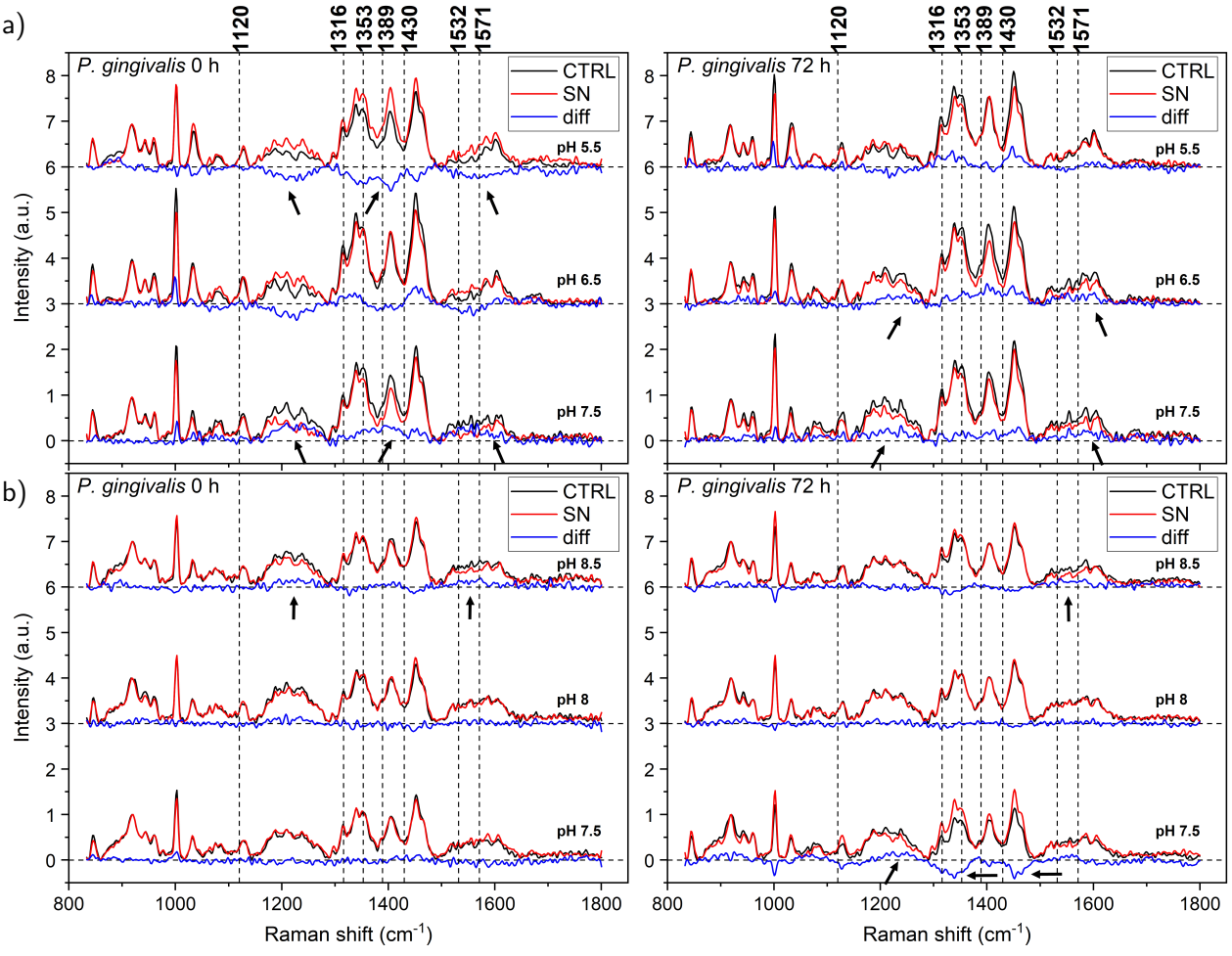

Figure 40: Average Raman spectra of *P. gingivalis* after pH treatments: left column 0h culture (up to 30 min), right column 72h culture. **a)** acidic pH set, **b)** basic pH set. SN stands for 16 mg/mL silicon nitride powder in the growth medium, CTRL is without it; "diff"= CTRL - SN. Vertical dashed lines correspond to the bands of interest that were identified in the preliminary study. Arrows point at regions with evident changes.

Starting from the acidic pH treatments, 0h culture, the three pairs display very different behaviours: on the one hand in group 5.5 the SN spectrum has more intense features compared to the CTRL one, on the other hand in group 7.5 the CTRL spectrum predominates in intensity; lastly in group 6.5 the trend is alternating. The differences between the pairs seem to level off in the 72h scenario: in this case the CTRL spectrum exhibits more intense features in all the pairs. Switching to the basic pH set, both in the 0h and 72h case the spectra in each pair are strikingly similar. Minor differences could be found in pH group 8.5, where at both time-points the CTRL spectrum shows more intense bands in the amide II region (1530-1570 cm^{-1}) compared to the SN. Finally in group 7.5, 72h, the SN spectrum exhibits more intense features in the ranges 1300-1370 cm^{-1} and 1440-1475 cm^{-1}, which mostly cover CH_2 deformation vibrations but also include some of the marker bands that can be related to more specific cellular components.

Based on such visual comparisons, the bands selected for subsequent analysis were the following:

- region I: bands 16, 21, 24, 30, 32;
- region II: bands 39-40, 42, 43, 44, 45, 48, 49-49b, 55, 59.

5.3.2.3 Principal Component Analysis

For each pair of samples PCA was first performed on the spectral range from 950 to 1800 cm^{-1}, to avoid the previously identified glass signal region. Then it was performed on two sub-intervals, i.e. region I from 950 to 1290 cm^{-1} and region II from 1290 to 1800 cm^{-1}. Regarding the number of principal components (PCs) to be kept for proceeding with the inspection of the loadings a decision method was applied: to set a cutoff percentage of the variance that must be accounted for by a designated number of components [51]. Specifically the pre-set threshold value was 70 % of variance to be explained by the first two PCs. For the purposes of this study and taking into account the very limited number of spectra for each sample pair, it was considered not advantageous to proceed with the analyses when the criterion was not met, therefore in such cases the analysis was aborted. In the event that in both region I and region II the % had a favourable value, then only the region with the higher value was analyzed. For each pair of samples the evaluation of the PCA output is summarized in Tables X-XI, for *S. epidermidis* (SE) and *P. gingivalis* (PG) respectively: here for conciseness only the interval with the higher percentage of variance explained by PC1 and PC2 is reported and percentages below the cutoff value are indicated in red. "pH 7.5a" stands for the experiments performed at initial pH = 7.5 in the acidic pH set, "pH 7.5b" for the basic pH set.

Table X: PCA explained variance - SE

Sample pair	Spectral region	% variance PC1+PC2
SE pH 5.5 0h	II	73
SE pH 6.5 0h	II	77
SE pH 7.5a 0h	II	69
SE pH 7.5b 0h	I	85
SE pH 8 0h	I	79
SE pH 8.5 0h	I	77
SE pH 5.5 24h	II	81
SE pH 6.5 24h	II	72
SE pH 7.5a 24h	I	76
SE pH 7.5b 24h	I	86
SE pH 8 24h	I	65
SE pH 8.5 24h	I	83

Table XI: PCA explained variance - PG

Sample pair	Spectral region	% variance PC1+PC2
PG pH 5.5 0h	II	78
PG pH 6.5 0h	I	76
PG pH 7.5a 0h	I	66
PG pH 7.5b 0h	II	53
PG pH 8 0h	II	54
PG pH 8.5 0h	II	55
PG pH 5.5 72h	II	65
PG pH 6.5 72h	II	80
PG pH 7.5a 72h	II	64
PG pH 7.5b 72h	II	73
PG pH 8 72h	I	60
PG pH 8.5 72h	II	62

Among the 24 sample pairs, a total of 10 pairs were discarded so that 14 pairs were accepted for further analysis, specifically 7 pairs for spectral region I and other 7 pairs for spectral region II.

Typical PCA output graphs are displayed in Figure 41 for the sample pair SE pH 7.5b 0h. In this example PC1 describes 59.4% of the observed variance and PC2 26.1%. It can be appreciated from the 2D score plot (Fig.41a) that, although there is a superposition of the 95% confidence ellipses, the two treatment groups are quite distinguished in the plane formed by the first two PCs: along PC1 the evaluated spectra of the CTRL group have only positive scores whereas those pertaining to the respective SN group have only negative scores. Within-group variability is also evident and together with the small number of replicates it constitutes a limiting factor for the separation of the different groups of spectra, which appears to be even less clear for other sample pairs. Moving to the loadings of the first two principal components (Fig.41b) the spectral positions with high relative loads were marked in the plots by indicating the correspondent wavenumber. According to the assignments proposed in Section 5.3.2.1 the involved bands were: Band 14 at 999 cm^{-1} (phenylalanine), Band 18 at 1057 cm^{-1} (lipids), Band 19 at 1075 cm^{-1} (lipids and carbohydrates), Band 20 at 1088 cm^{-1} (lipids), Band 23 at 1111 cm^{-1} (carbohydrates), Band 24 at 1117 cm^{-1} (carbohydrates, ribose), Band 31 at 1197 cm^{-1} (hydroxyproline, tyrosine), Band 32 at 1208 cm^{-1} (phenylalanine, tryptophan), Band 33 at 1218 cm^{-1} (C–N stretching, no specific biomolecule), Band 34 at 1231 cm^{-1} (amide III, lipids).

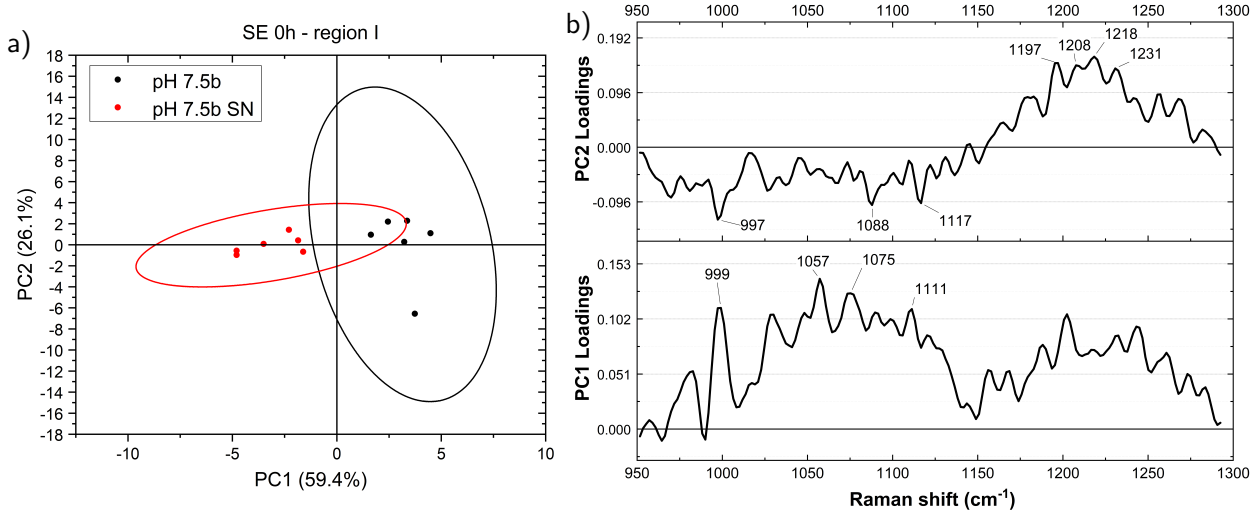

Figure 41: Example of PCA output for *S. epidermidis*: treatment group pH 7.5 (alkaline set of experiments), 0h culture, spectral region I. **a)** score plot for the first two PCs with 95% confidence ellipses, **b)** loading spectra of PC1 and PC2.

Analogous observations were carried out for all the sample pairs that satisfied the criterion. Since the identified bands were numerous a simple survey was conducted to determine how frequently such bands appeared with high loading among the successful sample pairs. For each band a relative occurrence frequency (%) was calculated by taking the ratio between the number of sample pairs in which the band was found at high load and the total number of successful sample pairs in that spectral region. For example, considering spectral region I, Band 22 emerged in the loadings of only 1 sample pair out of 7 successful pairs, resulting in an occurrence frequency of 14.3%. The results are summarized in Tables XII and XIII for the two spectral ranges, here the bands with occurrence frequency higher than 70% were highlighted in green.

Table XII: High load band selection - region I

Band n.	Raman shift (cm^{-1})	Occurrence frequency %
11	954-959	28.6
14	1000	71.4
16	1031	28.6
17	1043-1046	14.3
18, 18b	1055-1065	71.4
19	1073	28.6
20	1082-1088	57.1
21	1092-1096	28.6
22	1103	14.3
23	1110	42.9
24	1121	57.1
25	1129	28.6
27	1155	14.3
30	1187	28.6
31	1200	85.7
32	1210	57.1
33	1220	85.7
34	1230	100.0
34b	1234-1240	57.1
35	1246	71.4
35b	1253	14.3
36	1264	71.4
37	1276-1280	42.9
37b	1291	42.9

Table XIII: High load band selection - region II

Band n.	Raman shift (cm^{-1})	Occurrence frequency %
38-39	1297-1310	28.6
40	1313-1316	42.9
41, 41b	1321-1331	28.6
42	1335-1340	100.0
43	1349-1353	71.4
44	1363-1369	42.9
45, 45b	1388-1398	85.7
46	1402-1409	85.7
47	1420	28.6
48	1430	28.6
49, 49b	1443-1452	100.0
50	1465	71.4
51-53	1477-1501	28.6
54b	1522	14.3
55	1530	28.6
56	1545	28.6
57-59	1555-1571	71.4
62	1597	28.6
63b	1613	28.6
64	1620	14.3
65	1631-1637	28.6
66-71	1644-1692	57.1
72	1700	14.3
74-80	1720-1771	28.6

The following bands were finally used to calculate intensity ratios:

- region I: bands 14, 18-18b, 31, 33, 34, 35, 36;
- region II: bands 42, 43, 45-45b, 46, 49-49b, 50, 57-59.

5.3.2.4 Intensity ratios analysis

In accordance with the procedure employed in the previous Chapter (Section 4.2.2) intensity ratios were again calculated with respect to Band 49, the intense signal at $\sim$ 1446 cm^{-1} which arises from CH_2 scissoring from basically all cellular components and is used as internal reference. The selection of bands from pathway A and B led to a total of 22 distinct bands and considering that for each band there are two pH sets, two time points and two bacterial strains, it gives a number of cases equal to 176, to which corresponded an equivalent number of graphs (box-and-whiskers plots) displaying the ratio of the specific band over Band 49 for each sample. Statistical tests were performed pairwise, trying to assess variations between control and treatment samples belonging to the same group in terms of pH and time, i.e. control = CTRL = grown without silicon nitride vs. treatment = SN = grown with silicon nitride. One-sided Mann-Whitney tests were employed because of the small sample size involved and for the presence of outliers; significance was expressed as: $**$ for $p < 0.01$, $*$ for $p < 0.05$. Evidently the number of produced outputs (176 graphs) was too high to be displayed effectively and to allow a meaningful interpretation, therefore a further and more stringent selection was performed on the basis of the statistical significance obtained in the tests and ensuring to report for each bacterial strain at least one band for each cellular component, namely: proteins, carbohydrates, lipids and nucleic acids.

Starting from *S. epidermidis* - "SE" henceforth - two bands related to proteins were chosen: Band 16, which was assigned to Phenylalanine, and Band 59, assigned to amide II vibrations. The intensity ratios with Band 49 are presented in Fig.42. The relative intensity of Band 16 was more significantly affected by silicon nitride in the alkaline pH conditions, in particular the intensity was lower in the SN samples at pH 7.5 (0h, 24h) and 8 (0h) but the opposite was true for the samples treated at pH 8.5 (24h). Considering the acidic pH set the only significant difference was found in the pair treated at pH 6.5 (24h), where the band was less intense (w.r.t. Band 49) in the SN sample compared to its CTRL sample.

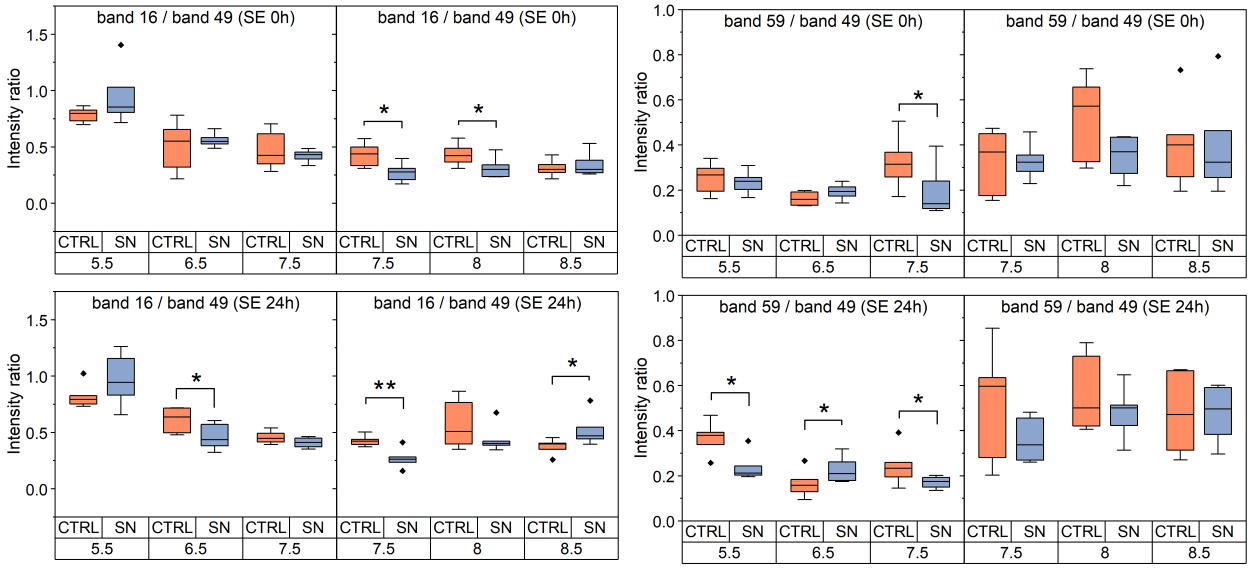

Figure 42: Intensity ratios for protein-related Raman bands (SE): Band 16 corresponds to Phenylalanine, Band 59 to amide II groups. Filled box: 25%-75% of the data with median line displayed; error bars represent the range within 1.5 interquartile range (IQR); black points indicate outliers.

Conversely, Band 59 displayed significant between-group variability in the acidic pH set and no significant differences in the alkaline set, probably due to the very high in-group variability found in the latter dataset; the treatment at pH 5.5 resulted in a behavior analogous to the normal BHI (pH 7.5), having the lower relative intensity in the SN sample, whereas for the pair at pH 6.5 (24h) the relative intensity of Band 59 was lower in the CTRL sample. Thus the effect of silicon nitride was apparently opposite for the bacteria grown at initial pH 5.5 and 6.5.

For carbohydrates and lipids the selected bands were Band 42 (OH deformation in polysaccharides) and Band 39 (CH_2 rocking and CH_2 twist in lipids), the results are in Fig.43. Both components displayed a decrease in relative intensity in the SN sample vs the CTRL one when looking at the acidic pH conditions. In the treatment group at pH 8 0h, instead, the intensity in the SN sample was significantly higher than in the CTRL; the trend is reverted for band 39 after 24h of culture (pH 8).

The last two reported bands are Band 21 (PO_2^- stretching) for nucleic acids (NAs) and Band 45 related to cell wall components (CH_3 deformation in NAG and NAM), whose ratios with Band 49 can be appreciated in Fig.44. The relative intensity of Band 21 was lower in the SN sample in almost every pH group except for the treatment at pH 8.5 for 24h, in which the presence of Si_3N_4 caused a significant intensity increase in this band w.r.t. the CTRL sample. Band 45 was less intense in the SN sample at pH 5.5 (0h, 24h) but no significant differences emerged in the other pairs of the acidic dataset. In

the alkaline set the only significant difference was found for pH 8 (0h), with a less intense signal in the CTRL sample compared to the correspondent SN sample.

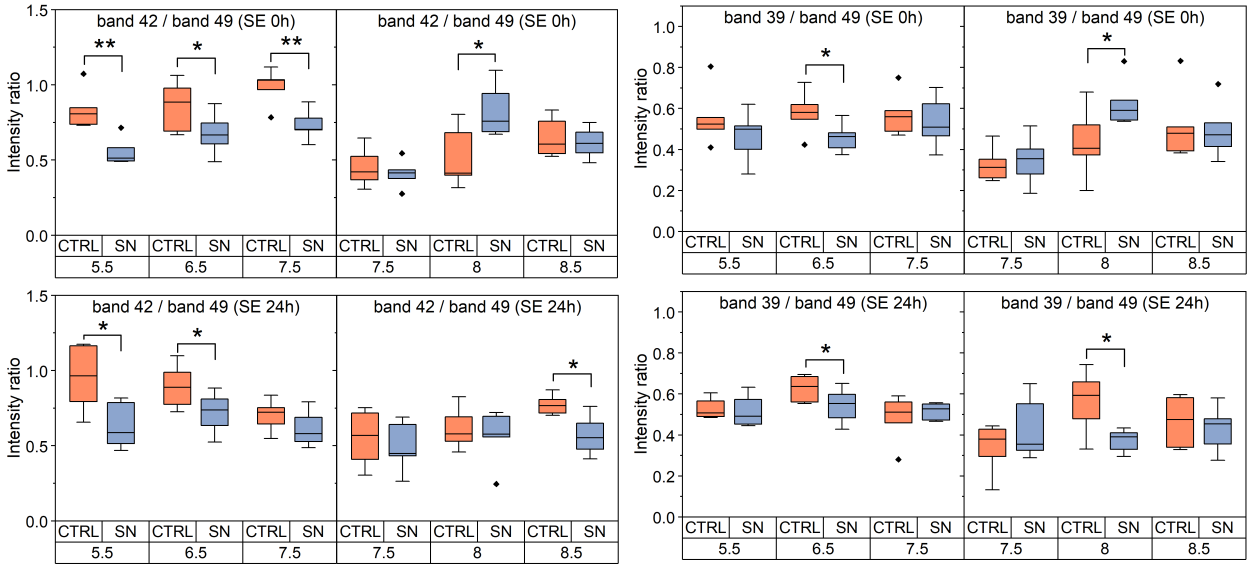

Figure 43: Intensity ratios for carbohydrate- and lipid-related Raman bands (SE): Band 42 corresponds to OH deformation in polysaccharides and Band 39 to CH_2 rocking and CH_2 twist in lipids.

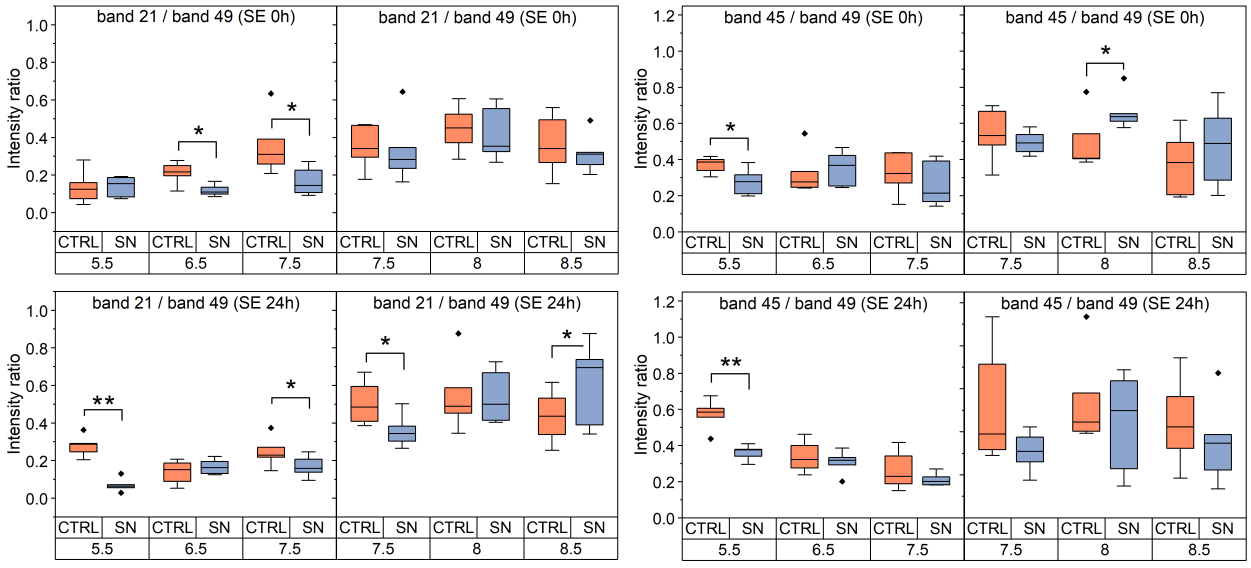

Figure 44: Intensity ratios for Raman bands related to NAs and cell wall (SE): Band 21 corresponds to PO_2^- stretching and Band 45 to CH_3 deformation in NAG and NAM.

For NA-related signals, the trend of Band 48 (CH_2 deformation in deoxyribose) over Band 49 with the varying pH conditions displayed a striking similarity with the results for Band 21, confirming the aforestated observations. The graphs related to Band 48 can be found in the Appendix (Fig.A.1).

On account of the different significance found in the statistical tests performed on data from *P. gingivalis* (PG) Raman spectra, an alternative set of bands was selected for the same cellular components investigated for SE: Band 14 (Phenylalanine) and Band 36 (amide III signals) for proteins, Band 18-18b for carbohydrates (C–O, C–C stretching in carbohydrates), Band 35 for lipids (=CH in lipids), Band 30 for nucleic acids (nitrogenous bases C, G, A) and Band 45 related to cell wall components (CH_3 deformation in NAG and NAM).

The intensity ratios of protein-related peaks with Band 49 are reported in Fig.45. In the acidic pH conditions the two selected bands were affected in a contrasting way by the presence of silicon nitride: on the one hand the Phenylalanine peak was less intense in the SN samples (pH 7.5 0h, pH 5.5 72h) and the behavior was similar among the three pH conditions, on the other hand the amide III signal had lower relative intensity in the CTRL samples (pH 6.5 0h, pH 5.5 0h and 72h) and the effect was significantly different comparing the truly acidic pH groups with the normal BHI (pH 7.5). In the alkaline pH set the only feature standing out was the higher contribution of both bands in the CTRL samples grown at pH 8 for 30 min (0h); the trend was however reverted after 72h of culture.

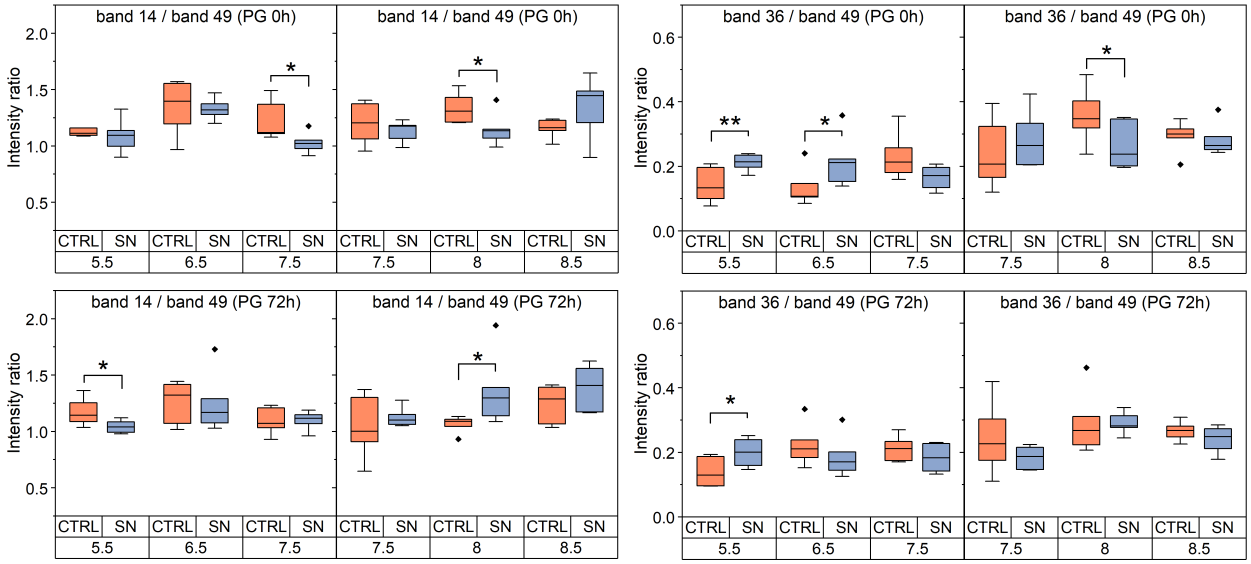

Figure 45: Intensity ratios for protein-related Raman bands (PG): Band 14 corresponds to Phenylalanine, Band 36 to amide III groups. Filled box: 25%-75% of the data with median line displayed; error bars represent the range within 1.5 interquartile range (IQR); black points indicate outliers.

Considering the peak related to carbohydrates (Fig.46 - left, Band 18) the intensity ratio was significantly higher when Si_3N_4 was present in the medium at pH 5.5 (0h), whereas for pH 6.5 (72h) and 7.5 (0h, 72h) the ratio was higher in the CTRL sample. Once again in the basic pH dataset the treatment at pH 8 resulted in opposite effects compared to the other two conditions (pH 7.5 and pH 8.5). For what concerns the lipid-related band (Fig.46 - right, Band 35), the results were strikingly different at 0h and 72h, with opposite trends appearing in both the acidic and the basic pH groups. Specifically the band was relatively more intense in the SN sample at pH 6.5 after 30 min but after 72h it became higher in the CTRL sample. Although the same happened in the basic set at pH 7.5, it can be noted that this specific pH condition, corresponding to normal BHI, displayed an opposite effect in the acidic dataset at 0h, thus the reliability of the result at 0h is controversial.

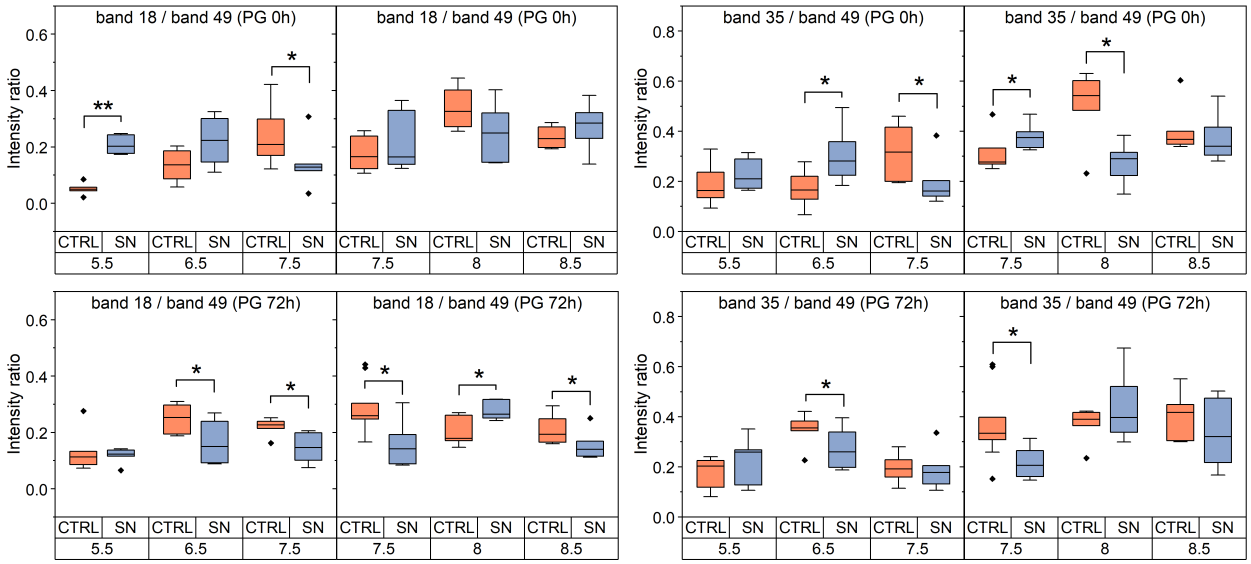

Figure 46: Intensity ratios for carbohydrate- and lipid-related Raman bands (PG): Band 18 corresponds to C–O, C–C stretching in carbohydrates while Band 35 to =CH in lipids.

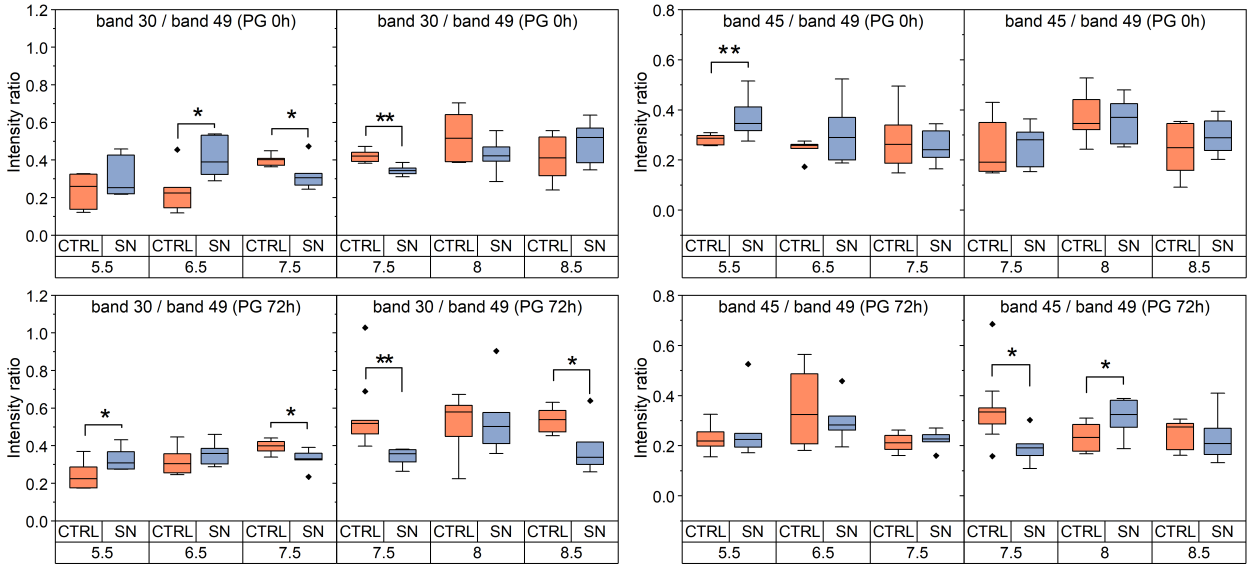

Figure 47: Intensity ratios for Raman bands related to NAs and cell wall (PG): Band 30 corresponds to vibrations from the nitrogenous bases C, G and A, while Band 45 to CH_3 deformation in NAG and NAM.

The last comparison involved the signals ascribed to NAs and cell wall components (Fig.47). The ratio Band 30 / Band 49 was significantly higher in the CTRL samples at pH 7.5 (both in acidic and alkaline datasets, 0h and 72h). The same hold for the treatment at pH 8.5 for 72h. At pH 6.5 (0h) and 5.5 (72h), in contrast, the ratio was higher in the SN samples. Band 45 was relatively more intense in the SN sample when bacteria were treated at pH 8 for 72h, while less intense in the SN sample when unmodified BHI broth was used (pH 7.5, 72h); the only significant difference in the acidic pH set was found in the sample pair at pH 5.5 (0h), where the ratio was higher in presence of silicon nitride.

5.3.2.5 Summary

The effect of different pH conditions on the antibacterial activity of Si_3N_4 was here investigated by analysing changes in the Raman spectra of *S. epidermidis* (SE) and *P. gingivalis* (PG) after 30 min (0h) and 24h (72h for PG) of culture. Two pathways were followed for the selection of relevant Raman bands and culminated in the calculation of intensity ratios for those peaks that were both statistically and biologically significant. In many sample pairs - SN vs CTRL, with the same pH and time parameters - the presence of Si_3N_4 powders in the culture media affected the contribution of bacterial Raman signals to the overall spectrum. In addition to being dependent on initial pH and exposure time, the effects seemed to be different for the two strains. The main results can be graphically summarized as follows:

Table XIV: Trend of Raman intensity ratios in SN samples w.r.t. CTRL for varying pH treatment (SE)

Band relationship	Time	pH treatment					
		5.5	6.5	7.5	7.5	8	8.5
Protein (Phen)	0h				↓	↓	
	24h		↓		↓		↑
Protein (amide II)	0h			↓			
	24h	↓	↑	↓			
Carbohydrates	0h	↓	↓	↓		↑	
	24h	↓	↓				↓
Lipids	0h		↓			↑	
	24h		↓			↓	
Nucleic acids	0h		↓	↓			
	24h	↓		↓	↓		↑
Cell wall	0h	↓				↑	
	24h	↓					

Table XV: Trend of Raman intensity ratios in SN samples w.r.t. CTRL for varying pH treatment (PG)

Band relationship	Time	pH treatment					
		5.5	6.5	7.5	7.5	8	8.5
Protein (Phen)	0h			↓		↓	
	72h	↓				↑	
Protein (amide III)	0h	↑	↑			↓	
	72h	↑					
Carbohydrates	0h	↑		↓			
	72h		↓	↓	↓	↑	↓
Lipids	0h		↑	↓	↑	↓	
	72h		↓		↓		
Nucleic acids	0h		↑	↓	↓		
	72h	↑		↓	↓		↓
Cell wall	0h	↑					
	72h				↓	↑	

↑	higher intensity ratio in the sample with SN compared to the CTRL
↓	lower intensity ratio in the sample with SN compared to the CTRL

5.4 Discussion

As anticipated in the discussion of the effect of different concentrations of silicon nitride powder on the activity and viability of *S. epidermidis*, a comprehensive explanation of the processes involved in the interaction between powders and bacteria is beyond the scope of the present study. Furthermore, the evaluation of the effect of silicon nitride with varying pH conditions required a much higher number of treatment groups, with different growing conditions and also with the introduction of a second bacterial strain, *P. gingivalis*, whose metabolism differs from SE. The higher information load prevents keeping the level of detail adopted in Section 4.3. In this broader perspective both the analysis of Raman spectra and microbial viability tests provided evidence for the pH-susceptibility of the mechanism of action of Si_3N_4 against bacteria, even if the results were distinct for the two investigated strains.

Considering *P. gingivalis*, a striking trend in the summary table (XV) is the presence of higher relative intensities in the spectra of bacteria grown with silicon nitride (w.r.t. CTRL samples) at initial pH 5.5 and 6.5, for Raman bands related to proteins, carbohydrates, lipids, NAs and cell wall components. A hypothesis could be linked to the dissolution of Si_3N_4, producing ammonia that, in acidic conditions, is almost fully present in its protonated form, inducing a gradual increase in hydroxyl ions which can result in a higher pH. It is reported that PG best thrives in neutral and mildly alkaline environments (pH from

7 to 8) [52, 53], hence silicon nitride is probably less effective on PG in acidic culture medium, since its dissolution can lead to a pH increase which constitutes a more favorable growth environment for this bacterium (compared to the CTRL groups in which the acidic conditions are maintained). Also from the WST assay results Si_3N_4 appeared to be effective in the acidic groups but having a minor impact with respect to the alkaline treatments (Fig.35 **c-d**); the assay didn't reveal any significant difference between the pH groups 5.5, 6.5 and 7.5 (72h) while between-group variability was evidenced through Raman spectroscopy, even though the analysis was not so sophisticated to discern variations in specific molecules (the bands assignments often pertain to a very wide class of biomolecules). As to the effect of Si_3N_4 powders in the alkaline conditions, both WST-assays and Raman intensity ratios suggested that the most significant difference lay between the treatments at pH 7.5 and pH 8, the sample at initial pH 7.5 being more affected by Si_3N_4 in terms of lower viability and lower Raman intensities for bands related to carbohydrates, lipids, nucleic acids and cell wall after 72h. There might be a relationship with the equilibrium chemistry of ionized/un-ionized ammonia, however the unionized form was proposed as the most harmful for bacteria [31] and above pH 7 its fractional percentage rapidly increases: this would signify a more detrimental impact of Si_3N_4 at pH 8 (w.r.t. pH 7.5), but the opposite trend emerged from the experiments of the present study. It is therefore possible that other mechanisms are involved in the antibacterial activity of silicon nitride, in addition to the previously supposed ionic stress caused by ammonia.

For what concerns *S. epidermidis*, almost all the investigated Raman bands displayed lower intensity ratios in the SN samples compared to the correspondent CTRL in the acidic treatment groups; variations were found among the samples at pH 5.5 and 6.5, the former presenting a more significant intensity decrease in the peak related to cell wall and the latter in the peak related to lipids (Table XIV). The comprehensive lower intensity in bands related to different biomolecules is in agreement with the phenomena hypothesized for SE in normal BHI broth (pH 7.5) in the previous Chapter (Section 4.3), namely: the alteration and/or degradation of cell wall and cell membrane and the inhibition of transcription and translation. According to the WST assays the viability of SE was most impacted in the cultures with Si_3N_4 at pH 5.5 and 8 (Fig.36). The same treatment groups were noticed in the FTIR analysis of the powders for causing the most remarkable changes in the powder spectrum; the measurement of zeta potential for the powders treated at pH 8 could have provided valuable insights on what these two treatment groups may have in common, unfortunately those powders were not analyzed. Surprisingly, the results of the intensity ratios of SE Raman bands in the samples treated at pH 8 are in contrast with those obtained for the sample pair at pH 5.5 and it is not clear why with the alkaline treatments the presence of silicon nitride induces a higher intensity contribution of the analyzed bands. In particular the ratios were higher (w.r.t. the CTRL samples) for bands related to carbohydrates, lipids and cell wall in the 0h dataset for pH 8, while for peaks related to proteins and nucleic acids in the 24h dataset for pH 8.5. Once again it is confirmed that the initial pH is a relevant factor for the antibacterial effects of Si_3N_4.

It is worth complementing the discussion in relation to some common and well-renowned antimicrobial mechanisms. In general an antibacterial agent targets growth processes and/or bacterial functions, which are either damaged or inhibited, and the mechanism of action can be classified into four main categories: interference with cell wall or cell membrane, interference with protein synthesis, interference with DNA replication, interference with metabolic processes [54]. When it comes to micro and nanoparticles various mechanisms can occur concurrently, depending on the properties of the particles, such as shape, size, surface charge and roughness, and the characteristics of the environment, such as temperature, pH, osmotic pressure and stirring [55]. Because of the highly complex nature of these

phenomena, often the specific mechanisms of action are not fully understood. Nevertheless, they usually involve one - or more - of the following effects: alteration of membrane permeability, membrane/wall disruption, oxidative stress caused by reactive oxygen species (ROS), damage to proton efflux pump and inhibition of electron transport chain, frequently leading to the eventual damage to DNA and proteins [55, 56]. The information extracted from the data collected in the present study was not sufficient to identify a specific mechanism for Si_3N_4, yet it is likely that the mechanism is strictly related to the powders' surface chemistry and silicon nitride hydrolysis and dissolution reactions play an important role, probably causing more than one detrimental effect, e.g. compromised wall/membrane, alteration of the concentration of ions in the cells, ionic stress. The additional use of other investigation techniques, for example based on fluorescent probes that bind to specific cellular components or employing proteomic or transcriptomic profiling [57], could allow a more detailed tracking of molecules involved in the bacterial reaction to silicon nitride, but the advantages of a non-destructive real-time characterization without external labels (such as Raman spectroscopy) would be lost. An ideal situation would be to identify some very specific Raman markers and to exploit the technique not as an explorative tool but as a diagnostic one.

5.5 Conclusion

For the investigation of the effect of pH on the antibacterial properties of Si_3N_4 powders, alterations in the bacterial cultures of *S. epidermidis* (SE) and *P. gingivalis* (PG) were analysed after culture in BHI broth with different pH conditions, for time up to 24h for SE and 72h for PG. The initial pH values were 5.5, 6.5, 7.5, 8 and 8.5 and each condition was replicated for a sample pair, one sample without silicon nitride (CTRL) and one sample with 16 mg/mL of silicon nitride powder dispersed in the medium (SN). WST assays and Raman spectroscopy were employed to monitor changes in microbial viability and in the bacterial Raman fingerprint. The results were analyzed pairwise, always relating the SN sample to the correspondent CTRL sample.

In every treatment group, after 24h or 72h the microbial viability assays revealed that viability was significantly lower in the SN samples, therefore silicon nitride exerted some antibacterial effects in all the investigated pH conditions, for both the tested bacterial strains. Comparing different sample pairs, the overall effect was variable among the various pH groups, indicating that the mechanism is susceptible to pH. In addition, distinct trends emerged for SE and PG. Analogous observations were derived from the evaluation of intensity ratios between Raman bands that were selected on the basis of statistical and biological criteria. Several SN samples displayed an intensity decrease (w.r.t. CTRL samples) in bands related to proteins, carbohydrates, lipids, nucleic acids and cell wall components, which can be distinctive signs of a compromised cell wall/membrane and of interference with transcription and translation reactions. Considering the outcome of the powder characterization performed in this study, it is reasonable that the antibacterial activity is in close connection with the reactions taking place on the surface of Si_3N_4 particles. The hydrolysis and dissolution of the surface layers involve the production of ammonia and the penetration of unionized ammonia in the cells could be the trigger of a stress condition for the bacteria. Yet, the powders were also effective in acidic conditions where the percentage of unionized ammonia is almost zero, therefore suggesting the presence of alternative or concurrent mechanisms.

References Chapter 4 and 5

1. Dojindo. *Microbial Viability Assay Kit-WST* https://www.dojindo.eu.com/store/p/141-Microbial-Viability-Assay-Kit-WST.aspx.
2. Notingher, I. & Hench, L. L. Raman microspectroscopy: A noninvasive tool for studies of individual living cells *in vitro*. *Expert Review of Medical Devices* **3,** 215–234. doi:10.1586/17434440.3.2.215 (2006).
3. De Gelder, J., De Gussem, K., Vandenabeele, P. & Moens, L. Reference database of Raman spectra of biological molecules. *Journal of Raman Spectroscopy* **38,** 1133–1147. doi:10.1002/jrs.1734 (2007).
4. Czamara, K. *et al.* Raman spectroscopy of lipids: A review. *Journal of Raman Spectroscopy* **46,** 4–20. doi:10.1002/jrs.4607 (2015).
5. Stone, N., Kendall, C., Smith, J., Crow, P. & Barr, H. Raman spectroscopy for identification of epithelial cancers. *Faraday Discussions* **126,** 141–157. doi:10.1039/b304992b (2004).
6. Paret, M. L., Sharma, S. K., Green, L. M. & Alvarez, A. M. Biochemical characterization of Gram-positive and Gram-negative plant-associated bacteria with micro-raman spectroscopy. *Applied Spectroscopy* **64,** 433–441. doi:10.1366/000370210791114293 (2010).
7. Chan, J. W. *et al.* Micro-raman spectroscopy detects individual neoplastic and normal hematopoietic cells. *Biophysical Journal* **90,** 648–656. doi:10.1529/biophysj.105.066761 (2006).
8. Wiercigroch, E. *et al.* Raman and infrared spectroscopy of carbohydrates: A review. *Spectrochimica Acta - Part A: Molecular and Biomolecular Spectroscopy* **185,** 317–335. doi:10.1016/j.saa.2017.05.045 (2017).
9. Kuhar, N., Sil, S., Verma, T. & Umapathy, S. Challenges in application of Raman spectroscopy to biology and materials. *RSC Advances* **8,** 25888–25908. doi:10.1039/c8ra04491k (2018).
10. Cheng, W. T., Liu, M. T., Liu, H. N. & Lin, S. Y. Micro-Raman spectroscopy used to identify and grade human skin pilomatrixoma. *Microscopy Research and Technique* **68,** 75–79. doi:10.1002/jemt.20229 (2005).
11. Williams, A. C. & Edwards, H. G. Fourier transform Raman spectroscopy of bacterial cell walls. *Journal of Raman Spectroscopy* **25,** 673–677. doi:10.1002/jrs.1250250730 (1994).
12. Neugebauer, U. *et al.* Towards a detailed understanding of bacterial metabolism - Spectroscopic characterization of Stophylococcus epidermidis. *ChemPhysChem* **8,** 124–137. doi:10.1002/cphc.200600507 (2007).
13. Carmona, P. & Molina, M. Raman and infrared spectra of D-ribose and D-ribose 5-phosphate. *Journal of Raman Spectroscopy* **21,** 395–400. doi:10.1002/jrs.1250210703 (1990).
14. Rehman, I., Movasaghi, Z. & Rehman, S. *Chapter 8: FTIR and Raman characteristic peak frequencies in biological studies* in *Vibrational Spectroscopy for Tissue Analysis* 1st edition (Taylor & Francis group, 2012). doi:10.1201/b12949.
15. Huang, Z., Lui, H., McLean, D. I., Korbelik, M. & Zeng, H. Raman Spectroscopy in Combination with Background Near-infrared Autofluorescence Enhances the In Vivo Assessment of Malignant Tissues. *Photochemistry and Photobiology* **81,** 1219–1226. doi:10.1562/2005-02-24-ra-449 (2005).
16. Maquelin, K. *et al.* Identification of medically relevant microorganisms by vibrational spectroscopy. *Journal of Microbiological Methods* **51,** 255–271. doi:10.1016/S0167-7012(02)00127-6 (2002).
17. Cîntă Pînzaru, S., Andronie, L. M., Domsa, I., Cozar, O. & Astilean, S. Bridging biomolecules with nanoparticles: Surface-enhanced Raman scattering from colon carcinoma and normal tissue. *Journal of Raman Spectroscopy* **39,** 331–334. doi:10.1002/jrs.1907 (2008).
18. Lemma, T., Saliniemi, A., Hynninen, V., Hytönen, V. P. & Toppari, J. J. SERS detection of cell surface and intracellular components of microorganisms using nano-aggregated Ag substrate. *Vibrational Spectroscopy* **83,** 36–45. doi:10.1016/j.vibspec.2016.01.006 (2016).
19. Ruiz-Chica, A. J., Medina, M. A., Sánchez-Jiménez, F. & Ramírez, F. J. Characterization by Raman spectroscopy of conformational changes on guanine-cytosine and adenine-thymine oligonucleotides induced by aminooxy analogues of spermidine. *Journal of Raman Spectroscopy* **35,** 93–100. doi:10.1002/jrs.1107 (2004).
20. Stone, N., Kendall, C., Shepherd, N., Crow, P. & Barr, H. Near-infrared Raman spectroscopy for the classification of epithelial pre-cancers and cancers. *Journal of Raman Spectroscopy* **33,** 564–573. doi:10.1002/jrs.882 (2002).
21. Verrier, S., Notingher, I., Polak, J. M. & Hench, L. L. In Situ Monitoring of Cell Death Using Raman Microspectroscopy. *Biopolymers* **74,** 157–162. doi:10.1002/bip.20063 (2004).
22. Krafft, C., Neudert, L., Simat, T. & Salzer, R. Near infrared Raman spectra of human brain lipids. *Spectrochimica Acta - Part A: Molecular and Biomolecular Spectroscopy* **61,** 1529–1535. doi:10.1016/j.saa.2004.11.017 (2005).
23. Da Silva, E. & Rousseau, D. Molecular order and thermodynamics of the solid-liquid transition in triglycerides via Raman spectroscopy. *Physical Chemistry Chemical Physics* **10,** 4606–4613. doi:10.1039/b717412h (2008).
24. Boschetto, F. *et al.* In situ molecular vibration insights into the antibacterial behavior of silicon nitride bioceramic versus gram-negative Escherichia coli. *Spectrochimica Acta - Part A: Molecular and Biomolecular Spectroscopy* **223,** 117299. doi:10.1016/j.saa.2019.117299 (2019).
25. Zhmud, B. V. & Bergström, L. Dissolution kinetics of silicon nitride in aqueous suspension. *Journal of Colloid and Interface Science* **218,** 582–584. doi:10.1006/jcis.1999.6425 (1999).
26. Laarz, E., Zhmud, B. V. & Bergström, L. Dissolution and Deagglomeration of Silicon Nitride in Aqueous Medium. *Journal of the American Ceramic Society* **83,** 2394–2400. doi:10.1111/j.1151-2916.2000.tb01567.x (2004).
27. Pezzotti, G. *et al.* Silicon Nitride Bioceramics Induce Chemically Driven Lysis in Porphyromonas gingivalis. *Langmuir* **32,** 3024–3035. doi:10.1021/acs.langmuir.6b00393 (2016).

28. Müller, T., Walter, B., Wirtz, A. & Burkovski, A. Ammonium toxicity in bacteria. *Current Microbiology* **52,** 400–406. doi:10.1007/s00284-005-0370-x (2006).
29. Emerson, K., Russo, R. C., Lund, R. E. & Thurston, R. V. Aqueous Ammonia Equilibrium Calculations: Effect of pH and Temperature. *Journal of the Fisheries Research Board of Canada* **32,** 2379–2383. doi:10.1139/f75-274 (1975).
30. Kadam, P. C. & Boone, D. R. Influence of pH on ammonia accumulation and toxicity in halophilic, methylotrophic methanogens. *Applied and Environmental Microbiology* **62,** 4486–4492. doi:10.1128/aem.62.12.4486-4492.1996 (1996).
31. Pezzotti, G. Silicon Nitride: A Bioceramic with a Gift. *ACS Applied Materials and Interfaces* **11,** 26619–26636. doi:10.1021/acsami.9b07997 (2019).
32. Muttray, A. F. & Mohn, W. W. RNA/DNA ratio as an indicator of metabolic activity in resin acid-degrading bacteria. *Water Science and Technology* **37,** 89–93. doi:10.2166/wst.1998.0589 (1998).
33. Kerkhof, L. & Ward, B. B. Comparison of nucleic acid hybridization and fluorometry for measurement of the relationship between RNA/DNA ratio and growth rate in a marine bacterium. *Applied and Environmental Microbiology* **59,** 1303–1309. doi:10.1128/aem.59.5.1303-1309.1993 (1993).
34. Cagliero, C. & Jin, D. J. Dissociation and re-association of RNA polymerase with DNA during osmotic stress response in Escherichia coli. *Nucleic Acids Research* **41,** 315–326. doi:10.1093/nar/gks988 (2013).
35. Sørensen, M. A., Fehler, A. O. & Lo Svenningsen, S. Transfer RNA instability as a stress response in Escherichia coli: Rapid dynamics of the tRNA pool as a function of demand. *RNA Biology* **15,** 586–593. doi:10.1080/15476286.2017.1391440 (2018).
36. Hauryliuk, V., Atkinson, G. C., Murakami, K. S., Tenson, T. & Gerdes, K. Recent functional insights into the role of (p)ppGpp in bacterial physiology. *Nature Reviews Microbiology* **13,** 298–309. doi:10.1038/nrmicro3448 (2015).
37. Akhova, A. V. & Tkachenko, A. G. ATP/ADP alteration as a sign of the oxidative stress development in Escherichia coli cells under antibiotic treatment. *FEMS Microbiology Letters* **353,** 69–76. doi:10.1111/1574-6968.12405 (2014).
38. Kim, H. M. & Davey, M. E. Synthesis of ppGpp impacts type IX secretion and biofilm matrix formation in Porphyromonas gingivalis. *npj Biofilms and Microbiomes* **6.** doi:10.1038/s41522-020-0115-4 (2020).
39. Geiger, T., Kästle, B., Gratani, F. L., Goerke, C. & Wolz, C. Two small (p)ppGpp synthases in staphylococcus aureus mediate tolerance against cell envelope stress conditions. *Journal of Bacteriology* **196,** 894–902. doi:10.1128/JB.01201-13 (2014).
40. Rohde, H., Frankenberger, S., Zähringer, U. & Mack, D. Structure, function and contribution of polysaccharide intercellular adhesin (PIA) to Staphylococcus epidermidis biofilm formation and pathogenesis of biomaterial-associated infections. *European Journal of Cell Biology* **89,** 103–111. doi:10.1016/j.ejcb.2009.10.005 (2010).
41. Gomes, F., Teixeira, P., Cerca, N., Ceri, H. & Oliveira, R. Virulence gene expression by staphylococcus epidermidis Biofilm cells exposed to antibiotics. *Microbial Drug Resistance* **17,** 191–196. doi:10.1089/mdr.2010.0149 (2011).
42. Boschetto, F., Adachi, T., Horiguchi, S. & Fainozzi, D. Monitoring metabolic reactions in Staphylococcus epidermidis exposed to silicon nitride using in situ time-lapse Raman spectroscopy. *Journal of Biomedical Optics* **23,** 056002. doi:10.1117/1.jbo.23.5.056002 (2018).
43. Rice, K. C. & Bayles, K. W. Molecular Control of Bacterial Death and Lysis. *Microbiology and Molecular Biology Reviews* **72,** 85–109. doi:10.1128/mmbr.00030-07 (2008).
44. Varmuza, K. & Filzmoser, P. doi:10.1201/9781420059496 (CRC Press, 2016).
45. Jollife, I. T. & Cadima, J. Principal component analysis: A review and recent developments. *Philosophical Transactions of the Royal Society A: Mathematical, Physical and Engineering Sciences* **374.** doi:10.1098/rsta.2015.0202 (2016).
46. Cordella, C. B. *PCA: The Basic Building Block of Chemometrics* in *Analytical Chemistry* (2012). doi:10.5772/51429.
47. Gautam, R., Vanga, S., Ariese, F. & Umapathy, S. Review of multidimensional data processing approaches for Raman and infrared spectroscopy. *EPJ Techniques and Instrumentation* **2.** doi:10.1140/epjti/s40485-015-0018-6 (2015).
48. Senger, R. S. & Scherr, D. Resolving complex phenotypes with Raman spectroscopy and chemometrics. *Current Opinion in Biotechnology* **66,** 277–282. doi:10.1016/j.copbio.2020.09.007 (2020).
49. Colniță, A. *et al.* Characterization and discrimination of gram-positive bacteria using Raman spectroscopy with the aid of principal component analysis. *Nanomaterials* **7,** 248. doi:10.3390/nano7090248 (2017).
50. Walter, A., März, A., Schumacher, W., Rösch, P. & Popp, J. Towards a fast, high specific and reliable discrimination of bacteria on strain level by means of SERS in a microfluidic device. *Lab on a Chip* **11,** 1013–1021. doi:10.1039/c0lc00536c (2011).
51. NCSS Statistical Software. *NCSS Documentation - Multivariate Analysis* https://ncss-wpengine.netdna-ssl.com/wp-content/themes/ncss/pdf/Procedures/NCSS/Principal_Components_Analysis.pdf.
52. McDermid, A. S., McKee, A. S. & Marsh, P. D. Effect of environmental pH on enzyme activity and growth of Bacteroides gingivalis W50. *Infection and Immunity* **56,** 1096–100. doi:10.1128/iai.56.5.1096-1100.1988 (1988).
53. Takahashi, N. & Schachtele, C. F. Effect of pH on the Growth and Proteolytic Activity of Porphyromonas gingivalis and Bacteroides intermedius. *Journal of Dental Research* **69,** 1266–9. doi:10.1177/00220345900690060801 (1990).

54. Kapoor, G., Saigal, S. & Elongavan, A. Action and resistance mechanisms of antibiotics: A guide for clinicians. *Journal of Anaesthesiology Clinical Pharmacology* **33,** 300–305. doi:10.4103/joacp.JOACP_349_15 (2017).
55. Wang, L., Hu, C. & Shao, L. The antimicrobial activity of nanoparticles: Present situation and prospects for the future. *International Journal of Nanomedicine* **12,** 1227–1249. doi:10.2147/IJN.S121956 (2017).
56. Shaikh, S. *et al.* Mechanistic insights into the antimicrobial actions of metallic nanoparticles and their implications for multidrug resistance. *International Journal of Molecular Sciences* **20,** 2468. doi:10.3390/ijms20102468 (2019).
57. Raheem, N. & Straus, S. K. Mechanisms of Action for Antimicrobial Peptides With Antibacterial and Antibiofilm Functions. *Frontiers in Microbiology* **10,** 2866. doi:10.3389/fmicb.2019.02866 (2019).

6 Conclusions, Limitations and Future Perspectives

The assessment and understanding of newly emerged antibacterial materials is of fundamental importance to tackle the problem of antimicrobial resistance. Within this framework, the present study aimed at investigating the effect of pH on the antibacterial activity of silicon nitride powders against the Gram positive *S. epidermidis* and the Gram negative *P. gingivalis*. The powder concentration of 16 mg per mL of culture medium was selected as the outcome of the preliminary phase of the study and used in the subsequent experiments. Microbial viability assays and Raman spectroscopy were employed to monitor the effects of the powders on bacterial cultures with initial pH 5.5, 6.5, 7.5, 8 and 8.5, after an exposure time up to 24h and 72h. The mere powders were pH-treated for the same time points and characterized - after purification - by ATR-FTIR spectroscopy, Raman spectroscopy, XPS and zeta potential measurements.

Remarkable differences were noticed through the characterization of the treated powders in comparison with an untreated sample, suggesting alterations in the surface chemistry and bonding structure of Si_3N_4. To be highlighted is the variable presence of oxygen-related signals in the FTIR and Raman spectra, as well as in the XPS results, which indicates different degrees of oxidation among the powders belonging to distinct treatment groups and can be related to the hydrolysis and dissolution of the outermost layers of the particles, whose reactions are dependent on pH. The hypothesis is also supported by the positive zeta potential values observed for the treated powders, which suggest the emergence of non-oxidized Si_3N_4 surface.

The examination of bacterial cultures clearly showed that silicon nitride had a detrimental impact on the viability of SE and PG in all the tested pH conditions. Both WST assays and Raman spectroscopy allowed to verify that the effect was different depending on the pH of the medium and on the bacterial strain. The latter technique revealed significant variations in Raman signals related to several biomolecules which represent the cellular building blocks. It is not clear whether the mechanism relies on the damage to cell wall and cell membrane components or on the interference with key internal processes such as DNA replication, transcription or translation. The elution of ammonia from the powders and its penetration inside the cells could play an important role but from the experimental evidence it cannot be considered as the sole mechanism.

Several factors contributed to the limitations of this study, both in terms of experiments and of data analysis and interpretation. Concerning the evaluation of the activity of Si_3N_4 on bacteria, one important limiting factor was the number of spectra per sample, 6 spectra for each sample is in fact very low for addressing biological matter by Raman spectroscopy, since the content of the sample is not uniform. In this regards, the average of six spectra is not always very meaningful and some features might be averaged out, with the disadvantage that useful information can be missed in the visual comparison of average spectra. The number of replicates was also low for a thorough, fully statistical approach based on multivariate data analysis in which, having a substantial amount of spectra, one could define a model and use a subset of the data as a training set and then classify the newly acquired spectra (test data set) according to the trained model. Without such rigorous application of the method, the risk is to lose the "biological" meaning of the Raman signals in return for statistical significance. Another key limitation in the analysis of bacterial Raman spectra was the absence of some *a priori* strongly relevant marker band: to look after few specific bands, instead of exploring the whole spectral range, could have facilitated the elaboration of the data and its interpretation.

On more experimental grounds, it should be evidenced that pH was measured only at the beginning

of the treatments while, particularly for the characterization of the powders, it would have been insightful to check the pH at intermediate and final time points in relation to the interpretation of the surface reactions taking place on the particles. Furthermore, the zeta potential measurements were limited to only three treatment groups and didn't fully allow to compare the different scenarios. Lastly, again considering the experiments with bacteria, Raman spectroscopy was only flanked by WST assays, which however do not provide information on specific cellular components but only on the overall viability of the culture, thus being not highly supportive in the interpretation of trends in Raman signals.

In the light of these considerations, further investigation is needed to better understand the processes behind silicon nitride antibacterial activity. In order to improve the robustness and the depth of the information, future studies on this topic could involve some of the following elements:

- the measurement of pH at multiple time intervals, to monitor the evolution of chemical reactions;
- the additional characterization of the powders with techniques assessing variations in the crystalline structure (for example X-Ray Diffraction) and in the particle size (for example Dynamic Light Scattering), to evaluate changes in the bonding structure and reductions in average particle size (if any);
- the increase in the number of Raman spectra per bacterial sample;
- the refinement of the bacterial Raman bands assignment and the identification/definition of impactful marker bands to allow the usage of Raman spectroscopy as a diagnostic tool;
- the supplementary analysis of bacterial cells with methods that involve staining of very specific molecules and/or methods for the proteomic and transcriptomic profiling, for better support and comparison with the Raman data.

Acknowledgements

I want to express my gratitude to all the people who crossed my path during the last three years, those who made this work easier and those who made it harder. In one way or the other, both sides gave me stimuli to become a stronger person with an enlarged vision. A product is always the outcome of a process, a sequence of transformations and events... and if the product is growth and improvement, then any part of the process was worth being there and being experienced.

In particular I would like to thank professors Alvise Benedetti and Giuseppe Pezzotti for giving me the opportunity to carry out my thesis internship at the Kyoto Institute of Technology; professor Wenliang Zhu for the useful advice on the XPS, FTIR and Raman spectra of silicon nitride; professor Eriko Ohgitani for allowing me in her lab at the Kyoto Prefectural University of Medicine, with trust and kindness; professor Elia Marin for his dedication and for encouraging me in the struggle with self-confidence.

Thanks to Galih, for helping me out with tons of Japanese documents to fill in; to Francesco, Matteo, Thefye and Taigi, for eating delicious food together, playing cards, singing or simply gathering along the Kamo river.

I thank Marikoji Kaikan for guaranteeing safety measures during the pandemic and I thank the city of Kyoto, for making me breathe in the toughest days, for letting me wander around with wonder.

Thanks to Raffaella, Silvia and Patrizia, an emergency ladder to get out of a nightmare; to Ca' Foscari Competency Lab and Emotional Leadership Lab initiatives, a boost of positive energy.

A big thank you to my friend Gigio, for the overseas night calls, of great support, and to my friend Christian for the unexpected understanding and mental closeness. To my friend Alberto for the countless moments and experiences that we shared and for being there as much as you could, we'll keep growing.

My deepest gratitude to family, despite my hermeticism, for being "home", for asking, listening and caring, for loving me and leaving me free.

Vi ringrazio.

Martina

Appendix A Additional information

Chapters 4 and 5 - Bacterial cultures

Bacteria were preserved at -80°C, and the initial density of *S. epidermidis* was $1.8 \cdot 10^{10}$ CFU/mL while $5 \cdot 10^{10}$ CFU/mL for *P. gingivalis*. After thawing, the first culture step for SE involved inoculating 10 mL of fresh BHI broth with 20 µL of bacteria solution. After 24h of incubation at 37°C the medium was changed, again in the ratio of 20 µL of bacterial sample in 10 mL of fresh medium. At this point, 10 µL of the new bacterial solution were added to the individual samples (CTRL or SN) of 1 mL each. For PG, 200 µL of thawed bacteria were inoculated into 10 mL of BHI broth, then the medium was changed after 4 days of incubation by adding 2 mL of bacterial solution into 8 mL of fresh medium. At this point 250 µL of the final bacterial culture were added to each sample of 1 mL.

Chapter 5 - Raman intensity ratio

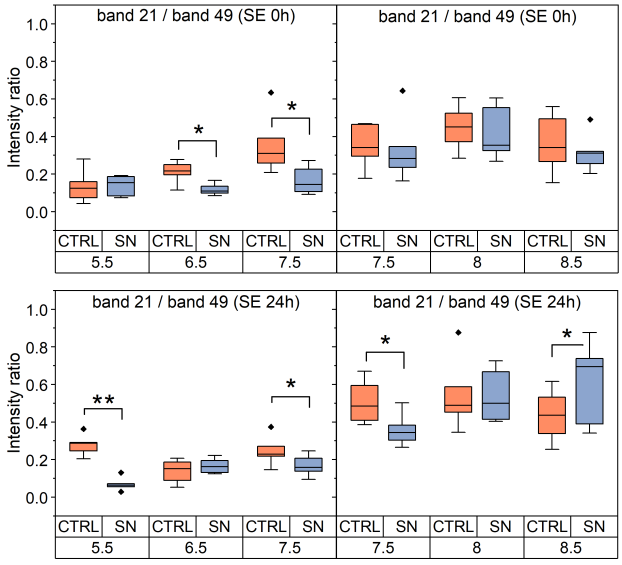

Figure A.1: Intensity ratios for Raman bands related to NAs (SE): Band 48 corresponds to CH_2 deformation in deoxyribose.